Universidade de Aveiro Departamento de Engenharia Mecânica
2019

Bernardo Filipe Valente Guimarães

Otimização do comportamento dinâmico-acústico de ventiladores de bombas de calor

Optimization of the dynamic-acoustic behaviour in heat pump axial fans

Universidade de Aveiro Departamento de Engenharia Mecânica
2019

Bernardo Filipe Valente Guimarães

Otimização do comportamento dinâmico-acústico de ventiladores de bombas de calor

Optimization of the dynamic-acoustic behaviour in heat pump axial fans

Dissertação apresentada à Universidade de Aveiro para cumprimento dos requisitos necessários à obtenção do grau de Mestre em Engenharia Mecânica, realizada sob orientação científica de Rui António da Silva Moreira, Professor Auxiliar, da Universidade de Aveiro e de Jürgen Herbst, Engenheiro Acústico do Departamento TT-RHP/Eng-Av da Bosch Termotecnologia S.A..

Esta dissertação teve o apoio dos projetos

UID/EMS/00481/2019-FCT - FCT - Fundação para a Ciência e a Tecnologia;

CENTRO-01-0145-FEDER-022083 - Programa Operacional Regional do Centro (Centro2020), através do Portugal 2020 e do Fundo Europeu de Desenvolvimento Regional;

O júri / The jury

Presidente / President

Professor Doutor António Manuel de Amaral Monteiro Ramos
Professor Auxiliar da Universidade de Aveiro

Vogais / Committee

Professor Doutor José Fernando Dias Rodrigues
Professor Associado da Faculdade de Engenharia da Universidade do Porto

Professor Doutor Rui António da Silva Moreira
Professor Auxiliar da Universidade de Aveiro

Agradecimentos / Acknowledgements

Foremost, I offer my sincere gratitude to my advisors Prof.Dr.Rui Moreira from the Mechanical Engineering Department, and Dr.Jürgen Herbst from the Heat Pump Development Department of Bosch Termotecnologia S.A., for their continued guidance whenever I was facing difficulties during the thesis. I am extremely grateful to Dr.Alister Clay from Bosch Thermotechnik GmbH. Junkers, for sharing his knowledge on turbomachinery aerodynamics and CFD modeling in particular. I am forever thankful to my colleagues Almeida, Pinho and Tavares for their friendship and support, and for creating a cordial working environment. A very special word of thanks goes for my family and Eliana for their support and patience during the time of writing my thesis.

Keywords Aeroacoustics; Axial Fan Noise; Heat Pump; Dimples; Finlets; Boundary Layer separation; Flexible trailing edge

Abstract The aim of this investigation is the aeroacoustic analysis of the boundary layer separation noise and trailing edge noise in a heat pump axial fan, using Computational Fluid Dynamics (CFD), Fluid Fluid Structure Interaction (FSI) and Computational Aeroacoustics (CAA). The Broadband Noise Source (BNS) model and Transition SST turbulence model, implemented in Fluent 19.0, were used to study the boundary layer noise component of the three noise reduction features in steady-state and transient simulations. The objectives of this study were divided into two main parts: the analysis and optimization of golf ball dimples to control the the boundary layer separation on fan blade and the study regarding the application of two features from the "silent" flight of the owl on the fan, the finlets and the flexible trailing edge. The parametric optimization on dimples showed a 15,1% shift in boundary layer separation. This optimized pattern when applied to the suction side of the fan blade shifting the boundary layer separation which promotes the inhibition of the vortex generated at the junction of the blade with the hub resulting in a reduction of up to 0,8 dB under normal fan operating conditions. It was also found that dimples have a greater influence on operating conditions under an airflow less than 1500 m^3/h, showing a shift in the stall resulting in an increase of the fan efficiency by 1,9% and a decrease in the boundary layer noise of 2,9 dB. On the second part of the work it was found that a fan with finlets presented a reduction of 0,3 dB at 300 rpm, although the results showed an increase in noise and a decrease in efficiency for higher rpm than those for which the finlets were optimized. The study of an flexible trailing edge showed a decrease in the thickness of the turbulence generated by the boundary layer. This, due to the downward movement of the flexible trailing edge that decreases the pressure mismatch between the suction surface and the pressure surface and the decrease of the angle of attack caused by its upward movement. Experimental measurements of an dimpled fan prototype, conducted in a hemi-anechoic chamber showed noise improvements in the order of 0,5 dB(A), the results suggested that for lower velocities than 380 rpm an increase in the fan efficiency is expected. Lastly, an attempt was made to induce stall in the fan through the obstruction of the heat pump evaporator. This investigation identified that for an airflow of 1700 m^3/h at 535 rpm the original fan enters in a light stall condition while the dimpled fan prototype maintains its normal operating conditions, resulting in a reduction of 0,9 dB(A).

Palavras-chave Ruído de Ventiladores Axiais; Aeroacústica; Bomba de Calor; Cavidades de bolas de golf; Bordo de Fuga Alhetado; Turbulência na Camada Limite; Bordo de Fuga Flexível

Resumo O objetivo deste trabalho de investigação consistiu na análise do ruído aeroacústico emitido pelo ventilador aplicado às unidades exteriores das bombas de calor, recorrendo a Computational Fluid Dynamics (CFD), Fluid Fluid Structure Interaction (FSI) e Computational Aeroacoustics (CAA). O modelo acústico Broadband Noise Source (BNS) e o modelo de turbulência Transition SST, implementados no código comercial Fluent 19.0 foram utilizados para avaliar diferentes técnicas de redução do ruído emitido pela separação da camada limite e pelo bordo de fuga. Os objetivos deste estudo estão divididos em duas componentes: a análise e otimização de cavidades inspiradas nas bolas de golf para o atraso da separação da camada limite na pá do ventilador e o estudo da implementação de duas características do voo "silencioso" das corujas no ventilador, o bordo de fuga alhetado e o bordo de fuga flexível. Os resultados da otimização paramétrica das cavidades das bolas de golf mostram um atraso na separação da camada limite de 15,1%. Este padrão otimizado quando aplicado no lado de sucção da pá do ventilador atrasa a separação da camada limite o que promove a inibição do vortex gerado entre a pá e o centro do ventilador resultando numa redução de até 0,8 dB em condições normais de funcionamento do ventilador. As cavidades das bolas de golf mostram ter uma maior influência para condições de operação com um fluxo de ar inferior a 1500 m^3/h, mostrando atrasar o fenômeno de stall, aumentado a eficiência do ventilador em 1,9% e diminuíndo o ruído aerodinâmico em 2,9 dB em comparação com o modelo original. Na segunda parte da tese foi descoberto que um bordo de fuga alhetado revela uma redução de ruído de 0,3 dB a 300 rotações por minuto, sendo que se verifica perda de eficiência e aumento do ruído do ventilador para rotações por minuto superiores aos quais as alhetas foram geometricamente otimizadas. O estudo da utilização de um bordo de fuga flexível mostrou a diminuição da espessura da turbulência gerada pela camada limite através do movimento descende do bordo de fuga flexível que diminui a diferença de pressão entre a superfície de sucção e a superfície pressão e a diminuição do ângulo de ataque com o seu movimento ascendente. Medições experimentais realizados numa câmara semi-anecóica do protótipo do ventilador com cavidades inspiradas nas bolas de golf mostraram melhorias na ordem de 0,5 dB(A) para diferentes rotações por minuto e sugerem um aumento da eficiência para rotações por minuto inferiores a 380. Por fim foi feita a tentativa de induzir um escoamento totalmente separado no ventilador através da obstrução do evaporador da bomba de calor, este estudo identificou que que para um fluxo de ar de 1700 m^3/h a 535 rotações por minuto o ventilador original entra em condição de separação total sendo que o protótipo do ventilador com cavidades inspiradas nas bolas de golf mantem condições de funcionamento normais, resultando numa redução de 0,9 dB(A).

Contents

List of Tables

Intentionally blank page.

List of Figures

Chapter 1

Introduction and Background

The present work was developed within the Acoustics Team from Bosch Termotecnologia S.A., based in Aveiro, and addresses the application of Computational Fluid Dynamics (CFD) and Computational Aeroacoustics (CAA) in the research and development process of axial fans for heat pump units. This chapter starts with a brief introduction to the company and the phenomenon of fan noise, followed by the motivation behind this work and the impact in different engineering applications.

1.1 Bosch Termotecnologia S.A.

The mission of Bosch Thermotechnology is to supply costumers with efficient room climate, domestic hot water and decentralised energy management solutions. The company offers innovative solutions that address market needs while maintaining a constant focus on new ways to reduce CO_2 emissions.

In 1988 Bosch Thermotechnology established its presence in the city of Aveiro with the acquisition of the Vulcano Termodomésticos. At the moment the company is responsible for the development and design of water heaters, gas boilers, electrical appliances for water heating, heat pumps and in addition the production of some of these devices.

1.2 Heat Pump

In Europe, primary energy consumption in the building sector is around 40%. Of these, 75% are used for room heating and hot water generation [1]. The use of heat pumps is an attractive solution due to the high seasonal coefficient of performance and low CO_2 emission compared to conventional heating systems. These advantages lead to an annual growth of 12% in 2017, according to the European Heat Pump Association [1].

The working principle of a heat pump is to extract low grade heat from the heat source, this heat exchange takes place in the evaporator due to the forced convection promoted by the axial fan. In this phase the refrigerant goes from its liquid state to a low pressure vapour. The low pressure vapour passes through the compressor increases its pressure and temperature. Then the high temperature vapour enters the condenser and transfers heat to the building, becoming a high pressure, moderate temperature liquid after being condensed. The moderate temperature liquid passes through an expansion valve that reduces its pressure and temperature. The refrigerant returns to the

evaporator to start another cycle.

The Bosch Heat Pumps external units currently uses two different types of axial fans with different blade designs, one for each heat pump chassis (Figure 1.1). This research focuses on one of the two fan types since it is in the company's interest to use a single fan for the entire product range.

Figure 1.1: Component diagram of the AirX Bosch Heat Pump outdoor unit [2].

1.3 Fan Noise

Turbomachines are used for the conversion of mechanical energy into thermal and pressure energy by the interaction of the blade with the fluid, creating a pressure differential between the top surface and the bottom surface of the blade. The fan is usually contained within a shroud which channels the airflow in a certain direction according to its application. There are four different types of fans: the axial fan, the centrifugal fan, the tangential fan and the mixed fan. From these four fan types only one will be studied, the axial fan.

Acoustic waves are generated by many different sources within the fan and the shroud. It is necessary to consider that these waves propagate, influencing other waves from other sources, and can be absorbed by the geometry or the flow. The aeroacoustic noise sources in low-speed axial fans can be characterized by the frequencies at which they occur. Every fan has the characteristic of generating a tone at the blade passing frequency (BPF), given by Equation (1.1).

$$f_{BPF} = \frac{Nb \cdot RPM}{60} \tag{1.1}$$

where Nb represents the number of blades and RPM the rotational speed in revolutions per minute. The BPF tones are affected by the following factors:

- The operating point of the fan dictates the characteristics of the flow field and the blade loading. When the fan operates in stall conditions, rotating instabilities are generated producing wide peaks at the BPF [3].
- Inlet flow fluctuations leads to an increase in unsteady blade forces which causes variations in the blade loading, this phenomenon generates eddies on the suction side of the blade. The fan blades passing through these eddies results in a tone noise at the BPF [4].

In addition to the tonal noise, axial fans produce broadband noise associated with the variations of speed of the flow near the surface of the blade. Thus, the separation of the boundary layer is directly related to broadband noise, due to the generation of turbulence and unsteady loading. The research by Moreau et al. [5] have shown that when an low to moderate Reynolds number flow goes over an airfoil it becomes complex due to flow separation, impacting in a great scale broadband noise.

The axial fan under this study operates with a low Reynolds number witch is expected to influence the broadband noise generated, leading to differences when compared to most of the well-researched high Reynolds regime in axial fans. Therefore, the purpose of this research will be the study of the broadband fan noise due to boundary layer separation in the blade and its interaction within the rest of the neighbour blades, the motor and the shroud.

1.4 Motivation

Aerodynamic noise emitted from turbomachinery is an increasing concern in different engineering applications in terms of comfort and regulations. Industries such as automotive, energy and aerospace have placed a emphasis in order to attend to the urbanization, better standards of living and noise legislation.

In the automotive industry, with the great improvement in noise reduction inside and outside commercial vehicles, more attention is given to reducing the noise emitted from the radiator's fan which is a huge contributor to the overall noise, in some cases dominates over other sources such as engine, transmission, tire, mechanical or exhaust contributions [6].

In the energy sector there is a focus on reducing the noise emitted by wind turbines, which has been proven to reduce the quality of sleep, namely the reduction of deep sleep and an increased frequency of awakenings [7]. Many countries have regulations that stipulate the distance between wind turbine farms and urban areas, leading to a constraint in the push towards energy sustainability [8].

Large delivery companies such as Amazon and Google plan in the near future to use drones for delivering small and light packages. On July 17, 2015 the first commercial drone was approved by the Federal Aviation Administration [9]. However, studies by NASA show that the production of high-frequency noise of drones is perceived as more annoying than the commercial car, making noise the biggest obstacle to the use of this engineering application [10].

As the density of buildings in urban centers grows, there are major concerns about interior sound and its impact on people's lives. In the comparison between different equipment's that produce interior noise, the exhaust fans come first with (75.8 dB) followed by the pump (74.3 dB) and ventilation fan (65.5 dB)[11].

Considering the technological advances in the mentioned areas, it is imperative to achieve an acceptable noise without compromising the efficiency or the design of the application. The ideal fan design for low noise would aim to stop it from being generated in the first place. Thus, the reduction of noise at the source is addressed as the target of this research.

1.5 Objectives

One of the major targets for the next generation of heat pump's is the reduction of the overall noise. Therefore, the constant effort by Bosch Thermotechnology to reduce noise in the main sources: the fan, the compressor and the occasional turbulent flow in the fins of the evaporator. The previous research by Santos [12] has identified the noise sources on the different heat pump fans and the influence of the tip speed, motor cap and noise reduction features, such as serrated trailing edge and dimples. The experimental test results of the re-scaled 3D printed model of the fan with dimples showed to be a promising noise feature, with a potential reduction of 3.7 dB.

A parametric study of the boundary layer separation will be undertaken in a two-dimensional flow. This will identify the mechanism behind the shift of the boundary layer separation with the implementation of dimples in the blade surface. The optimized parametrization will be adapted to a three-dimensional flow and will be applied to the original model of the fan. The aeroacoustics of the dimpled fan models will be analysed by comparison with the reference fan model through Computational Fluid Dynamics (CFD) and Computational Aeroacoustics (CAA) numerical simulations. An steady-state method will be used to compare the different fan performance curves and the aerodynamic noise at the fan and motor surfaces using the Broadband Noise Source Model (BNS) as the acoustics model and the Transition SST as the turbulence model. Both algorithms are implemented in the commercial code Fluent 19.0. Also with these models will be analyzed two noise reduction features inspired by the characteristics of the owls' feathers, which are responsible for a "silent" flight. These features, were compared with the regular fan model, and due to the self oscillation of the trailing edge an two-way transient Fluid Structure Interaction (FSI) numerical simulation will be used. As a final step, the dimpled fan will be replicated at real scale, two types of stickers with cavities with the similar parameters of the optimized pattern were applied in the original fan. The prototype will be installed within the heat pump unit and measurements in a semi-anechoic chamber will be conducted, so the noise levels of the dimpled fan could be compared to the reference model.

Chapter 2

State of the Art

2.1 Noise Mitigation Technologies for Turbomachinery

In this chapter, a review of recent research in noise reduction mechanism in aircraft turbofan engine, wind turbine and unmannedaerial systems is presented.

2.1.1 Aircraft Turbofan Engine

An aeroplane travels through the air using a propulsion system capable of generating thrust. Nowadays, most airplanes are equipped with a turbofan engine, capable of generating high performance and low noise, while maintaining fuel efficiency. The turbofan works as follows: the air captured at the engine inlet goes through a fan, followed by a compressor, and finally the burner where the air is mixed with the fuel and the combustion occurs. The different components of an turbofan engine can be observed in the Figure 2.1. Studies have shown that fans dominate total engine noise during take-off and approach to landing, as can be observed in Figure 2.2.

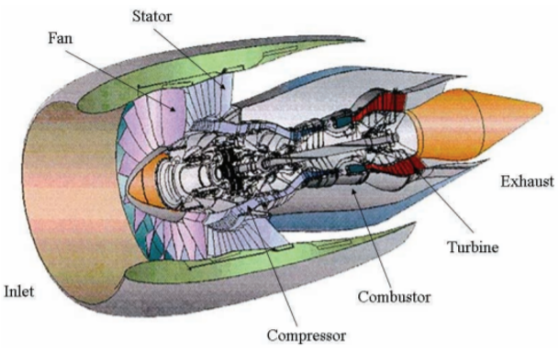

Figure 2.1: Aircraft turbofan engine components [13].

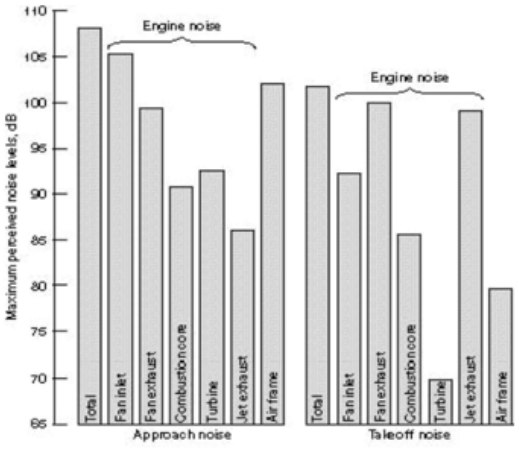

Figure 2.2: Breakdown of the noise components of a typical turbofan [14].

Two innovative fan noise reduction concepts have been introduced by NASA - the soft vanes and over-the-rotor metal foam liners [15]. Both of the concepts provide acoustic

absorption by the introduction of viscous dissipation at internal surfaces (chamber walls for soft vanes, and structural ligaments for the foam) and at the same time providing pressure-releasing surfaces in the near-field of the noise generation process, reducing radiation efficiency [15].

The first application of this concept is the soft vane stator, where a fan exit guide vanes presents a suitable impedance boundary condition leading to surface softening. This is achieved with the placement of porous surfaces to allow communication between pressure fluctuations at the vane surface and multiple internal resonant chambers. Multiple configurations were tested in order to achieve the desired surface impedance. The final design has a porous surface between 20% and 50% of the chord length of the pressure surface of the vane, with the rest being used for the placement of four internal chambers (Figure 2.4). The final configuration is shown in the Figure 2.3 allowing an attenuation of 3 dB over the entire frequency range [16].

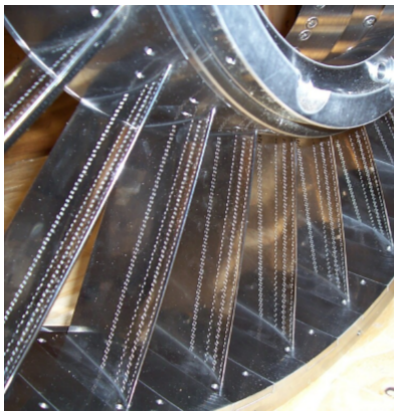

Figure 2.3: Photographs of the installed soft vanes stator [16].

Figure 2.4: Open (no end cap) soft vane configuration; four internal chambers [16].

The second technique used for noise reduction is the placement of a metallic foam embedded in fan duct (see Figure 2.5). The foam has the effect of acoustic absorption through the viscous losses generated by the interaction of the tip leakage flow with the interior of the metallic structure surface. The optimized solution is made with an cobalt allow (Haynes 25) with 80 pores per inch and 8% density. The experimental results showed a 2.5 dB attenuation for frequencies above 2 BPF [16]. Following studies showed a loss from 2.76% to 8.75% with the implementation of this type of treatments. A lighter alloy was implement to overcome this efficiency penalty, but fabrication of the treatments was problematic, and increased noise due to fabrication flaws remained a concern.

In order to find a solution which do not substantially increase the weight of the turbofan one particular design was created. This over-the-rotor treatment consist in a number of mesh-caps embedded into a honeycomb core as illustrated in Figure 2.6. This concept allows a variable depth creating the desired distributed impedance, reducing 1 dB between the frequency range of 1 BPF to 3 BPF, without any efficiency loss. The focus of the current research is the reduction of its manufacturing complexity [17].

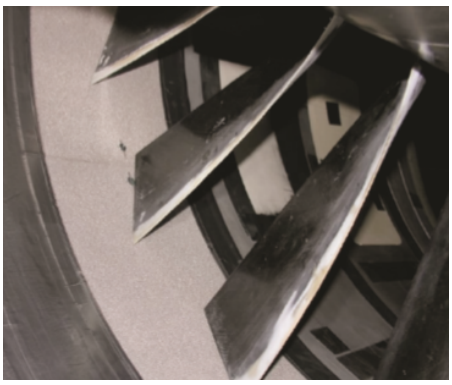

Figure 2.5: Over-the-rotor metal foam liner [15].

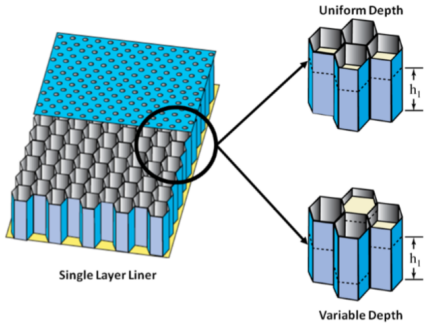

Figure 2.6: Single layer of honeycomb with variable impedance inside the mesh-cap insertion [18].

2.1.2 Wind turbine

Noise generation from wind turbines is divided into two types: mechanical and aerodynamic. The sources of aerodynamic noise in wind turbines are very similar to the axial fan. Therefore, a detailed explanation of the different sources of noise generation in this type of turbomachines is discussed in Chapter 3.4.

The inlet flow turbulence is considered one of the major sources of noise in turbomachines. Although this type of noise source is difficult to mitigate, the introduction of leading edge serration shows slight improvements in noise generation of this phenomenon [19]. Different designs of leading edge serration has been researched with a focus on bio-inspired solutions. Experimental studies by Hansen et al. [18] show that when turbercles (inspired by the whale fin) are placed at the leading edge of an airfoil (Figure 2.7), the tonal component generated is strongly reduced and shifted to higher frequencies, in addition an reduction of broadband noise at frequencies near to the shifted peaks was observed (Figure 2.8). Tubercles with larger amplitude and small wavelength found to be the most effective in noise reduction and also with a lower lift loss associated. It is postulated that the turbercles create vortexes that increase the momentum exchange within the boundary layer, changing its stability characteristics and frequency of velocity fluctuations in the shear layer near the trailing edge.

Figure 2.7: Section view of the 0021 NACA airfoil with tubercles [18].

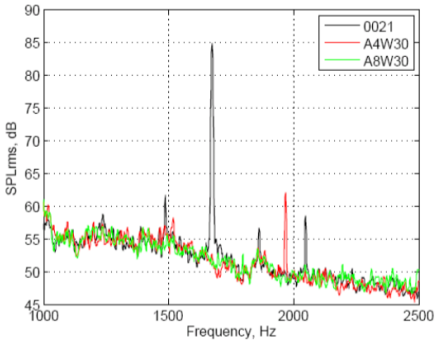

Figure 2.8: SPL vs. Frequency for Variation of Amplitude of Tubercles and the standard 0021 NACA airfoil [18].

The presence of turbulent boundary layer next to the trailing edge is responsible for one of the major causes of broadband noise in wind turbines. This phenomenon will be explained in detail in Chapter 3.4. Recent studies [20] shows that in the presence of a porous trailing edge has the effect of balancing the dynamic pressure mismatch between suction and pressure side at the trailing edge. Different porous NiCrAl foams (Figure 2.10) with cell diameters of 550 μm to 800 μm were tested, according with the following configuration represent in the Figure 2.9. It was found that larger cell size are more suitable for higher angles of attack, showing a reduction of up to 18 dB at higher frequencies. For lower angles of attack, the noise reduction was not as significant, with a reduction of 5 dB. An increase in extension from 10% to 20% of the chord length showed little to no effect on the coefficient of lift; in other hand, an reduction in low frequency noise was observed.

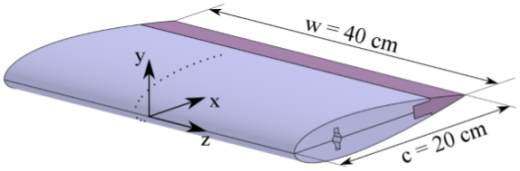

Figure 2.9: Sketch of the NACA 0018 airfoil with porous insert. The NiCrAl trailing edge is represented by the purple region while the grey region represents the aluminum body [20].

Figure 2.10: Photography of a metal foam trailing edge [20].

Similar studies were carried out at the acoustic wind tunnel of the German Aerospace Center for high Reynolds number (1.2 million) and larger airfoils [21]. These studies compare metal foam with serration in the trailing edge and the original airfoil profile. The results can be observed in the Figure 2.11, where the far-field, third-octave band spectra for have been normalized with the values of the untreated blade. The negative values represent noise reduction, while the positive values represent an increase in noise.

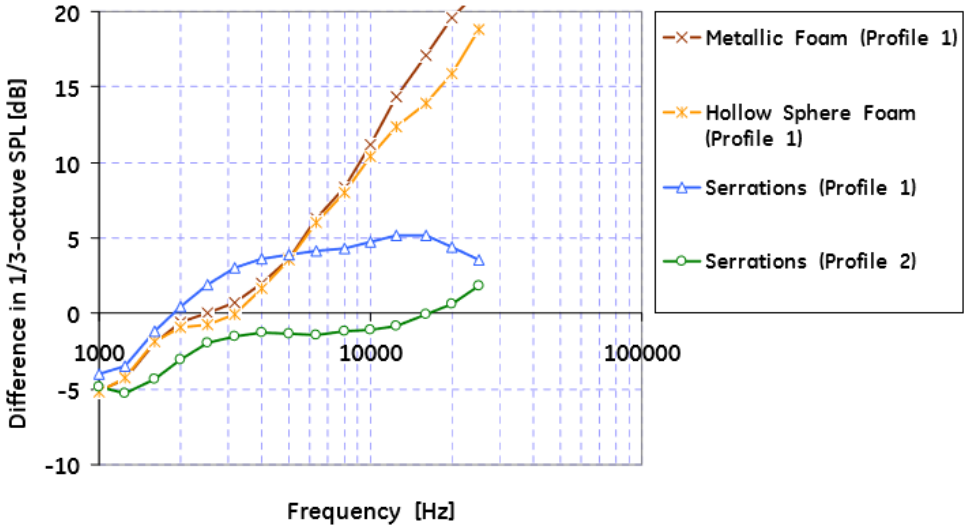

Figure 2.11: Noise reduction comparison between different trailing edge modifications [20].

Contrary to the studies presented for low-medium Reynolds number previously mentioned, the metal foam trailing edge presents a noise reduction up to 3 dB at low frequencies (1-3kHz), followed by an constant noise increase at higher frequencies. The trailing edge with serrations in the airfoil profile 2 presents lower noise emission for a broad range of frequencies, with only an increase up to 5 dB at high frequencies [21].

2.1.3 UAVs

The use of different blade shapes shows a potential reduction of 1 to 3 dB. There is a popular geometry developed in the 1970s and still used to this date - the q-tip (Figure 2.12). This geometry uses 90º tips to reduce the tip vortex, leading to the noise reduction. This geometry can be seen in Figure 2.12. Recent and innovative advances were accomplished with the use of shrouds made with absorption materials (Figure 2.13), promoting the reduction of low to mid frequency noise and adding more safety to the UAVs [22].

Figure 2.12: Q-tip style propeller used in the DJI Mavic Pro [22].

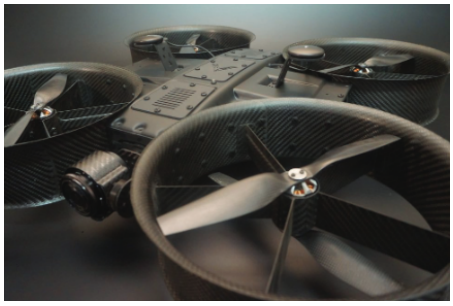

Figure 2.13: Lightweight fan shrouds comprising sound-absorbing acoustic materials (Aerotestra MK10) [22].

Intentionally blank page.

Chapter 3

Theoretical Background

For a better understanding of this work, some theoretical principles of fluid mechanics, turbomachinery and aeroacoustics will be introduced. The present section will present basic fluid dynamics equations. Subsequently, the turbomachinery equations and boundary layer separation conditions will be derived. Finally, the axial fan noise generating mechanisms and its sources will be explained and potential solutions will be presented.

3.1 Basics of Fluid Mechanics

In this chapter a summary of the basic equations of fluid dynamics is presented, and the following laws are introduced: the mass conservation equation, the moment conservation equation and the energy conservation equation. Then the occurrence of flow separation will be explained.

Governing Equations

A three-dimensional fluid dynamics problem can be generally expressed mathematically by the fundamental equations. Physical variables such as ρ and the velocity vector $\vec{v}$ decomposed into three velocity components u, v, w described in dependency of the Cartesian coordinates x, y and z must be have to solved for these type of problems [23]. The following conservation laws have to be applied for every fluid mechanical problem:

- Conservation of mass
- Conservation of energy
- Conservation of momentum

These conservation laws state that neither mass, momentum or energy can be created or destroyed on a close system or within a fixed control volume. The laws can be presented in the Euler form to mathematically relate the field quantities [23]. The conservation of mass, which is mathematically described by the continuity equation, defines that temporal change of the mass within a volume element corresponds to the difference between the incoming mass flows and the outgoing mass flows [23]. This relationship can be generally expressed as:

$$\frac{\partial \rho}{\partial t} + \frac{\partial (\rho u_i)}{\partial u_i} = 0 \tag{3.1}$$

Equation 3.1 can be written in Cartesian coordinates in the following form:

$$\frac{\partial}{\partial t}(\rho) + \frac{\partial}{\partial x}(\rho \cdot u) + \frac{\partial}{\partial y}(\rho \cdot v) + \frac{\partial}{\partial z}(\rho \cdot w) = 0 \tag{3.2}$$

In the case of steady (negligible temporal change) and incompressible (constant density) flow, the incoming and outgoing mass flows are having the same magnitude for a given control volume [23]. In this case, can be simplified into the following form:

$$\frac{\partial(u_i)}{\partial x_i} = 0 \tag{3.3}$$

The momentum equation in fluid mechanics can be derived by applying the Newton's second law to a model of flow, which vectorially expresses that the net force on a fluid element is equal to the product of its mass and its acceleration. Two sources of this force can be understood by body forces and surface forces, respectively. The body forces are the forces that are acting directly on the volumetric mass of the fluid element. The surface forces act on the surface of the fluid element. One of the sources for the surface forces is the pressure distribution on the surface, which result in pressure force. Another source of this are the frictional forces, which are produced by means of normal and shear stress distributions on the surface. The equation of momentum can be expressed as following in conservation form [24]:

$$\underbrace{\rho\frac{\partial(u_j)}{\partial t}}_{\substack{\text{temporal}\\ \text{momentum}\\ \text{change}}} + \underbrace{\rho u_i\frac{\partial u_j}{\partial x_i}}_{\substack{\text{momentum}\\ \text{change of mass}\\ \text{flows by}\\ \text{convection}}} = - \underbrace{\frac{\partial p}{\partial x_j}}_{\substack{\text{pressure}\\ \text{force}}} - \underbrace{\frac{\partial \tau_{ij}}{\partial x_i}}_{\substack{\text{friction}\\ \text{forces}}} + \underbrace{\rho g_j}_{\substack{\text{gravitational}\\ \text{force}}} \tag{3.4}$$

Equation 3.4 can be shown in following equations for x,y and z Cartesian coordinates [24]:

$$\frac{\partial}{\partial t}(\rho \cdot u) + \frac{\partial}{\partial x}(\rho \cdot u^2 + p - \tau_{xx}) + \frac{\partial}{\partial y}(\rho \cdot u \cdot v - \tau_{yx}) + \frac{\partial}{\partial z}(\rho \cdot u \cdot w - \tau_{zx}) - \rho \cdot g_x = 0 \tag{3.5}$$

$$\frac{\partial}{\partial t}(\rho \cdot v) + \frac{\partial}{\partial x}(\rho \cdot v \cdot u - \tau_{xy}) + \frac{\partial}{\partial y}(\rho \cdot v^2 + p \cdot v - \tau_{yy}) + \frac{\partial}{\partial z}(\rho \cdot v \cdot w - \tau_{zy}) - \rho \cdot g_y = 0 \tag{3.6}$$

$$\frac{\partial}{\partial t}(\rho \cdot w) + \frac{\partial}{\partial x}(\rho \cdot w \cdot u - \tau_{xz}) + \frac{\partial}{\partial y}(\rho \cdot w \cdot v - \tau_{yz}) + \frac{\partial}{\partial z}(\rho \cdot w^2 + p - \tau_{zz}) - \rho \cdot g_z = 0 \tag{3.7}$$

In the equations above, the term of the viscous stress τ_{ij}, which is a tensor, can be considered to be symmetrical, which indicates $\mid \tau_{ij} \mid = \mid \tau_{ji} \mid$. An equation is necessary to express τ_{ij} in terms of $\partial u_j / \partial x_i$. Under the assumption of the fluid to be Newtonian, where the shear stress is proportional to the time rate of strain [23], the following equation can be expressed:

$$\tau_{ij} = -\mu(\frac{\partial u_j}{\partial x_i} + \frac{\partial u_i}{\partial x_j}) + \frac{2}{3}\sigma_{ij}\mu\frac{\partial u_k}{\partial x_k} \tag{3.8}$$

where μ is the dynamic stress viscosity and σ_{ij} is the Kronecker delta. The index k symbolizes the compressible part of the equation, which exists due to the increase in surface area. By combining the continuity equation, the three momentum equations, the six equations for the viscous stress with the thermal energy equation and the equation of state of gas, a closed system of partial differential equations is obtained. This is described by the Navier-Stokes equations under the assumptions of incompressible and Newtonian fluids as following:

$$\rho(\frac{\partial u_j}{\partial t} + u_i\frac{\partial u_j}{\partial x_i}) = -\frac{\partial p}{\partial x_j} - \mu\frac{\partial^2 u_j}{\partial {x^2}_i} + \rho g_j \tag{3.9}$$

Together with the continuity equation, this equation system consists of four equations for four unknowns, which are the pressure p and the three velocity components u, v, and w. By defining suitable initial and the boundary conditions, this equation system can be principally used to solve a flow problem. A complete partial differential equations system can be obtained through the continuity equation and the momentum equations for a constant-density fluid. The mechanical energy equation can be derived by multiplying the momentum equation in Equation 3.4 by u_j. The general form of mechanical energy equation can therefore be expressed as:

$$\underbrace{\rho\frac{D}{Dt}(\frac{1}{2}u_j^2 + G)}_{\text{temporal change of kinetic and potential energy}} = -\underbrace{\frac{\partial(pu_j)}{\partial x_j}}_{\text{pressure energy difference}} + \underbrace{p\frac{\partial u_j}{\partial x_j}}_{\text{work done during expansion}} - \underbrace{\frac{\partial \tau_{ij}u_j}{\partial x_i}}_{\text{kinetic energy difference}} + \underbrace{\tau_{ij}\frac{\partial u_j}{\partial x_i}}_{\text{dissipation of mechanical energy into heat}} \tag{3.10}$$

where G is a potential which is derived from the gravitational acceleration g_j by following:

$$g_j = -\frac{\partial G}{\partial x_j} \tag{3.11}$$

From the general equation of the mechanical energy, a special form can be derived, namely the Bernoulli's equation:

$$\frac{p}{\rho} + \frac{1}{2}u_j^2 + G = constant \tag{3.12}$$

Some assumptions have been made in deriving this equation, such as for Newtonian fluids, where $\tau_{ij} = 0$, for steady flow, which includes $\partial p/\partial t$=0, and for incompressibility, that considers ρ to be constant. However, this form of equation can be used in many engineering applications. The change in term of the gravitational force is usually negligible in many applications, because the change of this term is not substantial compared to the other terms in the equation. With this, the simplified Bernoulli's equation can be expressed as:

$$p_{total} = p_{static} + p_{dynamic} = p_{static} + \frac{\rho}{2}c^2 = constant \tag{3.13}$$

3.2 Flow Separation

3.2.1 Two-Dimensional Boundary Layer Separation

Flow separation is defined as separation of the boundary layer [23]. A flow tends to separate from its own flow path during a sudden deceleration, a high wall friction and high pressure differences. The flow field will be pushed away from the surface of the body contour. In the boundary layer, a fluid will be decelerated due to its low kinetic energy. Hence, if there is a zone in the flow direction along the body contour with high pressure available, the fluid with low kinetic energy in the boundary layer is not able to penetrate the high-pressure zone. Accordingly, the boundary layer starts to disconnect from its zone, to separate from the wall, and tends into the inner flow field [23].

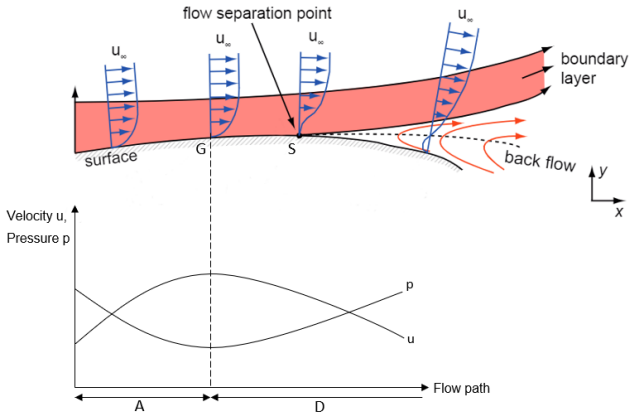

Figure 3.1: Occurrence of flow separation (adapted from [25]).

The schematic occurrence of the flow separation is illustrated in Figure 3.1. In zone A, the fluid will be accelerated due to the pressure drop. At Point G, the pressure is minimum and the corresponding velocity is maximum. At this position, the point of inflection of the velocity profile is exactly at the wall and there can be no separation here. At the beginning of zone D, the fluid starts to decelerate and therefore the pressure rises again. From the beginning of the zone D onwards, the boundary layer gets thicker due to the continuously lost kinetic energy and the point of inflection is shifted into the boundary layer. Yet, the flow is not separated due to the weak pressure gradient [25]. The pressure keeps increasing up to the point S. The point S is the separation point which is defined as the boundary between forward flow and backflow. At this point, the tangent at the velocity profile is exactly normal to the body contour, and the wall shear (skin friction) stress τ_w is zero [23]:

$$\tau_w = \mu \frac{\partial u}{\partial y} = 0 \tag{3.14}$$

From the point S onwards, flow separation occurs, the flow keeps decelerating up to a certain location where zero velocity is reached, and afterwards the backflow occurs. The occurrence of the flow separation consumes high energy to produce the separation vortex and the highly turbulent flow, and therefore the mechanical dissipation loss and noise generation is substantial [25].

3.2.2 Three-Dimensional Boundary Layer Separation

When the axial fan is rotating, the direction and velocity of air were constantly changing, this mechanism generates a transverse pressure gradient (Figure 3.2), leading to a three-dimensional flow separation [26].

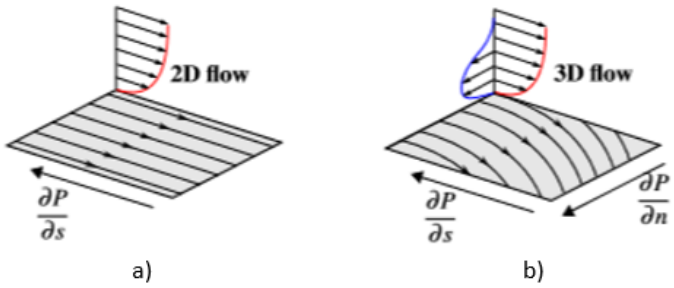

Figure 3.2: Effect of adverse pressure gradient on velocity streamlines of: a) 2D flow and b) 3D flow with formation of transverse velocity distribution [26].

In contrast to the phenomenon described in the previous section, three-dimensional separation do not behave in a simple and controlled way, making it difficult to identify. Three-dimensional separation can happen without the presence of reverse flow or a non zero skin friction. Experiments also show to be independent of the number of Reynolds as opposed to two-dimensional separation [27].

Three-dimensional flow separation tend to separate along lines (Figure 3.3). This phenomenon can be identified by the convergence or divergence of the wall-shear vector field (also mentioned as skin-friction lines) under the influence of a transverse pressure gradient and viscous forces. The kinematics of complex flows can be described by critical points that are at the basis of the skin-friction vector field [28]. First, the friction field $\vec{\tau}$ needs to be constructed to trace skin friction lines trajectories, when a point satisfies Equation 3.15 it is considered an critical point, the point where the skin friction line vanishes altogether [28, 29].

$$\tau_x = \tau_y = 0 \tag{3.15}$$

Critical points can be classified into two categories:

- nodes
- saddle points

A node is a common point of different skin friction lines, all of which are tangent to a single straight line. There are two different types of nodes described as follows [28, 29]:

- The saddle point (Figure 3.5)- Point where two critical skin friction lines pass, acting as barriers in the field for other skin friction lines, making one set of streamlines inaccessible to the adjacent set. In the vinicity of a critical point, all skin friction lines tend to avoid contact with the critical point and only two lines pass through the critical point. These lines are called dividing lines.

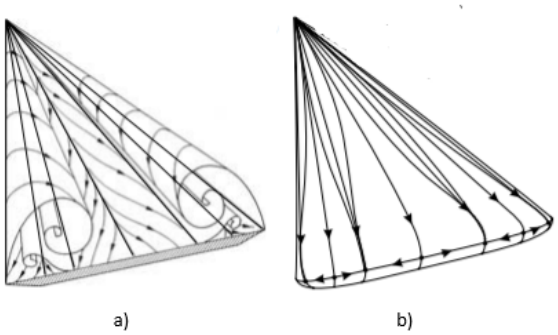

Figure 3.3: a) Illustration of separation on a delta wing, b) Skin-friction field representing the flow separation (Adapted from [27]).

- Spiral node or focus of separation (Figure 3.4)- Point which has an infinite number of skin lines around the node like an vortex, the arrows indicate its motion. An attachment focus is set when motion goes away from the vortex or either into it, defining a focus of separation.

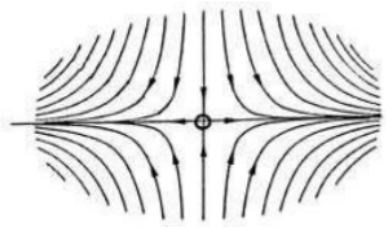

Figure 3.4: Spiral node or focus of separation [29].

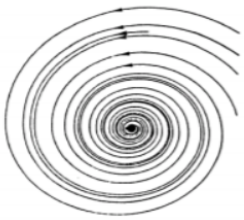

Figure 3.5: Saddle point [29].

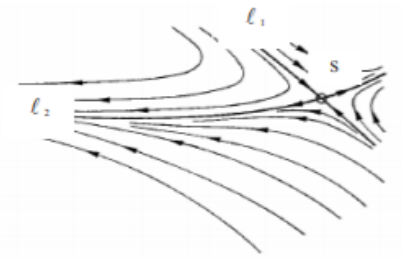

Figure 3.6: Node of separation [27].

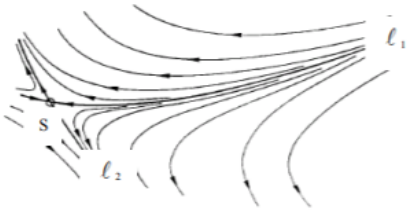

Figure 3.7: Node of attachment [27].

The Figure 3.6 shows two dividing skin friction lines defined as $L1$ and $L2$. Line $L1$ is coming from the upstream an the other from the opposite end, merging at the saddle point S, and a group of lines turns towards the left and other to the right. After being separated, the skin friction lines tend to follow the direction of $L2$. At the approach of the line $L2$ the other lines on the surface will separate. In this phenomenon, the viscous layer of the fluid represented by the group of skin friction lines will be leave

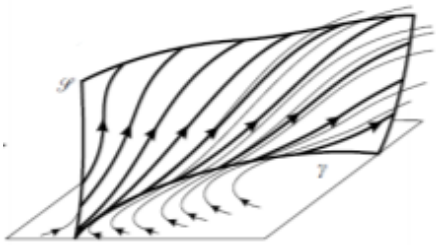

Figure 3.8: Separation surface ζ emanating from a separation line γ [27].

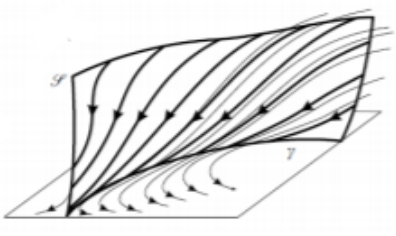

Figure 3.9: Reattachment surface ζ emanating from a reattachment line γ [27].

transversely along the line $L2$ to mix with the non-viscous flow (Figure 4.6). The Figure 3.7 represents the same principle for the attachment of the flow [29].

3.3 Fundamentals of Turbomachinery

In the following section is presented the most popular technique of axial fan design - the meridional flow analysis for axial fans. The concept behind this technique is the approximation of the fully three-dimensional flow as two-dimensional averaged meridional flow, with constant radial velocity (free vortex design). The technique defines a set of meridional surfaces with direction equal to the flow, for an axial fan it is expected that the majority of the flow follows a circular path when seen in the rotating frame. The intersection between the blade and the meridional surface creates a curved airfoil for each blade. Then the curved airfoils have to be unwrapped from the cylindrical coordinate systems to a cartesian one. In the Cartesian form the different velocity components can be analysed using the velocity triangle [4], shown in Figure 3.10.

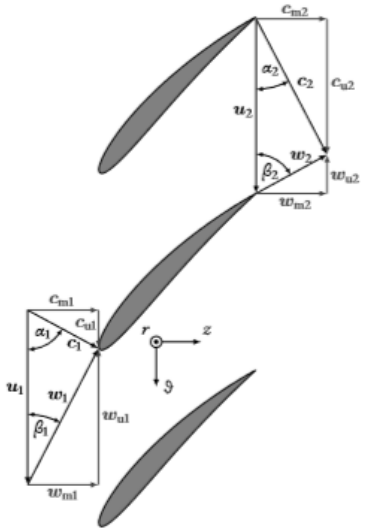

Figure 3.10: Inlet and outlet velocity diagram of an axial blade row with r=constant [4].

Basic equations of energy conversion of the axial fan are presented according to the flow kinematics within a axial fan row of constant radius. Where the fluid has the

axial direction from the left to the right. Therefore, on the left side the inlet velocity is illustrated and on the right side the outlet velocity diagram [4]. The absolute velocity c denotes the velocity of a fluid particle in the global coordinate system, with coordinates r, υ, z. Where, the absolute velocity c is related to the relative velocity w with respect to the rotating coordinate system and the circumferential velocity of the fan blades u,

$$\vec{c} = \vec{u} + \vec{v} \tag{3.16}$$

The absolute velocity c can be written as the vector sum of its radial component c_m and the circumferential component c_u [4].

$$c = c_m + c_u \tag{3.17}$$

where the meridional velocity c_m lies in the meridional plane, rz plane and the circumferential velocity c is aligned with the υ-axis. In the same way the relative velocity w can be expressed in the same components.

$$w = w_m + w_u \tag{3.18}$$

The angular correlation between the velocities c, w and u is given by the relative flow angle β which represents the angle between the relative velocity w and the circumferential velocity u. The absolute angle α represents the angle between the absolute velocity c and the circumferential velocity u [4].

For axial fans, the magnitude of the vector u is given by the following 3.19, where r represents the radius of the section and n the rotational speed.

$$u = u_1 = u_2 = 2\pi nr \tag{3.19}$$

The magnitude of the vector c is determined with by volume flow rate $\dot{V}$ and the fan dimensions, as:

$$c_m = c_{m1} = c_{m2} = \frac{\dot{V}}{\pi(r_{tip}^2 - r_{hub}^2)} \tag{3.20}$$

In addition, from flow kinematics it follows that:

$$c_m = w_m, \tag{3.21}$$

and

$$c = \sqrt{c_m^2 + c_u^2} \tag{3.22}$$

$$c = \sqrt{w_m^2 + w_u^2} \tag{3.23}$$

The absolute flow angle α and the relative flow angle β are calculated with the following trigonometric relationship:

$$\alpha = \arctan \frac{c_m}{c_u} \tag{3.24}$$

and

$$\beta = \arctan \frac{w_m}{w_u} = \arctan \frac{c_m}{u - c_u} \tag{3.25}$$

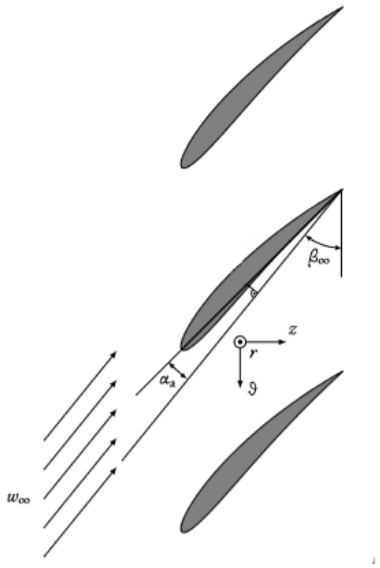

Figure 3.11: Average flow relative velocity ω_∞, and flow angle relative to the blade β_∞ of an axial blade row with r=constant [4].

The magnitude of the vectorial average relative velocity and flow angle will be derived from basic trigonometric operations.

The average flow relative velocity ω_∞ and the flow angle relative to the blade β_∞ the free flow [4]:

$$\omega_\infty = \frac{\omega_1 + \omega_2}{2} = \frac{1}{2}\sqrt{(u + \sqrt{\omega_2^2 - c_m^2})^2 + 4c_m^2} \tag{3.26}$$

$$\beta_\infty = \frac{\beta_1 + \beta_2}{2} = \arctan(\frac{2c_m}{u + \sqrt{\omega_2^2 - c_m^2})}) \tag{3.27}$$

3.4 Axial Fan Acoustics

The different noise generation mechanisms of a fan can be classified by the three fundamental noise sources, which are:

- Monopole - consequence of the blades moving through the air, creating periodic volumetric displacement fluctuations in the far-field.
- Dipole - created as a result of pressure fluctuations on the blade surface.
- Quadrupole - as a consequence of the turbulent flow.

The major differences between the noise sources are elaborated below, where the noise generation coming from an axial fan are divided into two types: the noise emitted by the geometry of the blade, which is similar to the mechanisms of noise generation of the airfoils, and the noise emitted due to the rotation motion of the fan.

3.4.1 Sound Generation Mechanisms for Airfoils

Airfoil noise is defined as the noise produced by the interaction of the turbulence produced by the boundary layer and the airfoil surface itself, considering a non turbulent inflow [30]. The different regimes of the boundary layer together with the geometrical parameters of the airfoil define the self-noise emitted.

Boundary Layer Noise

The noise emitted comes from the pressure fluctuation within the turbulent boundary layer. The noise is characterized by being a broadband noise and it is expected to radiate from the middle part of the airfoil [4]. Boundary layer noise depends on the following factors: angle of attack, Reynolds number and thickness of the turbulent boundary layer [30].

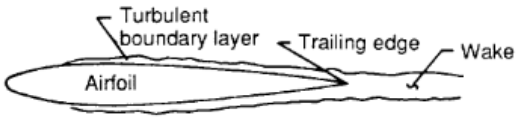

Figure 3.12: Schematic representation of the sound generation mechanism boundary layer noise [30].

Boundary Layer Separation - Stall Noise

One of the major focuses of this work is the control of boundary layer separation. The literature mentions that when the flow is slightly separated it becomes the dominant source of noise due to the complex flow formed [4]. The noise generated is expected to radiate from the trailing edge while in fully developed stall conditions is distributed throughout the suction side [4].

When the aerodynamic stall is triggered it is expected an increase of more than 10 dB in relation to the turbulent boundary layer phenomenon [30].

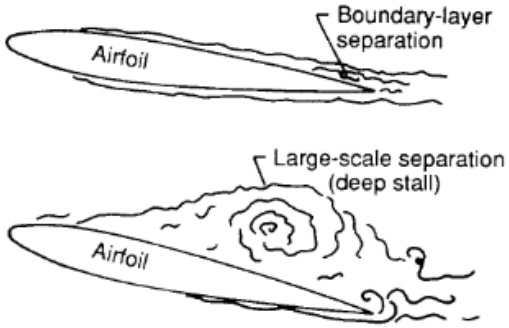

Figure 3.13: Schematic representation of the sound generation mechanism due to flow separation and large-scale separation (stall) [30].

Trailing Edge Noise

Trailing edge noise is directly related to the occurrence of vortex shedding. There are two different types of vortex shedding, which depend on the nature of the boundary layer and the geometry of the trailing edge.

When a turbulent boundary layer passes through the trailing edge, it creates eddies that interact with each other, generating a broadband noise with a dominant frequency that can be calculated by the non-dimensional Strouhal ratio.

$$St = \frac{fL}{v} \tag{3.28}$$

Where f is the vortex shedding frequency, L the characteristic length and v is the local flow velocity [31].

When the boundary layer in laminar regime interacts with the trailing edge strong and clean vortexes are generated, that will create a feedback loop with the boundary layer, resulting in instabilities waves that generates tonal noise [32].

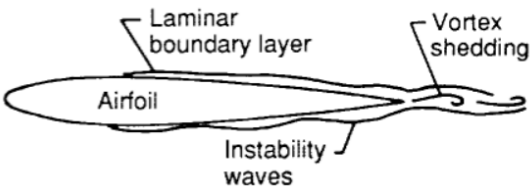

Figure 3.14: Schematic representation of the sound generation mechanism of trailing edge noise and vortex shedding sound (excited by instability effects in the laminar boundary layer) [30].

Turbulence Ingestion Noise

The inflow conditions have a major impact on the noise emitted by an axial fan. The ingestion noise is emitted by two inflow conditions: inflow turbulence intensity, a non-uniform velocity profile or the combination of both [4]. The inflow turbulence is often generated by heat exchangers, struts and other installation that lead to a substantial increase of broadband noise. The non-uniform velocity profile are generated by obstacles that induce inhomogeneous velocity profile upstream the fan, such as bends. This condition creates unsteady blade forces leading to eddies that are passed multiple times by fan blades generating low-frequencie noise [4].

Schematic Acoustic Spectrum of an Airfoil

In the Figure 3.15 a summary of sound sources of airfoils represented as a schematic acoustic spectrum can be seen. It is possible to observe that the low-frequency noise is dominated by the turbulence ingestion noise, while the mid high frequency noise derives mostly from trailing edge sources.

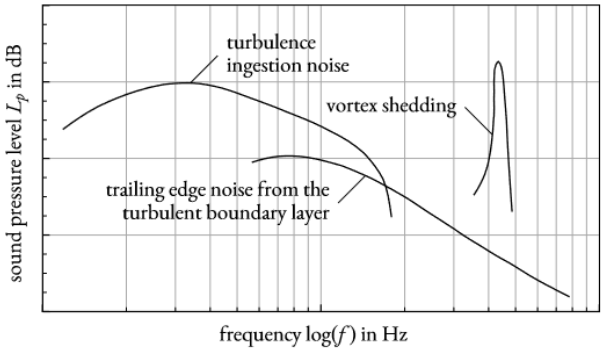

Figure 3.15: Schematic acoustic spectrum of an airfoil [4].

3.4.2 Sound Generation Mechanisms for Low-Speed Fans

The noise emitted from an axial fan has the airfoil self noise component, the of turbulence ingestion noise and other mechanisms due to the rotation movement of the blades. This mechanism will be presented in the next section.

Reverse Tip Leakage

Tip leakage flow is an unavoidable phenomenon that prevents ideal flow conditions around an aerodynamic body, causing a loss of efficiency and increased noise emitted [33]. This phenomenon is characterized by the passage of fluid from the pressure side (high pressure) of the fan towards its suction side (low pressure) through the tip leakage gap [34]. Therefore, the leakage flow generates a moment to the vortex generating a roll-up vortex that ends up blocking the flow in the tip clearance. The vortex roll-up, when interacting with the shroud and with the fan surface itself, generates noise from the dissipation of momentum energy into acoustic energy [34]. Reducing the size of the vortex generated involves controlling the size of the tip clearance or changing the geometry of the blade tip [35]. The literature references the use of wingles in order to decrease the difference of pressures between the fan surfaces. A reduction in the gap size between the blade and the shroud of 1.34% leads to an efficiency increase of 17.85% at high speeds [35].

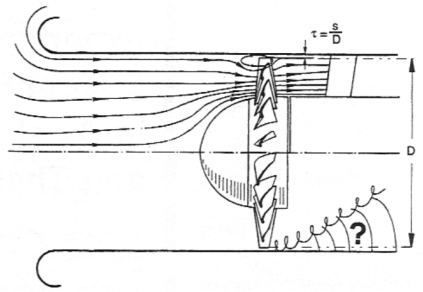

Figure 3.16: Schematic representation of the secondary flow formed in the tip leakage gap due to the difference of pressures between the fan surfaces [36].

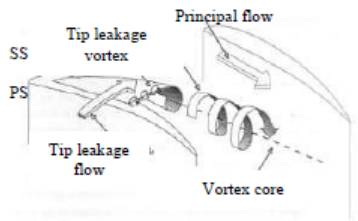

Figure 3.17: Roll up of the tip leakage vortex from the pressure side to the suction side of a compressor blade [29].

Hub Corner Separation

The physical mechanism associated to the hub corner separation is the reverse of the flow in great magnitude at the junction of the blade and the hub, thus generating a vortex between these two regions.

This phenomenon begins with the interaction of the boundary layer developed on suction side of the blade with the boundary layer developed in hub wall, with the consequent increasing of the boundary layer thickness in the junction. The pressure gradient in this region produce a three-dimensional separation in the junction near the trailing edge, generating a vortex that blocks the main flow [26, 29] (Figure 3.18). This effects the stability of the blade loading, and when the fan operates under its stability limit the hub corner separation tends to grow, resulting in stall (Figure 3.19).

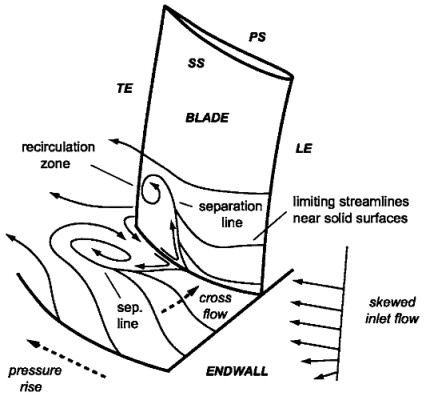

Figure 3.18: Vortex hub-corner formation schematic [29].

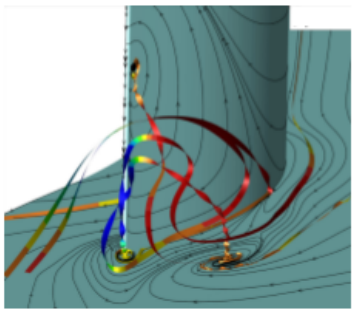

Figure 3.19: Hub corner separation represented with skin-friction lines and the focus of separation generating vortexes surfaces [26].

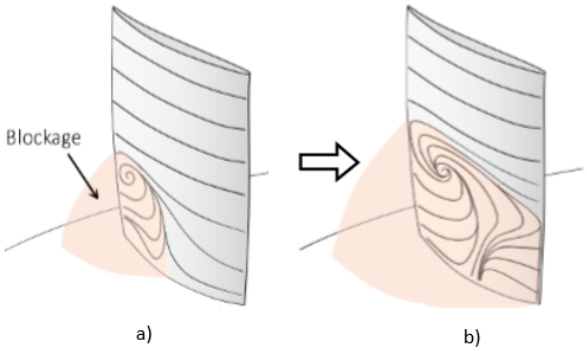

Figure 3.20: Blockage promoted in a blade by a) hub corner separation and b) aerodynamic stall [26].

3.4.3 Noise Reduction Features for Axial Fans

Trailing Edge Serrations

Trailing edge serrations are applied to airfoils and axial fans in order to reduce wake separation. The majority of the literature on this subject refers a reduction of 2 to 6 dB with a greater emphasis on high frequencies [37]. The mechanism for reducing the wake occurs when the flow from the suction side of the blade is mixed with the flow of the pressure side, generating a conter-rotating vortex compared to the vortexes in the boundary layer, energizing the boundary layer [37]. Studies between different types of serrations show that the geometries that energize closer to the tip of the fan have a major impact on the reduction of the vortex roll-up and the vortex shedding wake, as can be seen in Figure 3.21.

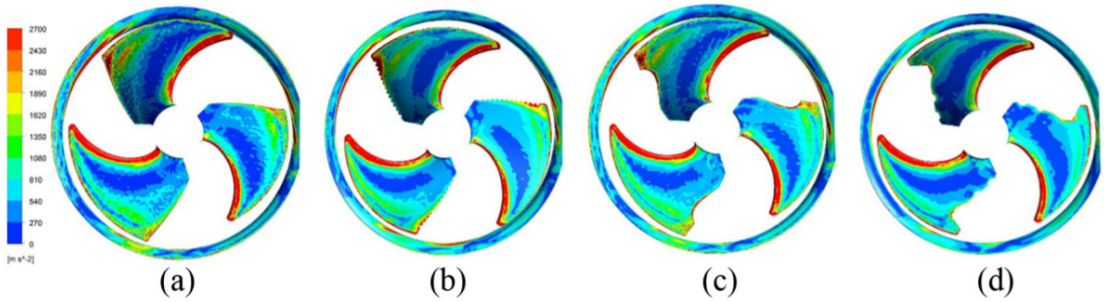

Figure 3.21: Distribution of vorticity on the pressure side for different axial fans: (a) impeller 1, (b) impeller 2, (c) impeller 3, and (d) impeller 4 [37].

Winglet

Noise prevention techniques focus on the vortex roll-up by introducing winglets. The winglet prevents or groves the vortex resulting in a decrease of speed. However, the vortex continues to interact with the suction side, creating a blockage [38]. The study by Nashimoto et al. [38] on this subject refers a reduction of 1 dB in the frequency range under 6 kHz, but conversely, tended to increase slightly in the range over 6 kHz.

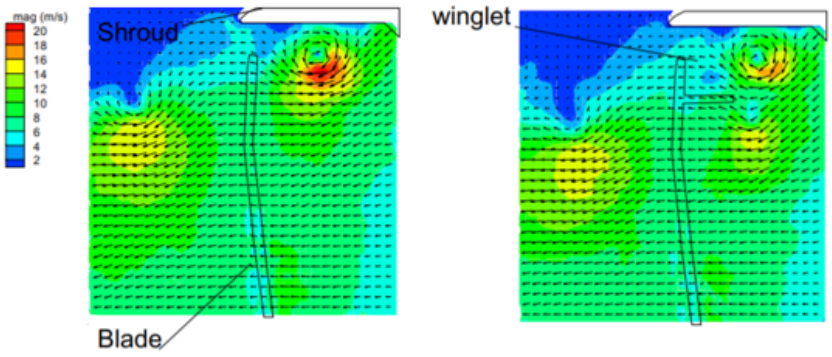

Figure 3.22: Velocity profile and magnitude near the shroud a) without winglet and b) with winglet [38].

Dimples

The acoustic study done by Santos [12] in the application of dimples on the Bosch's axial fan showed promising results as a high potential noise reduction feature. The numerical study showed a reduction of 0.8 average acoustic power level and the experimental study showed a potential reduction up to 3.7 dB (A). The theory proposed by Santos argues that dimples dissipate the flow turbulence into small eddies, which have low energy content, as a result the turbulent kinetic energy decreases in the critical areas (Figure 3.23). It is also suggested that dimples reduces the flow separation on the fan blade surface, making them a suitable solution for low airflow where a greater separation of the flow is verified. Due to the fact that it is an original idea of the previous work, an in-depth study will be conducted about the use of dimples for the control of the boundary layer separation and its effect on noise.

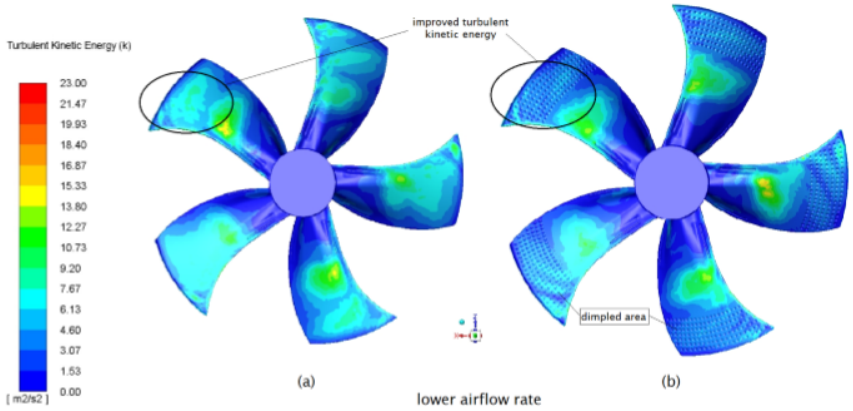

Figure 3.23: Turbulent kinetic energy contours (k) on the suction side of: a) the original fan, b) the dimpled fan [12] .

Intentionally blank page.

Chapter 4

Flow Separation Control Using Dimples

As mentioned before, the flow separation contributes greatly to the aerodynamics noise. The previous research done on the heat pump fan by Santos [12] showed a great potential of noise reduction with the placement of dimples to specific regions of blade surface. The experimental study of a reduced size 3D printed fan model with dimples showed a reduction of up to 3.7 dB(A), as mentioned in Section 3.4.3. The focus of this chapter is the detailed study of the previous research on dimples. Initially, the effect of the dimples in different applications will be presented. Then, the influence of the size, geometry, pattern and location will be analyzed in a two dimensional domain analysis. With the conclusions of this study, the optimized solution will be implemented in the original fan, then different fan curves and noise curve will be analyzed in order to evaluate the influence of the dimples in a complex three-dimensional flow.

4.1 The Effect of Dimples in Different Applications

In recent years there has been a great effort in the study of mechanisms capable of controling the formation of the boundary layer. The use of dimples has gained a lot of attention in terms of research due to its success in controlling the boundary layer in golf balls reducing the pressure drag on a sphere as much as 50% as compared to a smooth surface [39].

One of the famous investigations of the flow features near surfaces with spherical dimples was made by Bearman and Harvey [41]. They found that only one dimple is necessary for separation location shift by a few degrees if the dimple was located at approximately 80 deg from the front stagnation point, showing that the location of the dimple is a critical optimization factor.

Dimples due to its geometry, when the flow enters inside the dimple its generated a re-circulation bubble. The bubble has circulatory flow inside that will be responsible of generating discrete vortices which energizes the boundary layer flow immediately after the dimple. The end result is a turbulent boundary layer with more momentum close to the surface, leading to a more distance traveled until it starts to decelerate. When this happens, the adverse pressure gradient will be able to detach the flow [39, 40, 42]. However, the skin friction is increased due to the presence of a turbulent boundary layer.

Multiple studies on NACA airfoils showed that the position and dimensions of the

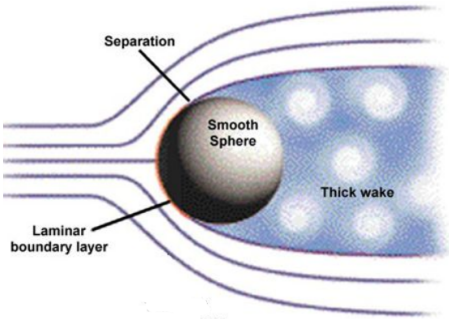

Figure 4.1: Schematic representation of flow separation on a smooth sphere [40].

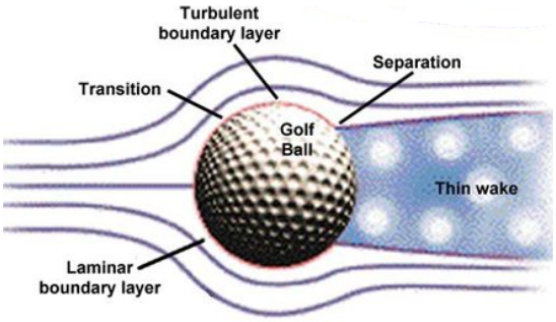

Figure 4.2: Schematic diagram of the mechanism that promotes the control of the boundary layer formation on a golf ball [40].

dimple affects the drag and lift characteristics, Loss et al. [40] showed that dimples reduce separation when positioned upstream from the location of the flow separation. Research on blade turbines done by Rouser [42] studied the effect of the dimple location on the blade with an inlet of 25 000 Reynolds number. The author tested different locations for the placement of one dimple and found that at 65% of the chord length the maximum boundary layer shift was achieved. Casey [42] continued Rouser research by showing that the use of different dimple patterns have a positive effect on flow separation control.

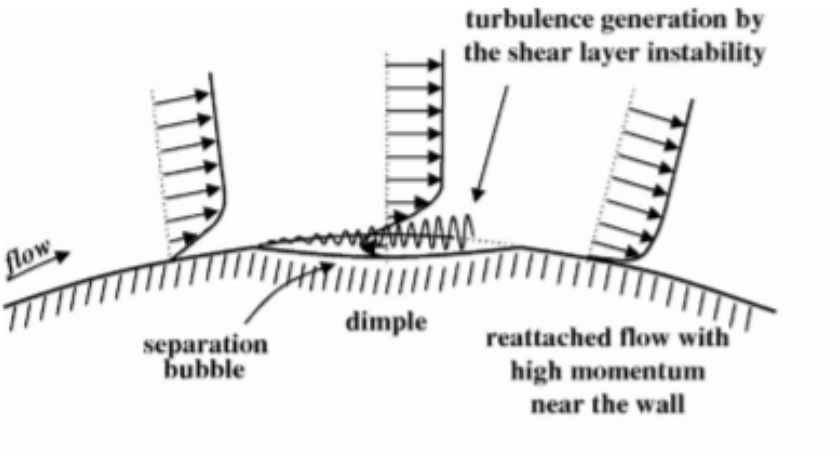

Figure 4.3: Schematic diagram of the dimple mechanism that promotes a shift in flow separation [39].

4.2 CFD Models

4.2.1 Turbulence Model

The accuracy of a solution using the Reynolds-averaged Navier–Stokes equations is dependent of the chosen turbulence model. However, many turbulence models are still

not able to sufficiently accurately solve the position of flow turnover from laminar to turbulence and the location of flow separation. Models applied to turbulent flow are classified into 3 categories:

- Reynolds stress model - solves every component of Reynolds tensor;
- Eddy viscosity model - substitutes the Reynolds stresses with a turbulence viscosity or an eddy viscosity;
- Eddy simulation models - solves complete unsteady Navier-Stokes equations;

The linear models have the characteristic of having two equations. These models can be divided into k-ϵ model, k-ω model and Shear Stress Transport (SST) model [43]. The k-ϵ model applies two equations for turbulent kinetic energy and turbulence dissipation. This model is suitable for inner flow field, not being recommended to solve flow separation by pressure gradients. In other hand, the k-ω gives accurate results for the near-wall region. This model applies the specific rate of turbulence energy dissipation ω, instead of the turbulence dissipation ϵ. The SST model combines the advantages of both k-ϵ and the k-ω models. This model delivers accurate results in entire flow by combining the advantage of the k-ω model at near-wall region and the advantage of the k-ϵ model in the rest of the flow field [43]. The two equations of the SST transition model are described as follows:

$$\frac{\partial}{\partial t}(\rho k) + \frac{\partial}{\partial x_i}(\rho k u_i) = \frac{\partial}{\partial x_j}\Big(\Gamma_k \frac{\partial k}{\partial x_j}\Big) + G_k - Y_k + S_k \tag{4.1}$$

$$\frac{\partial}{\partial t}(\rho \omega) + \frac{\partial}{\partial x_j}(\rho \omega u_j) = \frac{\partial}{\partial x_j}\Big(\Gamma_\omega \frac{\partial \omega}{\partial x_j}\Big) + G_\omega - Y_\omega + D_\omega + S_\omega \tag{4.2}$$

where G_ω and G_k represent the generation of turbulent kinetic energy and the specific dissipation rate; Γ_ω and Γ_k denote the flow diffusivity, Y_ω and Y_k correspond to dissipation, and S_ω and S_k to source terms.

From this model the SST-transition model is derived with the objective of modeling the transition of the boundary layer. This model aggregates two more equations to the set of equations of the SST model, these consider the intermittency γ and transition momentum thickness $R\bar{e}_{\theta t}$ to model the cross-flow of the region of separation, as:

$$\frac{\partial(\rho\gamma)}{\partial t} + \frac{\partial \rho U_j \gamma}{\partial x_j} = P_x\gamma 1 - E_{\gamma 1} + P_{\gamma 2} - E_{\gamma 2} + \frac{\partial}{\partial x_j}\Big[\Big(\mu + \frac{\mu_t}{\sigma_\gamma}\Big)\frac{\partial \gamma}{\partial x_j}\Big] \tag{4.3}$$

$$\frac{\partial(\rho R\bar{e}_{\theta t})}{\partial t} + \frac{\partial(\rho U_j R\bar{e}_{\theta t})}{\partial x_j} = P_{\theta t} + \frac{\partial}{\partial x_j}\Big[\sigma_{\theta t}(\mu + \mu_t)\frac{\partial R\bar{e}_{\theta t}}{\partial x_j}\Big] \tag{4.4}$$

The computational effort using the SST-transition model is acceptable and it delivers good results for phenomena such as a pressure-induced separation. Although, it is necessary to have a fine mesh of the near-wall for the model to achieve the convergence criteria and provide a detailed solution. The mesh refining is characterized by y+, where y+ is defined as the dimensionless wall distance which tells the location of the first node away from the wall. For the model used, an y+ less than 1 is recommended, which is the lowest category of values, representing a very highly detailed meshe [44].

4.2.2 Aeroacoustic Model

The first aeroacoustic noise propagation equation was developed by Lighthill and Curle [43]. This equation correlates the fluctuating stresses in a flow field to the acoustic density oscillation. This can be calculated with the conversion of the kinetic energy of fluctuating shear motion of the flow to the acoustic energy of longitudinal oscillating sound wave. One of the most used aeroacoustic noise algorithms currently implemented in Fluent 19.0 is the Broadband Noise Source (BNS) - Boundary Layer Noise Source model that contains mainly the Proudman's model for quadrupole sources and Curle's boundary layer model for dipole sources.

The boundary layer noise sources model is based on Curle's integral, where the radiated acoustic pressure was derived as a function of the fluctuating surface pressure of the rigid body surface. The surface acoustic power radiated from the blade surface can be computed by the model, which is mainly focused on the dipole source produced by pressure fluctuation on the blade, as:

$$P_A = \frac{1}{\rho_0 a_0} \int_0^{2\pi} \int_0^{\pi} \overline{p'^2} r^2 d\theta d\psi \tag{4.5}$$

where $\overline{p'^2}$ represents the sound intensity, ρ_0 denotes fluid density, a_0 the sound velocity, $r \equiv |\overrightarrow{x} - \overrightarrow{y}|$ and θ represents the angle between $|\overrightarrow{x} - \overrightarrow{y}|$ and the wall-normal vector $\overrightarrow{n}$.

Fluent 19.0 also enables to calculate the area-weighted average of a quantity using a surface integral. This integral is computed by summing the product of the field variable ϕ and the facet area A_i, where each facet i is associated with a cell in the domain, in a total of n cells. The area-weighted average is then computed by dividing the summation of the product by the total area of the surface A, as expressed in Equation 4.6.

$$\frac{1}{A} \int \phi dA = \frac{1}{A} \sum_{i=1}^{n} \phi_i |A_i| \tag{4.6}$$

Equation 4.6 was used to evaluate the area-weighted average of the Surface Acoustic Power Level, which represents the total acoustic power of the boundary layer noise on the entire surface of the fan, represented in dB levels. These equations were deduced on the information provided by ANSYS Fluent User's Guide [43].

4.3 Two-dimensional Boundary Layer Analysis

The objective of this section is to optimize through a parametric study the different geometries and dimensions of the dimple with the aim of controlling the flow separation and, as a consequence, decreasing the noise emitted. In order to carry out the flow analysis over the investigated fan model, three different isolated profiles were simulated with different parameters.

4.3.1 Geometries

The fan geometry provided by the manufacturer is shown in Figure 1, where it can be seen that the fan blade is defined by a set of airfoils with a variable geometry along the radius direction. As will be mentioned in the following section the study of flow separation and

the aerodynamic model chosen require a very detailed mesh near the surfaces of the blade. In order to obtain a detailed mesh and to guarantee the convergence of results, it was required to simplify the original fan by removing some of its surface features. Figure 4.4 shows a comparison of the fan before and after removing the rectangular protrusions. Software ANSYS Spaceclaim was used for this purpose.

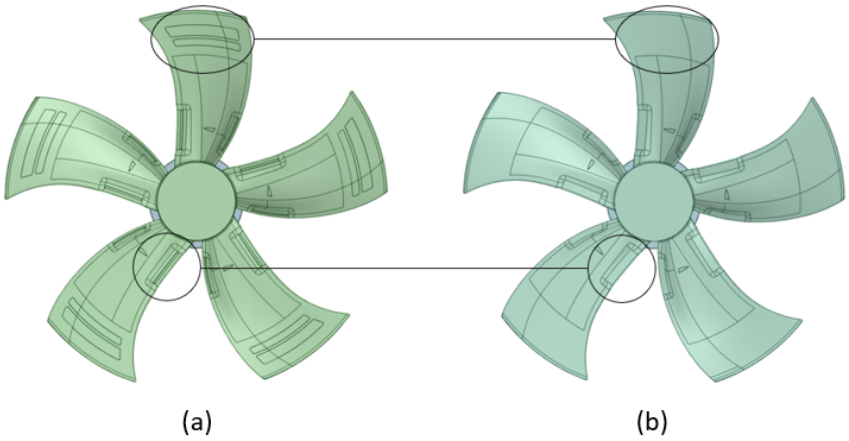

Figure 4.4: ⌀630 Ebm Papst fan: a) standard fan and b) simplified fan.

In order to evaluate the effect of the dimples on the two-dimensional flow separation, three sections of the blade were evaluated. The sections were carefully chosen in order to represent the three phenomena responsible for most of the noise generation in the axial fan due to their geometry, the vortex roll-up, the free-flow separation and the hub corner separation.

As mentioned in Chapter 3.3, a full three-dimensional can be represented by two-dimensional meridional flow. In order to define the two-dimensional flow it is necessary to create a meridional surface with a direction equal to the flow. Thus the meridional surfaces with $r = 135$ mm, $r = 210$ mm, $r = 290$ mm intersect the blades, as shown in Figure 4.5. Afterwards the meridional surface has to be unwrapped from the cylindrical coordinate systems to a cartesian one. The effect of this transformation can be observed in Figure 4.5 b).

To the angle of attack of the different airfoil was subtracted the averaged relative flow angle β_∞, this way the airfoil is parallel to the mean velocity vector of the flow α_∞, simplifying thus the CFD-Model. The Table shows the results for the average flow velocity and average flow angle for the main operating condition of the fan within the heat pump, 535 rotation speed (3150 m^3/h).

Table 4.1: Different parameters of the meridional flow method.

Radius section$[mm]$	Velocity $[RPM]$	Airflow $[m^3/h]$	u_∞ $[m/s]$	β_∞ [°]
290			4,12	12,2
210	535	3150	3,27	21,2
135			2,81	27,0

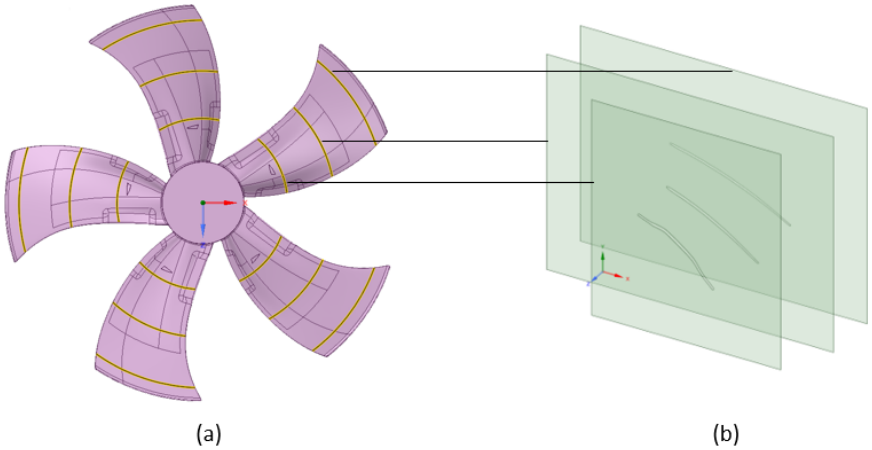

Figure 4.5: Result of the intersection of the circular meridional surfaces r=135 mm, r=210 mm, r=290 mm, with the fan blades, represented by yellow circular airfoils: a) blade sections in the meridional plane and b) meridional planes in the cartesian coordinate system.

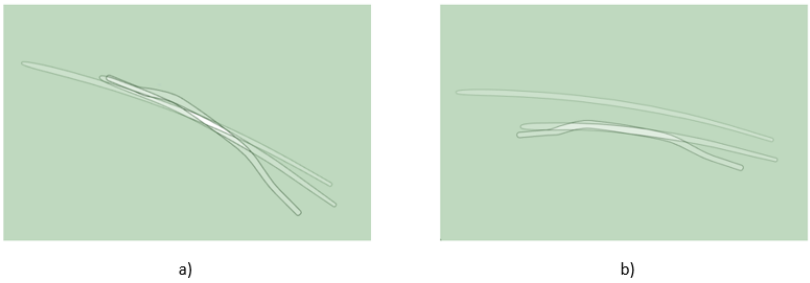

Figure 4.6: a)Original meridional plane in the Cartesian coordinates and b) Meridional plane with the change in the angle of attack of the different airfoils.

Since the flow is expected to be complex and three-dimensional within the cavity of the dimples, the study was performed in airfoils with 6 mm thickness (Figure 4.7), in order to predict the effect of the dimple on the flow properly.

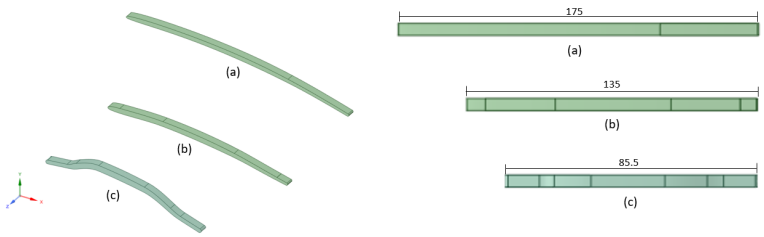

Figure 4.7: Geometries generated from the meridional planes: a) r=290 mm, b) r=210 mm, c) r=135 mm and respectively chord length.

4.3.2 Dimple Location

The study by Bearman et al. [41] showed that with only one dimple it is possible to observe a shift in flow separation. The objective of this section is to find the correct position to place the dimples in an airfoil and the different parameters that affect this choice. The majority of the literature on the use of dimples in airfoils mentions the location between 60-80% of the chord length. This region is associated to the separation of the flow. The study by Casey [42] obtained excellent results in the control of the turbine blade boundary layer separation through the numerical simulation of the meridional plane method for an airfoil with a dimple at 65% of the chord length . This distance was considered as the initial parameter of the optimization of the location of the dimple (Figure 4.8). The geometry of the dimple analyzed in the previous work by Santos [12] was considered as an the initial geometry for this study.

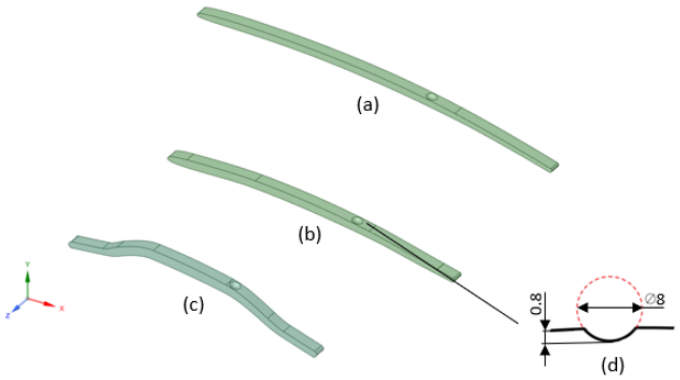

Figure 4.8: Single dimple application at: 65% of the airfoil chord length a) r=290 mm, b)r=210 mm and c)r=135 mm.

4.3.3 CFD Domain and Mesh

In the selection of the domain for the analyzed airfoils, the distance of the domain was kept large enough to ensure that the boundary conditions did not influence the interaction of the flow with the airfoil. The domain has the same thickness as the airfoil to avoid the influence from the margins of the side walls on the main flow.

In order to build a qualitative mesh able to solve accurately the flow around the profile, and especially the delicate problem of the flow in the near-wall regions, it is necessary to use of inflation layers to ensure that the mean normalized wall distance $y+$ is smaller than 1. The ANSYS guide [43] recommends the use of 25 inflation layers with the first layer of 0.025 mm in height with a growth of 1.2%. The mesh used has tetrahedral elements, to these elements were added the normal angle curvature of 9º so that the elements fit the curvatures of the airfoil. The mesh is more detailed next to the leading edge, trailing edge and dimple where important phenomena is expected to occur. To guarantee a valid mesh, the analysis parameters were the orthogonal quality which evaluates the coupling between the elements and the skewness which evaluates how much the element is distorted. Orthogonal quality values above 0.1 and skewness values below 0.15 are the target parameters for an ideal mesh [43]. The statistics of each

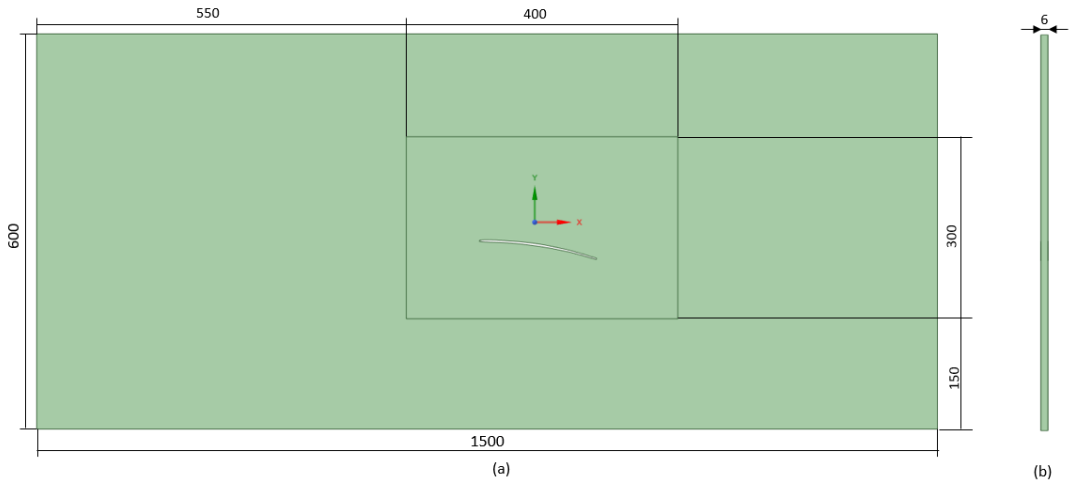

Figure 4.9: CFD-Model geometry: a)frontal view and b)lateral view.

model's mesh elements alternates between 3 and 3,5 million elements. The mesh was generated and evaluated through ANSYS meshing.

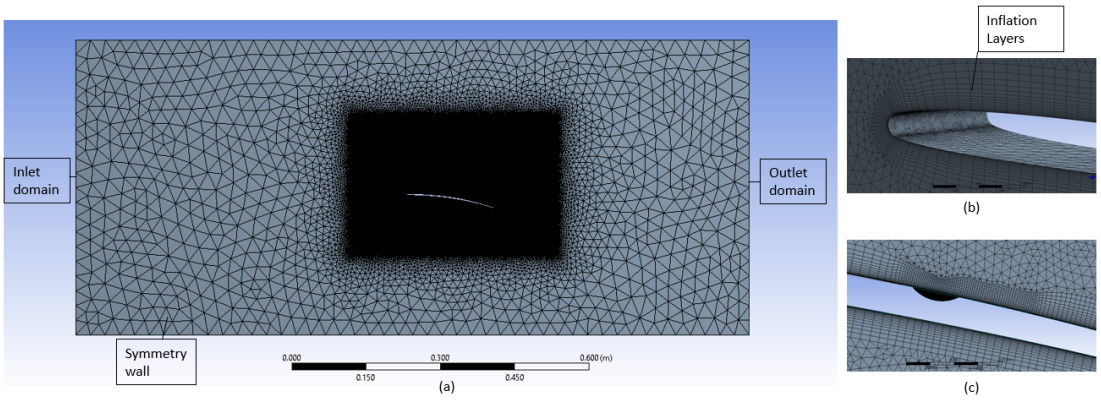

Figure 4.10: CFD-model mesh: a) front view of the mesh and associated boundary conditions, b) mesh refinement leading edge and inflation layers and c) mesh refinement near the dimple location.

4.3.4 Results

An analysis of the flow separation was carried out for the three airfoils with and without dimples. The flow behaviour of these models was evaluated by analysing a centered section view, as presented for the r=290 mm airfoil in the Figure 4.11. The Figure 4.11 shows the velocity field of the r=290 mm standard airfoil. At the leading edge, the vector field shows a region of separation with reattachment this phenomenon represents the leading edge vortex generation, commonly seen in airfoils with medium to high angle of attack [45]. Then the flow kept attached until it reached the point of separation at 63,4% of the chord length, followed by a reverse flow region. The results for the

Table 4.2: Surface Acoustic Power Level (SWL) and point of separation location for the different airfoil models.

Fan section radius[mm]	Model	Area Avg. SWL [dB]	Point of flow separation [% of the chord length]
290	Standard Airfoil	16,5	63,4
	Dimpled Airfoil	16,5	71,5
210	Standard Airfoil	18,0	77,6
	Dimpled Airfoil	18,0	77,6
135	Standard Airfoil	31,5	68,8
	Dimpled Airfoil	31,2	70,4

different airfoil are shown in Figure 4.12 and Figure 4.14 and resumed in Table 4.2, where boundary layer separation point and the surface acoustic power were analyzed.

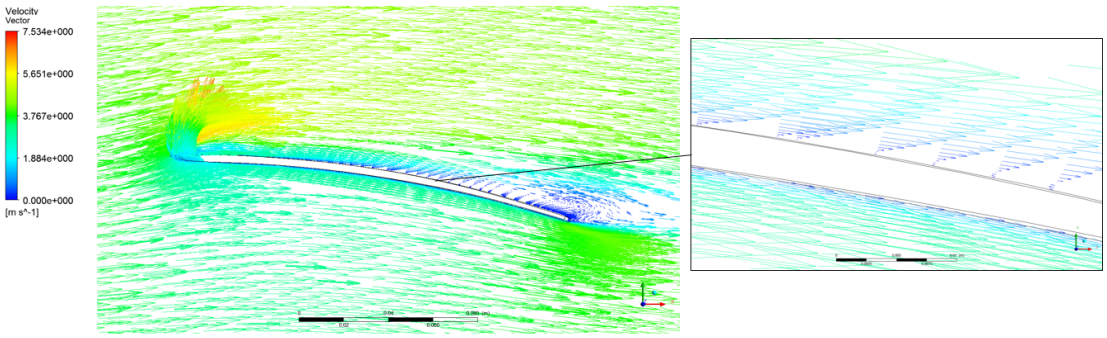

Figure 4.11: Velocity streamlines of the free-flow velocity in the CFD-Domain: a) frontal view and b) beginning of reverse flow near the surface.

An Isosurface is a good tool to illustrate the occurrence of the flow separation where its theory has been presented in Chapter 3.2. With the physical variable of zero velocity, an Isosurface can be generated. But this zero velocity would also include the flow at the wall. Hence, an Isosurface near 0 m/s which is $0.7m/s$ can be applied to observe the separation zone. In the analytical design, the separation zone for the different airfoil with and without dimples is represented by the turquoise color Isosurface in Figure 4.12.

From the Image 4.12 and the Table 4.2 it is possible to observe a shift of 8.1%, 1.6% and 0% in the separation of the flow in the dimpled airfoils r= 290, r=135, r=210, respectively. This result suggests that the closer the dimple is to the point of flow separation, the more effective it is.

The Figure 4.13 shows in detail the velocity vector in the separation zone. The sub-figure on the left shows the flow to separate generating a reverse flow, while in the dimpled airfoil is generated a small vortex in the cavity represented in the figure by the vectors with opposite direction to the flow. Above this, a higher density of vectors with direction of flow creates a small re-circulation inside the dimple, mixing the flow near the surface with low velocity with the free flow with high velocity (note the distribution of the velocity vector above the dimple). The vortex generated though the recirculation energizes the velocity vector, by increasing it near the surface of the

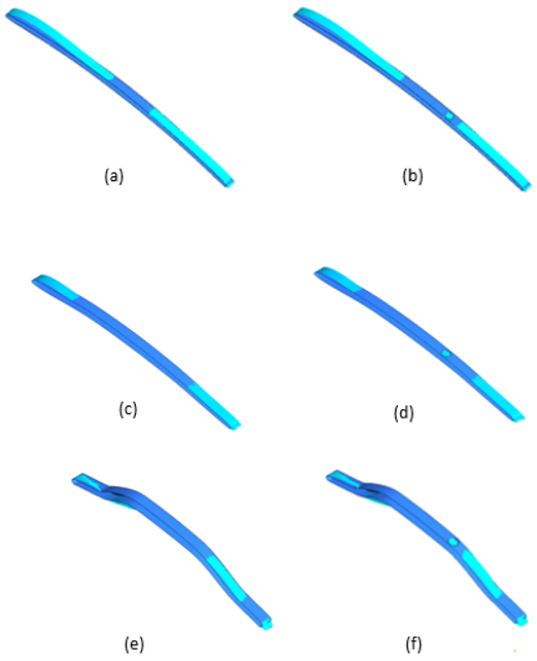

Figure 4.12: Isosurface with 0.7 m/s generated for the airfoil: a)standard airfoil r=290 mm, b)dimpled airfoil r=290 mm, c)standard airfoil r=210 mm, d)dimpled airfoil r=210 mm, e)standard airfoil r=135 mm and f)dimpled airfoil r=135 mm.

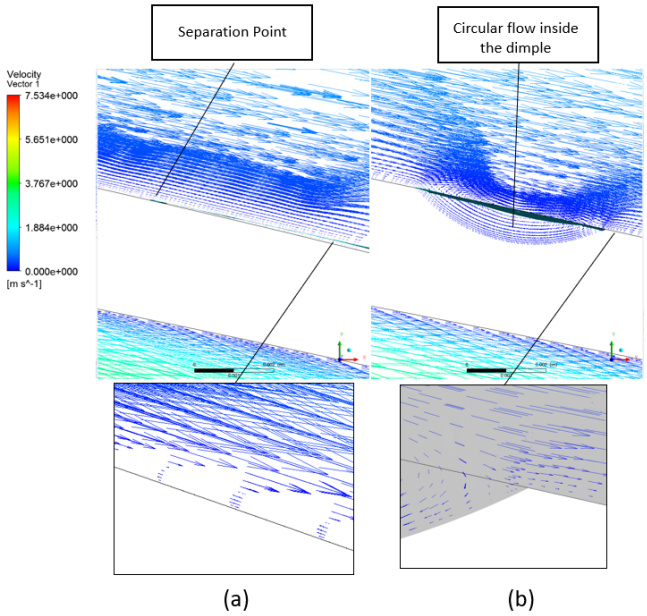

Figure 4.13: Velocity vector for the model: a) standard r=290 mm airfoil and b) dimpled r=290 mm airfoil.

airfoil, so the accelerated velocity profile can overcome the adverse high pressure and wall friction remaining attached to the airfoil. The necessity for the dimple to be close to the separation point supports this theory. The small vortex has to be able to energize the flow when the velocity vector is decelerated due to its low kinetic energy.

Although the dimpled airfoil with r=290 mm presents the maximum shift in boundary layer separation, the analysis of the boundary layer noise does not show noise improvements (Figure 4.14), whereas the dimpled airfoil with r=135 mm model with only a shift of 1.6%, presents a reduction of 0.3 dB, which suggests that the biggest reduction of the fan noise will be in that region. In spite of this, the aim of this section is the optimization of the pattern that shifts more the flow separation so the focus of the two-dimensional analysis will turn to the airfoil with r=290 mm.

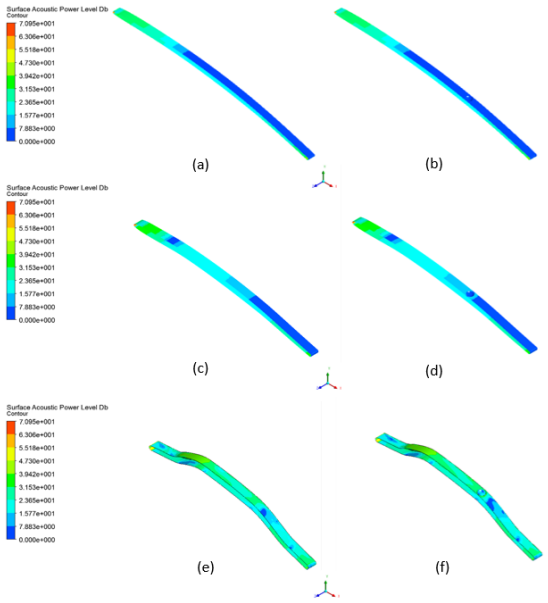

Figure 4.14: Surface acoustic power for the: a) standard airfoil r=290 mm, b) dimpled airfoil r=290 mm, c) standard airfoil r=210 mm, d) dimpled airfoil r=210 mm, e) standard airfoil r=135 mm and f) dimpled airfoil r=135 mm.

4.3.5 Dimples Depth

In order to analyze the influence of the depth of the dimple an analysis of the airfoil r=290 mm, that showed the best results in the shift of the flow separation, was made with different depths of the dimple, as shown in the Figure 4.15. The results are presented in Table 4.3.

Table 4.3: Effect of the dimples depth on the flow separation point.

Fan section radius $[mm]$	Dimple depth $[mm]$	Point of flow separation [% of the chord length]
290	0,2	69,3
	0,6	70,4
	0,8	71,5

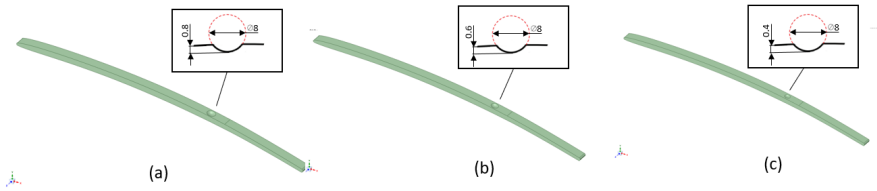

Figure 4.15: Different dimple depth: a)0.8mm, b)0.6mm and c)0.4mm applied to the airfoil r=290 mm at 65% of the chord length.

The results from the Table 4.3 suggest that with the increase of the dimple depth of a bigger vortex is generated due to more recirculation inside the dimple. This effect will accelerate more the flow right after the dimple, improving the flow attachment to the blade. A bigger depth was not studied in order to guarantee that depth does not exceed half the thickness of the blade.

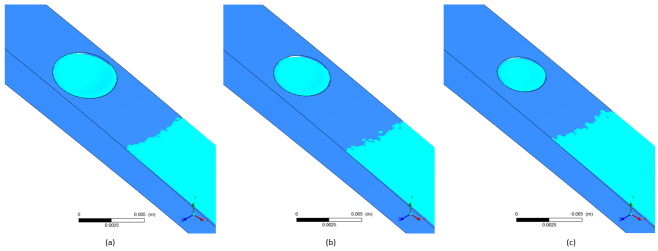

Figure 4.16: Isosurfaces generated for the different models with dimple depth: a)0.8mm, b)0.6mm and c)0.4mm.

4.3.6 Circular vs Hexagonal Dimple

The study documented along this section aims to identify effects of dimple geometry. Two r=290 mm airfoils were evaluated: the solution optimized up to this point, and another airfoil with the same parameters where the circular cavity is replaced by a hexagonal one, as can be observed in the Figure 4.18.

Figure 4.17: Effect of the dimple geometry on the point of flow separation.

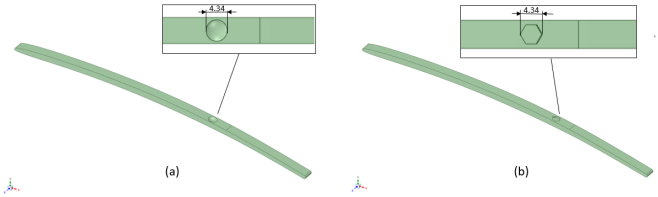

Figure 4.18: Geometry of the airfoil with an: a) circular dimple with ⌀4,34mm and b) hexagonal dimple with ⌀4,34mm.

In the first analysis between the different patterns, Figure 4.19 shows a profile of flow velocities above the cavity. In the case of the hexagonal pattern the generation of

Table 4.4: Point of flow separation for different dimple geometries.

Fan section radius $[mm]$	Airfoil Model	Point of flow separation [% of the chord length]
290	Standard	63.4
	Hexagonal	70.9
	Circular	71.5

the reverse flow exists inside and slightly outside the cavity (Figure 4.19), which leads to the vortex being dissipated away from the surface of the airfoil (vector field less dense above the cavity), it will accelerate the vector field after the dimple surface, but in a less efficient way. This can be seen in Figure 4.19 e) and f) where the vector field after dimple hexagonal has a lower magnitude when compared to the circular dimple .

The Figure 4.19 c) and d) shows three dimensional streamlines that are a very useful tool to represent the complex flow generated inside the dimple. It is observed that the creation of the vortex is identical in both dimple geometries, where the flow is pulled to the center of the dimple before leaving it. This suggests a tendency for the flow to separate earlier at the edges of the airfoil than at the center.

The analysis of the skin friction of each of the dimple shows that in the hexagonal lateral walls do not contribute to the increase of the skin friction. This is due to the fact that these walls do not contribute to the surface shear stress because the velocity vector in these walls is perpendicular to the flow. Even so, the circular dimple presents a smaller contribution to the increase of drag due to the velocity profile being distributed over its surface, where only the deepest zone has parallel flow to the main flow resulting in a slightly increase of the wall shear stress in this region.

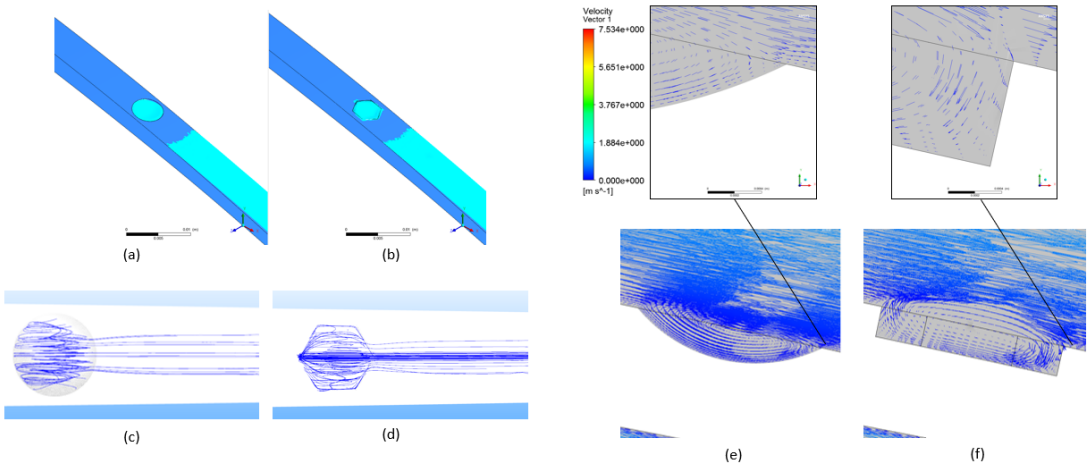

Figure 4.19: Effect of the: a) Isosurface with 0.7ms in the circular dimple, b)Isosurface with 0.7ms in the hexagonal dimple, c) 3D pathlines affected by the circular dimples, d) 3D pathlines affected by the hexagonal dimples, e) velocity vector of the circular dimple and f) velocity vector of the hexagonal dimple.

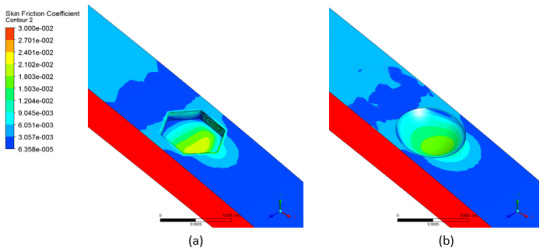

Figure 4.20: Skin friction coefficient for the surface of the: a)hexagonal dimpled airfoil and b)circular dimpled airfoil.

4.3.7 Number of Dimples

In an attempt to re-energize the flow several times in order to further shift the flow separation, more dimples were added 1 mm apart to the airfoil with the same parameters as the previously optimized solution.

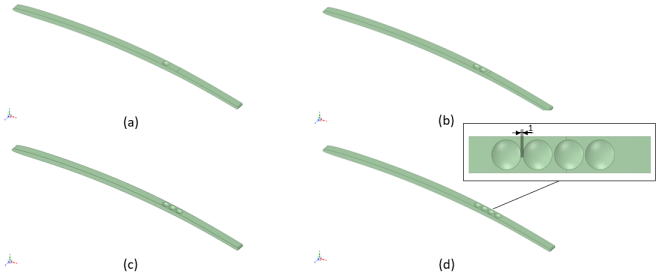

Figure 4.21: Geometry of the airfoil r=290mm with: a) one dimples, b) two dimples, c) 3 dimples and d) 4 dimples with 1 mm between each other.

Table 4.5: Point of separation evaluation with an increase on the number of dimples applied to the airfoil.

Fan section radius $[mm]$	Number of dimples	Point of flow separation [% of the chord length]
290	1	71,5
	2	73,8
	3	78,5
	4	76,9

The results of the Table 4.5 and Figure 4.22 show the influence of an increase on the number of dimples downstream the original point of separation. The results of an increase of dimples show that they have the ability to energize the flow several times until the velocity vector acceleration provided by the vortex generated inside the cavity is not sufficient to penetrate the high pressure gradient zone. The airfoil with three dimples, with the first one placed on the point of separation, shows an improvement of 7% in relation to the previously optimized solution, reaching a flow separation shift of 15.1% in comparison with the original airfoil. The pattern with two and four dimples shows the flow to separate first near the edges of the airfoil according to the theory

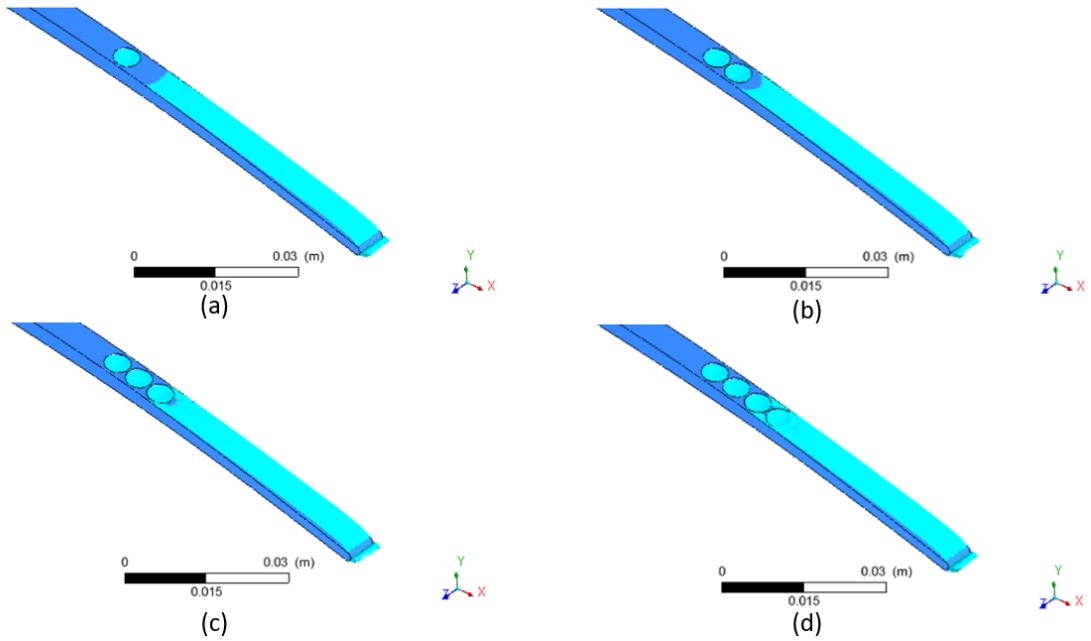

Figure 4.22: Isosurface with 0.7m/s for the r=290 mm airfoil with: a) one dimple, b) two dimples, c) three dimples and d) four dimples.

presented in Section 4.3.6.

4.3.8 Dimples Pattern

This section aims to evaluate the influence of distance between the dimples and other types of patterns in order to avoid separation on airfoil edges. The different patterns are shown in Figure 4.23.

Table 4.6: Effect of the different patterns on the point of flow separation.

Fan section radius [mm]	Pattern	Point of flow separation [% of the chord length]
290	a)	78,5
	b)	76,8
	c)	78,5
	d)	70,7

The analysis shows that with the increase of the distance between the dimples, the flow may not be accelerated when it presents low kinetic energy. Furthermore, the fluid tends to separate at the edges of the section. This is represented in the Figure 4.24 with signs of the isosurface between the second and third dimple near the lateral edge of pattern b).

It is possible to observe the effect of dimple on b) and c) patterns, where despite the flow is already separated from the surface the acceleration of the flow immediately after dimple exit is sufficient for the reattachment of the flow being separated shortly after. Thus, the pattern a) continues to be the most optimized solution.

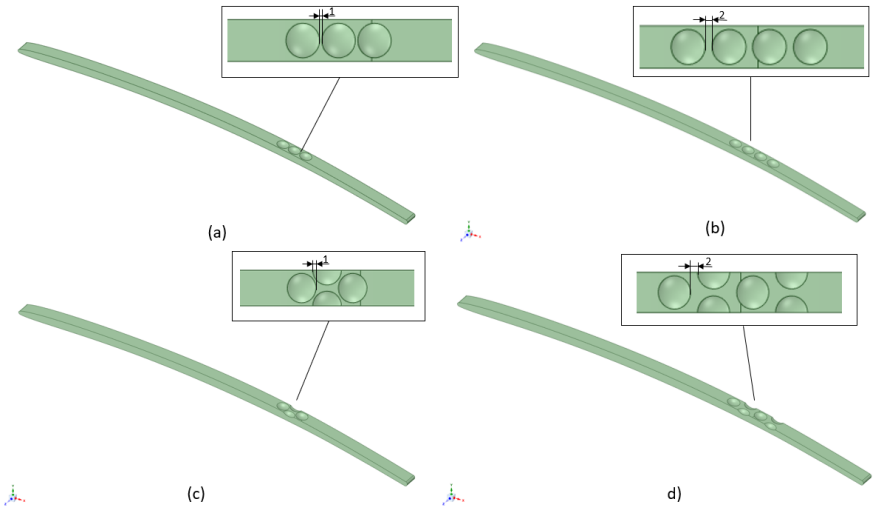

Figure 4.23: Dimples configuration applied to the airfoil r=290 mm, a)three dimples spaced by 1mm b)four dimples spaced by 2mm, c)pattern with 2 dimples between the first and last dimples with 1mm of spacing and d) pattern with 2 dimples between the first and last dimples with 2mm of spacing.

In the analysis of patterns a) and c) the displacement of dimples near the edges of the airfoil is shown to be beneficial, since the separation line is evenly distributed.

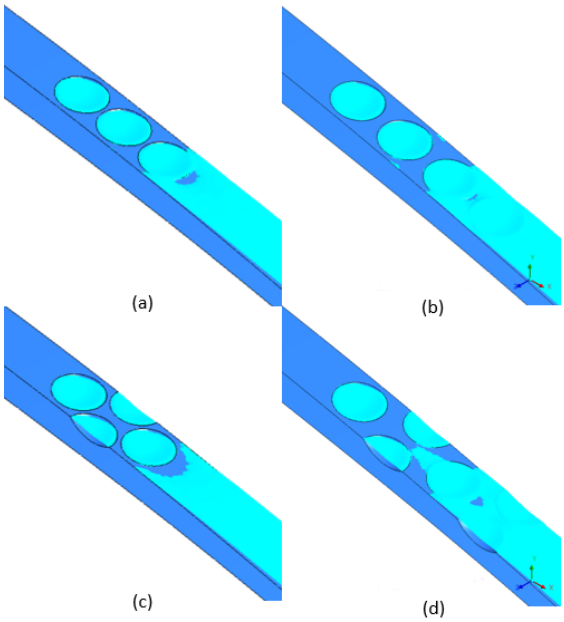

Figure 4.24: Isosurface with 0.7 m/s for the r=290mm airfoil with: a) 1mm of spacing between dimples pattern, b) 2mm of spacing between dimples pattern, c) pattern with 2 dimples between the first and last dimples with 1mm of spacing and d) pattern with 2 dimples between the first and last dimples with 2mm of spacing.

4.4 Three-Dimensional Flow Separation

When the fan is rotating, the moving direction and velocity of air flow in fan surface were constantly changing, resulting in a complex three-dimensional flow.

The present section aims to adapt the optimized dimple pattern from the two-dimensional flow study to the original ⌀630 mm fan and evaluate the noise reduction and efficiency of the different dimpled fans.

As a first step, the different aeroacoustic phenomena resulting from the three dimensional separation of the flow in the original fan were identified. Followed by the validation of the model by comparison with the fan curve provided by the manufacturer.

Then the optimized pattern of circular and hexagonal dimples studied in section 3.2.1 was applied in the standard fan, with some adjustments considering the circular direction of the flow. In a final stage the fan curve, efficiency curve and noise curve of the dimpled fan models and the standard fan were compared and analyzed.

4.4.1 Simulation Domain and Mesh

Due to the high complexity of the fan blade, there is a compromise between ensuring a fine mesh and keeping the number of elements below the limit of 10 million in order to guarantee the post processing of the simulation.

As mentioned in the Section 4.2.1, the tubulence model requires a y+ less than 1 in order to converge, so the inflation layers were used with the same parameters of Section 4.3.3. The mesh was generated with ANSYS Meshing, where the proximity and curvature function was used in order to give flexibility to the elements, increasing the mesh detail next to the complex geometries and geometries that have more effect on the flow. The angle of curvature was kept at 9º in order to capture the twisted surfaces of the blade. This value is recommended for turbomachines by ANSYS turbomachinery guide [44].

The mesh generated for the entire fan had a statistic of 33 million elements, even with access to Bosch High Performance Computer (HPC), there were pre-processing problems due to the high number of elements. In order to solve this problem, periodic boundary conditions were used (Figure 4.25) since it is expected a periodically repeating nature of the solution flow. This technique reduced the number of elements to approximately 7 million. Experimental studies [46, 47] compared with simulations show that the use of periodic boundary conditions can accurately predict the flow and broadband noise generated by an axial fan.

Unfortunately, the simulation was not possible with the complete geometry of the heat pump, since it would increase in large scale the number of elements used. The biggest influence of the chosen domain in the simulation would be the evaporator that was simplified through a half-cylinder with its center align with the axis of rotation (Figure 4.25). The shroud is expected to influence the acoustic results, so the original geometry was considered.

4.4.2 Results

Using CFD-Post, the streamline velocity profiles were plotted for the original fans, to better understand the generation of flow separation in the rotating flow.

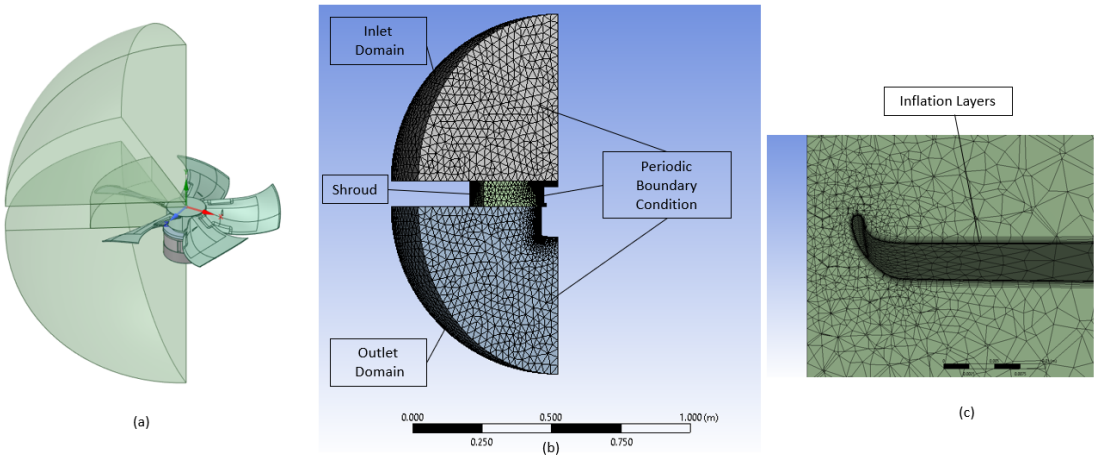

Figure 4.25: CFD-Model details: a) CFD-Model geometry with boundary conditions, b) Mesh and boundary condition used, c) Mesh refinement to capture the flow separation (y+ less than 1).

Through the streamlines it is possible to identify the reverse tip leakage flow in the blade tip clearance. This is due to the difference in pressures between the suction surface and pressure, leading to the separation of the flow that ends up rolling over the winglet (Figure 4.26 b)), generating turbulence in the blade suction side.

It is also possible to visualize the hub corner separation in junction between the blade and the hub. The flow separation developed on the blade fan interacts with the flow separation from the hub increasing of the overall thickness of the flow separation, generating a well-developed vortex (Figure 4.26 c)).

It is also shown the effect of reverse leakage after the motor, generating turbulence in the outlet of the simulation domain.

It is necessary to identify the region of flow separation in the blade surface in order to proceed with the application of the optimized dimple pattern studied in the Chapter 4.3. In order to identify the location of the flow separation in a complex three-dimensional flow, the skin friction pathlines were plotted in which their theory was explained in Chapter 3.2.2.

In the analysis of the Figure 4.27 it is possible to observe, at the leading edge of the blade, a separation dividing line followed by an attachment dividing line from the hub to the tip emerging with the dividing line of separation near the tip. This represents the leading edge vortex developed at the leading edge of the blade and transported out toward the blade tip, caused by the adverse pressure gradient and the geometric curvature of the blade leading edge [45].

Next to the tip is shown a separation dividing line, which corresponds to the separation of the flow creating a vortex that will roll-up over the winglet followed by the attachment on the pressure surface of the blade, representing the reverse tip leakage already shown in the Figure 4.26.

At about 41% of the chord length near the hub, it is possible to notice a diving line of separation with radial direction up to 36% of the trailing edge. This line represents the separation of the free flow. The separation on the blade and the separation on hub generates two focus of separation, which illustrates the formation of the hub corner

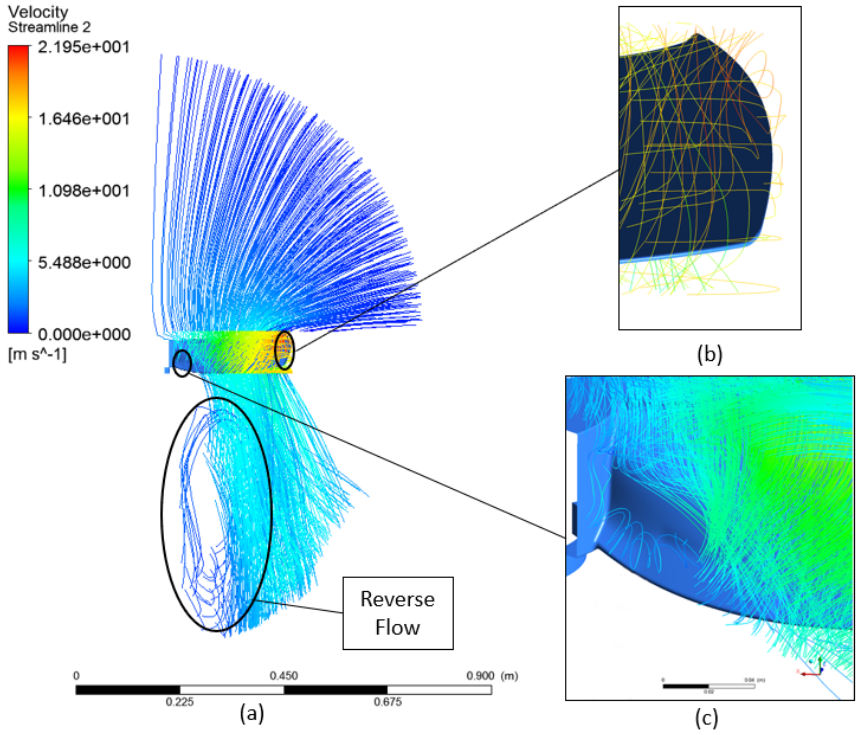

Figure 4.26: Velocity streamlines at 535 rotation speed 3000 m^3/h: a) entire CFD-model, b) vortex roll-up near the tip and c) hub corner separation and vortex generated.

vortex also shown in Figure 4.26.

It should be noted that the skin friction lines, illustrated in Figure 4.27, are shown for the simulation at 535 rotation speed (1000 m^3/h) which is an expected condition close to the aerodynamic stall, for a better perception of the dividing lines. When comparing the Figure 4.26, that represents the streamlines at the operating point 535 rotation speed (3000 m^3/h), with the Figure 4.27, the separation occurs closer to the trailing edge, which shows that the separation line moves towards the leading edge with the decrease of the airflow. This follows the literature since at low airflows is expected the occurrence of stall, represented by complete separation near the hub, as illustrated in Figure 3.20.

4.4.3 Dimpled Fans Geometries

With the separation location of the boundary layer already defined it was possible to apply the optimized pattern in the standard ⌀630 mm fan. The optimized pattern is composed of 3 circular dimples 1mm apart, with 4.34 mm of diameter and 0.8 mm of depth. Besides this pattern, another pattern with the same parameters was applied to another fan. The only change was the geometry of the dimples, being the second model with hexagonal dimples. The aim of this model is to evaluate as a final study the influence of a bigger dimple per area ratio at critical operating point (near stall).

The application of circular and hexagonal dimples on the blade presented some challenges due to their design. Previously the dimples had been applied to an airfoil being aligned with the direction of flow. In this case the flow is quite complex, but largely

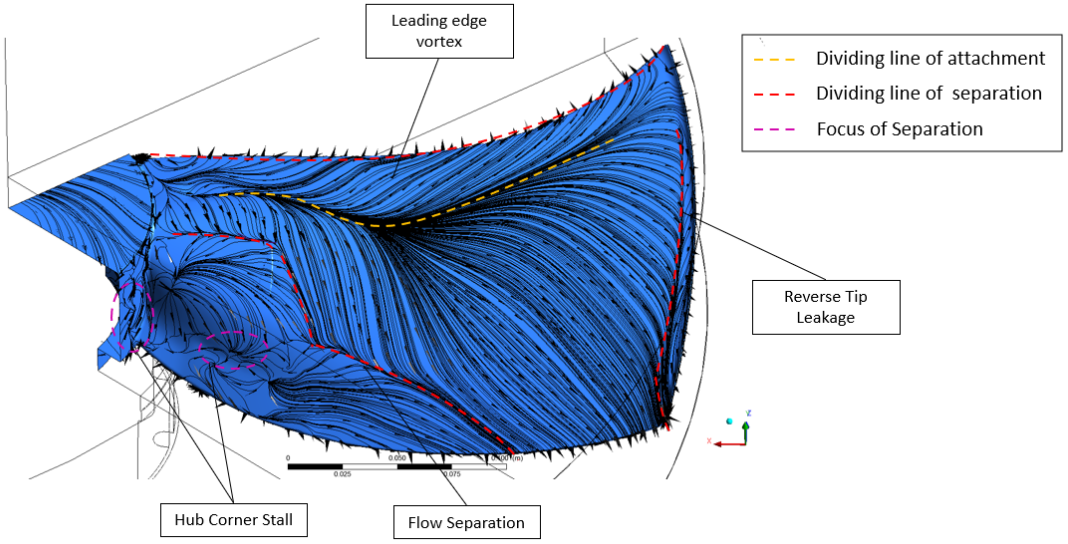

Figure 4.27: Skin-friction lines on the original fan blade suction surface at 535 revolution per minute (1000 m^3/h).

follows a circular trajectory. Thus, the circular dimples were applied with this trajectory, unfortunately this cannot be applied to the hexagonal dimples. The different designs are shown in the Figure 4.28.

The first dimple of the optimized pattern was placed over the 535 rotation speed (1000 m^3/h) separation line represented in the Figure 4.27, in order to guarantee the most important condition found in Chapter 3.2.1, the flow acceleration in the line of separation. Since the separation line tends to move closer to the trailing edge with the increase of the airflow, one to two dimples were added to the optimized pattern in order to make the geometry suitable for a higher airflow. Further information on the dimpled fan design can be observed in the Figure 4.29.

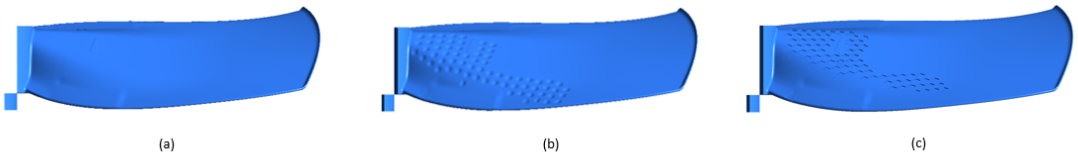

Figure 4.28: Dimples design on the ⌀630 fan blade: a) original blade, b) blade with circular dimples along the separation line nad c) blade with hexagonal dimples along the separation line.

4.4.4 Results

In this section the results of the airflow variation at 535 rotation speed are compared with the manufacturer's data sheet. Subsequently, the aeroacoustic behavior and the efficiency of the model with dimples are compared with the standard model. Due to time limitations the hexagonal pattern will be evaluated only for critical operating points.

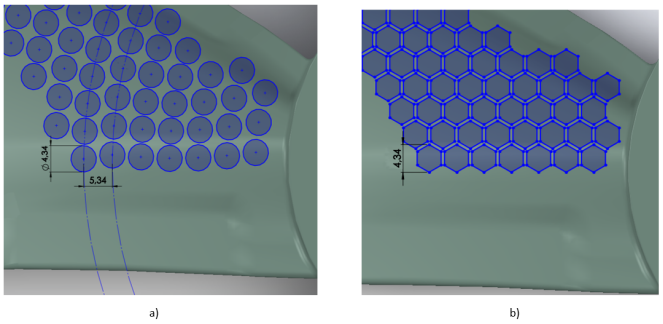

Figure 4.29: Zoom in on the dimples designed on the ⌀630 fan blade and its dimensions.

The variation of the airflow was made through the changing of the mass-inlet-flow in the boundary conditions of the CFD model. The results obtained for the variation of the airflow at 535 rotation speed are presented in Table 4.7 and subsequently compared with the curve provided by the manufacturer, in Figure 4.31.

Table 4.7: Operating points and surface Acoustic Power Level (SWL) of the standard and the dimpled (circular) fan models at 535 rotation speed.

Fan Model	Velocity $[RPM]$	Airflow $[m^3/h]$	Pressure Drop $[Pa]$	Area Avg.SWL $[dB]$	Fan Efficiency [%]
Standard Fan	535	500	46,3	53,2	8,9
		800	45,8	51,1	13,1
		1000	47,4	50,6	15,8
		1500	44,3	51,2	18,7
		2000	38,1	50,3	23,3
		2500	35,8	49,9	28,1
		3000	33,5	48,8	31,9
		3500	31,3	47,9	35,1
		4000	28,7	47,5	36,2
		4500	25,3	47,4	37,9
Dimpled fan	535	500	47,2	52,5	11,2
		800	48,7	48,2	15,0
		1000	48,2	48,5	17,3
		1500	44,5	51,3	19,1
		2000	38,1	49,9	24,5
		2500	35,7	49,2	28,8
		3000	33,6	48,0	32,5
		3500	31,0	47,5	33,7
		4000	27,2	47,0	34,9
		4500	23,2	46,6	35,1

Model Validation

The simulated models show to operate at normal airflow rates with similar pressure drop to the ones predicted by the manufacturer. There is a big difference between the curves for airflows higher than 3500 m^3/h, which can be correlated to the fact that the manufacturers carry out the experimental studies without any type of shroud around the fan. The experimental studies [48] supports this theory, by showing that a fan without shroud has a lower pressure coefficient associated in comparison with a ducted fan, especially for higher airflow rates.

Since the flow separation is a phenomenon which increases at lower airflow rates and near-stall or complete stall conditions, which correspond to operating points often not covered by the manufacturer's fan curves, the fan curve was extended to lower airflow values.

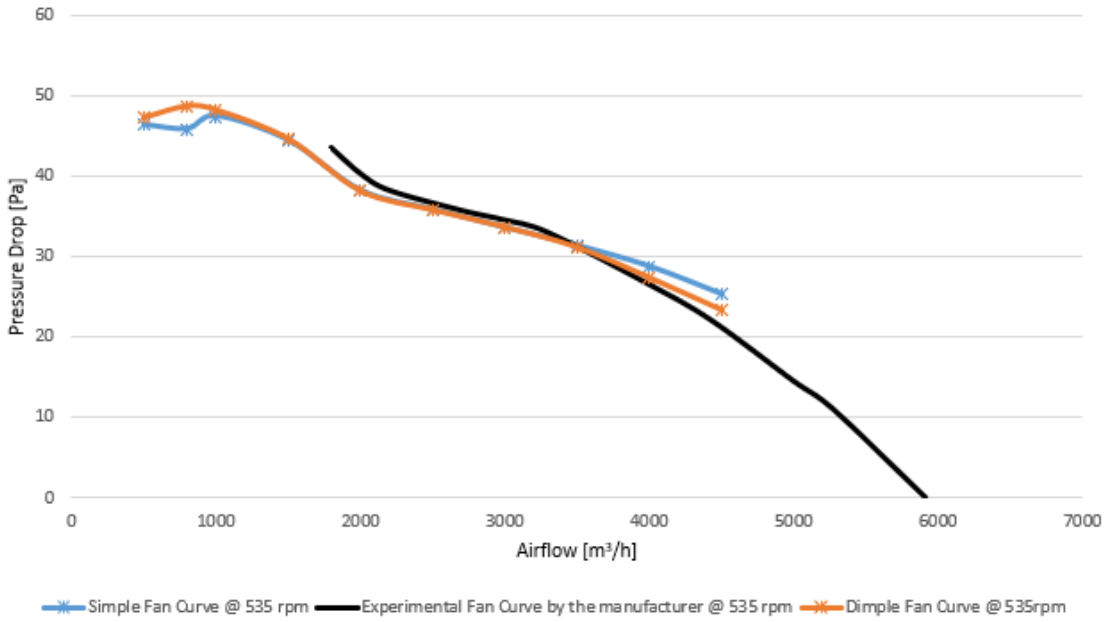

Figure 4.30: Evolution of the operating points standard and dimpled(circular) fans models at 535 rotation speed, for different airflow rates and comparison with the experimental curves based on the fan's data-sheet.

Fan Noise

The comparison between the curves of the dimpled model and the standard model shows that they fairly similar pressure drop associated after the 1000 m^3/h operating point. At 1000 m^3/h there is a point of inflection of the standard fan curve and it is referenced for the appearance of aerodynamic stall by the literature. In the model with dimples this inflection point only appears at 800 m^3/h, which suggest flow separation control for the dimpled model resulting in a shift of stall to a lower airflow. A detailed study of this phenomenon will be described in the next section.

Analyzing the fan noise curves, it is possible to see how boundary layer noise of the dimpled model is lower than the standard fan for airflows above 1500 m^3/h. The Figure

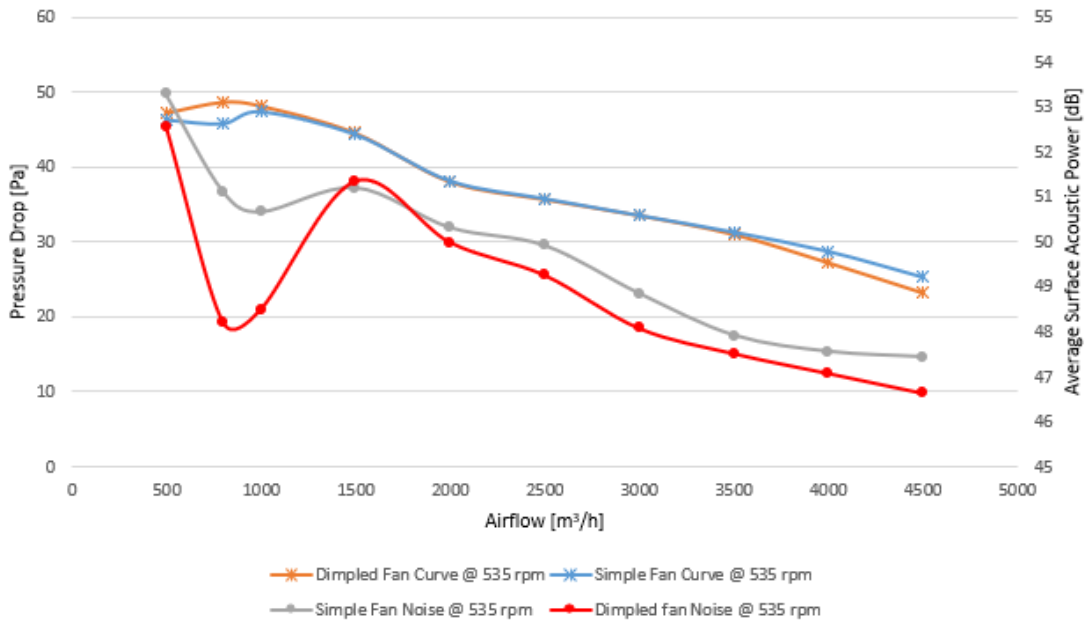

Figure 4.31: Evolution of the operating points and boundary layer noise of the standard and dimpled fans models at 535 rotation speed, for different airflow rates.

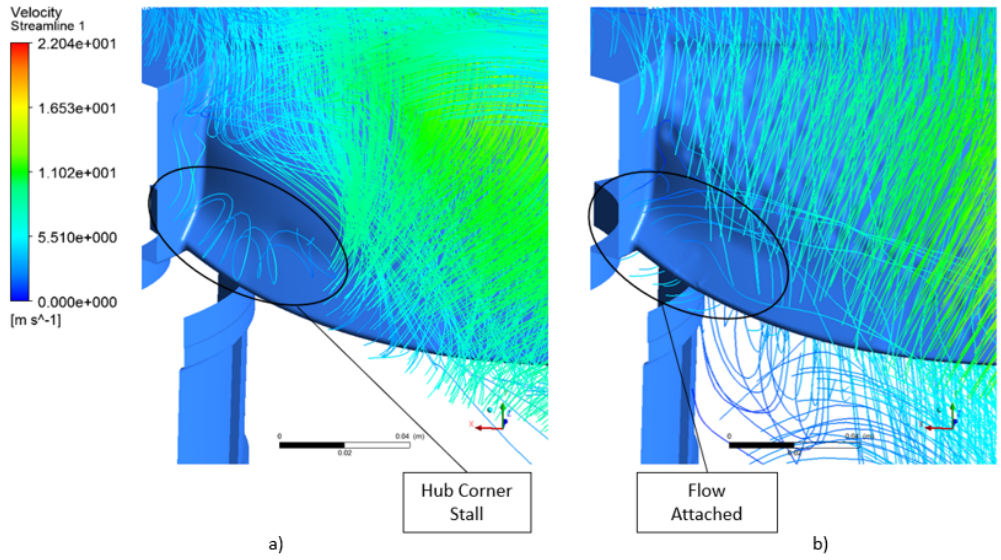

Figure 4.32: Velocity streamlines at 535 rotation speed 3000 m^3/h for the a) standard fan and b) dimpled(circular) fan.

4.32 clarifies this reduction showing the velocity streamlines for 3000 m^3/h, in the fan with dimples it is possible to observe the shift of the boundary layer separation of the main flow. This way, the turbulence generated does not have enough momentum to merge with the turbulence generated in the hub avoiding the increase of its thickness and the generation of the hub corner vortex, resulting in a reduction of 0.8 dB.

For values below 1500 m^3/h the curve presents a dip followed by an increase of the average boundary layer noise. In order to clarify this phenomenon, the following section is focused on this study.

Fan Efficiency

In Figure 4.33, the evolution of the operating points and the efficiency of the fan are compared for the standard model and the dimpled model.

The results show a higher efficiency for the model with dimples for airflow values below 3000 m^3/h. There is a more significant increase for values below 1500 m^3/h of airflow to these is associated greater separation up to the point of stall. This supports the theory that the dimples shift the occurrence of stall, which affects the efficiency of the fan.

For higher airflows 3000 m^3/h the model with dimples presents a lower efficiency, and this result was expected. The introduction of dimples increases the skin friction as seen in Chapter 4.3.6, by increasing the overall drag of the fan, which has more influence at higher airflow rates.

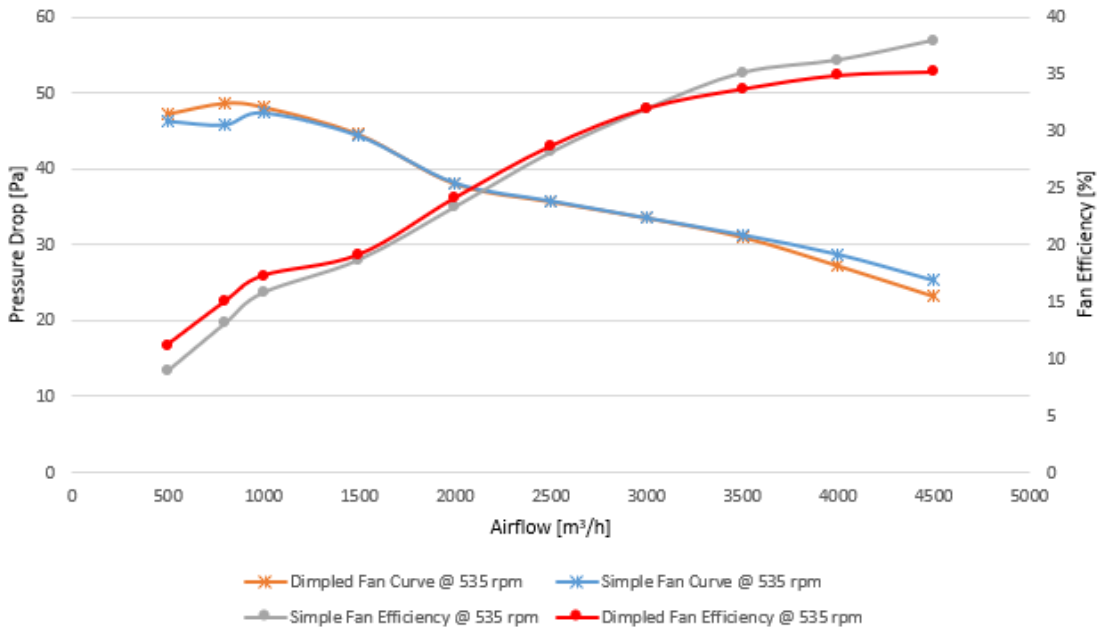

Figure 4.33: Evolution of the operating points and the fan efficiency of the standard and dimpled(circular) fan model at 535 rotation speed, for different airflow rates.

Stall Study

In order to clarify the suggested stall shift in the dimpled model the Isosurfaces are shown for the different model in Figure 4.34 for the 535 rotation speed (800 m^3/h) operating point. At this point of operation the curve suggests that the standard fan is in aerodynamic stall, and it is also expected that a larger number of dimples per area will be beneficial. Therefore, the model with hexagonal dimples was also simulated.

Table 4.8: Surface Acoustic Power Level (SWL) for the three fan models under 535 rotation speed and 800 m^3/h.

Fan Model	Velocity $[RPM]$	Airflow $[m^3/h]$	Pressure Drop $[Pa]$	Area Avg.SWL $[dB]$	Fan Efficiency [%]
Standard Fan			45,8	51,1	13,1
Dimpled Fan	535	800	48,7	48,2	15,0
Hexagonal Fan			47,3	48,0	13,5

Unfortunately, unlike the isosurface presented in Chapter 4.3.4, the Isosurface illustrated in the Figure 4.34 represents the surface where there is velocity 0 m/s, which means that the surface of the blade itself will appear represented by the isosurface as well as the phenomena associated with the separation of the boundary layer.

With the isosurface analysis of the standard blade model it is possible to observe the flow separation of the blade from the leading edge to the trailing edge in the hub region. This represents the generation of a vortex that develops along the radial direction triggering boundary layer separation and eddies in the middle of the blade to trailing edge. The developed eddies will propagate to the neighbour blade. These characteristics, observed in Chapter 3.4.2, are indicators of the stall condition.

The blade with the dimples presents the flow still attached to the blade in the region of the hub and this ends up separating due to the transverse pressure gradient, forming the well developed hub corner separation that will affect the attachment of the flow to leading edge of the neighbour blade. The same is true for the blade with the hexagonal pattern and in this case a small zone of total detachment near the hub is already developed, representing the beginning of a circular vortex that leads to the stall. This suggests that the circular pattern is more efficient in controling the occurrence of stall compared to the hexagonal pattern.

The comparison of the results of the table also identifies the blade with circular dimples is more efficient than the blade with hexagonal dimples, which follows the observations from Chapter 4.3.6.

In spite of these results, the Figure 4.35 shows the region of the hexagons with an acoustic emission considerably lower than the dimples, in particular close to the trailing edge of the blade.

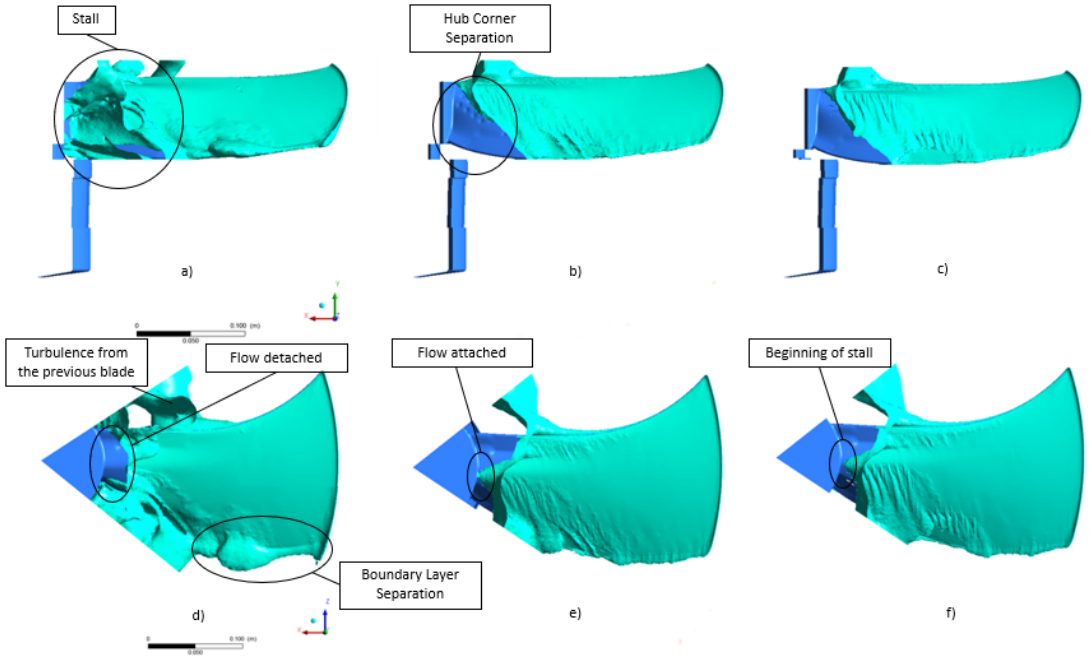

Figure 4.34: Isosurface with v= 0 m/s for: a) standard fan front view, b) dimpled fan front view, c) hexagon fan front view, d)standard fan top view, e) dimpled fan top view and f) hexagon fan top view.

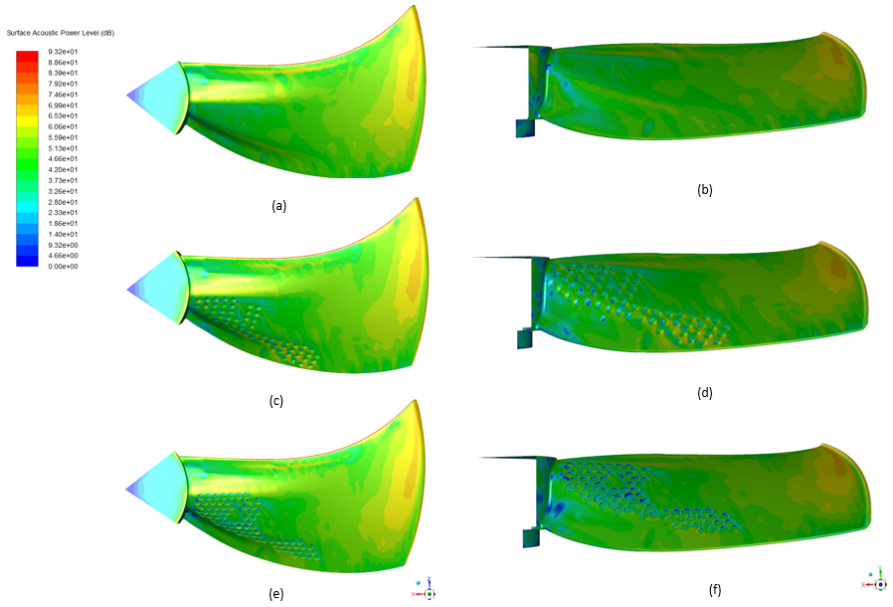

Figure 4.35: Surface Acoustic Power Level contours of the three models: a) standard top view, b)standard front view, c) dimpled top view, d) dimpled lateral view, e) hexagon top view and f) hexagon lateral view.

4.5 Conclusions

The concept of adding dimples to a low velocity axial fan is innovative. The following conclusion have been draw from the parametric study on the application of dimples in the original ⌀630 fan:

- When the flow along the suction surface of the airfoil enters the dimple, a reverse flow is formed inside the cavity. As a consequence the vortex generated inside the cavity mixes the main flow with the boundary layer flow energizing it. This leads to an increase of kinetic energy in the boundary layer after the dimple. This increase is represented by the accelerated velocity profile of the flow after the cavity, making it able to penetrate the high adverse pressure zone until the flow decelerates, and then flow separation occurs.

- The optimization study shows that the location of the dimples is one of the most important parameters in the optimization process. When the dimple is located at the point of separation, it is observed a shift in the boundary layer separation of 8.1%. The placement of a dimple in upstream from the separation point shows no effect on the flow characteristics.

- The comparison between the different shapes of dimples shows that the circular dimple energize more the flow promoting the mixing of the main flow with the boundary layer. This leads to an increase of 0.6% on the shift of the boundary layer separation in comparison with hexagonal dimple. In addition, the circular dimple distributes more uniformly the flow in its cavity resulting in a smaller increase of the skin friction coefficient.

- The introduction of dimples after the point of separation increases the shift of the boundary layer significantly. The pattern with 3 dimples with spacing of 1 mm showed an shift of the boundary layer by 7% in relation to airfoil with a single dimple, and 15.1% in comparison to the standard airfoil. Different patterns showed a evenly flow separation line, but there were no improvements in the shift of the boundary layer.

- Skin friction lines provide a method to identify the location of separation and attachment of the flow in different aeroacoustic phenomena, such as the vortex roll-up, the hub-corner separation and the leading edge vortex. The location of the separation line is a crucial factor for an successful application of dimples. The skin friction lines allow the application of this feature in different fan geometries.

- The flow separation line fluctuates with the variation of $airflow$ and the rotation speed of the fan. The flow separation line is prone to come closer to the leading edge for low airflow operating points.

- The use of the optimized dimples pattern in a standard fan with operating point between 2000 m^3/h and 4000 m^3/h shows a shift in the separation of the main flow, leading to inhibition of the generation of hub corner vortex, and resulting in a reduction potential of 0.3 - 0.8 dB.

- The improvement of the flow attachment in the fan with dimples leads to the shift of the aerodynamic stall condition, resulting in a reduction of 1.9 dB for the stall operating point of the standard fan.
- An increase in fan efficiency with dimples is verified for lower airflow of 3000 m^3/h. This is due to the shift of the stall condition, which leads to less blockage of the main flow. After 3000 m^3/h, a decrease of the efficiency of the blade with dimples is verified, a result that was expected for these range of speeds due to the increase of the skin-friction coefficient inside the cavities.

Chapter 5

Bio-Inspired Trailing Edge Noise Control

With the aim of reducing the trailing edge noise of the fan, two different noise reduction features inspired by the owl's wing were introduced: the finlets and a flexible trailing edge.

The noise benefits from finlets have been studied by several authors [49], but most of the studies are applied to wind turbines to which an high-Reynolds regime is associated. Therefore, the finlets were designed and applied to the original fan and compared with the standard model, exposing how finlets effect the flow in a low to medium Reynolds number regime.

In recent years, a greater focus has been given to the study of the flexibility of owl's wing trailing edge since this is the owl's noise suppression technique that has been less investigated. Theoretical models and experimental studies were conducted by Talboys et al. [50], but numerical simulation is still necessary for a better evaluation of the self-oscillation mechanism of the flexible trailing edge and its influence on the flow. This study intends to adapt this feature to the ⌀630 fan and analyze the phenomenon through numerical simulation. Unfortunately, the blade with an elastic trailing edge was not possible to model due to the complexity of the numerical simulation. As an alternative it was simulated the airfoil with radius = 290 mm though the meridional flow method described in the Chapter 3.3. The rigid trailing edge of the airfoil was replaced by a elastic one, and its oscillatory behavior was qualitative evaluated with the rigid airfoil.

5.1 The Structure of Owls' Wings

Owls are known for their silent flight to reach their prey without being detected. In recent years there has been a great efforts of research in order to identify the different mechanisms of acoustic camouflage and their application in aerodynamic applications. Aeroacoustic studies applied to the flight of owls show that they are able to largely eliminate noise emissions between 1.6kHz and 10kHz and these are the frequencies at which human hearing is most sensitive [51].The aeroacoustic benefits of owl wings have been studied by several authors over the years, identifying three distinct characteristics of the remaining species:

- Soft coating on the upper surface of the wing - modifies the boundary layer turbulence as it approaches the trailing edge, damping small eddies that generate high frequency noise. The eddies would be damped at frequencies lower than the frequencies at which viscous dissipation normally occurs [52].

- Curved serration at the leading edge - the serrations triggers a bypass transition leading to the boundary layer becoming turbulent relatively close to the aerofoil's leading edge. The study [53] compare two airfoils with straight serration and another with curved serration, showing that a curved serration outperforms the straight one by a 5 db reduction, when it had a large radius of curvature and small angle of inclination. The author believes that the peak of the curvature of the serration acts as a shield that removes the turbulence generated by the serrations themselves, without a large drag penalty [53].

- Fringe of flexible feathers at the trailing edge of the wing - theoretical models predict that the elastic behavior serves as a pressure-release mechanism for pressure fluctuations as they approach the trailing edge [52].

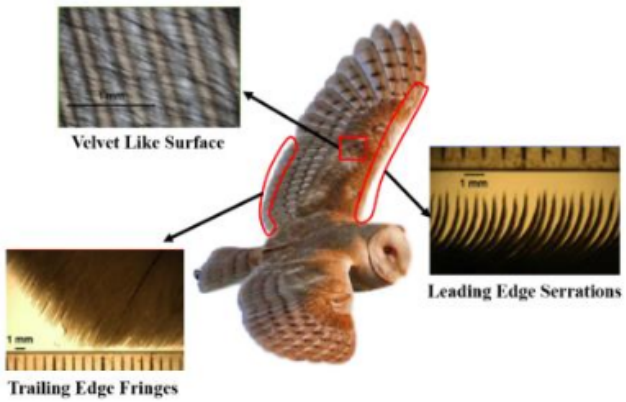

Figure 5.1: Unique features of the owl's wing feathers that enable a silent fly. Photographs through a microscope of top: soft coating right:leading edge serrations, down: flexible trialing edge fringes [54].

5.2 Finlets

This section aims to evaluate and adapt the solution inspired by the down coat of the owl studied by Clark et al. [52]: the finlets. When the finlets are applied to the trailing edge of a wind turbine, they reduced the trailing edge broadband noise by 10 dB. The solution shows great interest when applied to wind turbines, which operate under high Reynolds numbers. Since the fan under study operates in low-velocities, it was necessary to identify the characteristics of the flow that influence the geometry of the finlets according to the author. The aeroacoustic comparison at different velocities was made between the standard fan and the fan with finlets applied to the trailing edge.

5.2.1 The Effect Of Finlets

The finlets were developed taking into account the velvet like surface of the owls feathers [52]. This consists of small hairs emerging from the surface of the feather and soon after they end up bending. Test in wind tunnels show that this type of fibers reduce far-field noise but certain configurations generate high-frequency noise. The results of these tests inspired the finlet geometry, being modified more than 20 times due to the multiple parameters that can be manipulated in its geometry. The author [52] mentions that the set of finlets is responsible for reducing the speed of the free flow between the finlets and consequently the pressure fluctuations at the surface. It also mentioned that finlets break large scale eddies that are one of the major sources of far-field noise.

Geometry

An increase in drag is expected due to the nature of the flow on the surface of the blade, and it was necessary to adjust the direction of the finlets so that they are aligned with the flow. The finlets were placed on the trailing edge next to the tip where the highest speeds are expected. Clark et al. [52] identifies the height and spacing of the finlets as the most important parameters, stating that the recommended height should be 25%-50% of the boundary layer. An similar study of airfoil in Chapter 4.3, for 300 rotation speed revealed a thickness of the boundary layer of 4 mm and therefore the height of the finlets was considered to be 2 mm. The spacing between the finlets was 2 mm. The final geometry is shown in the Figure 5.2.

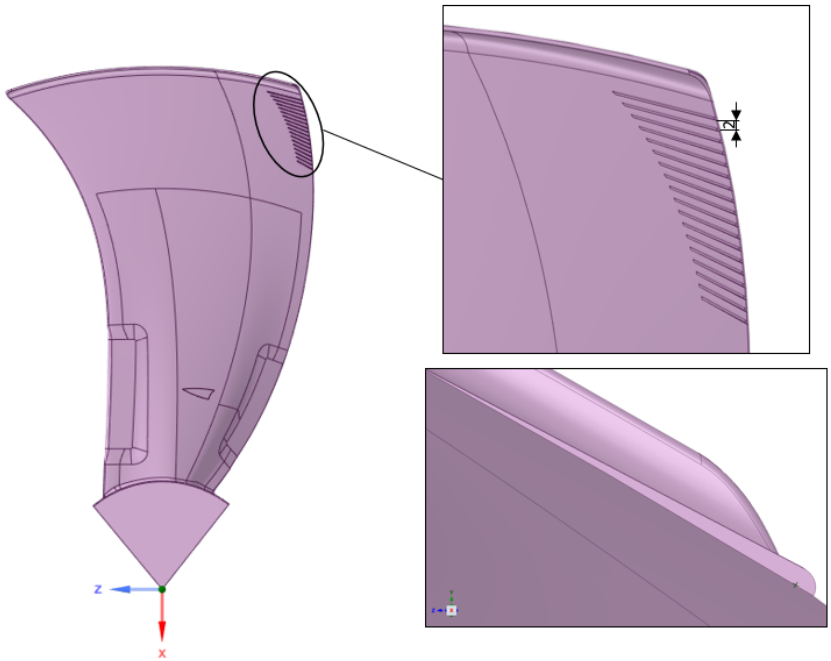

Figure 5.2: Finlets applied to the trailing edge of the ⌀630 mm fan blade.

CFD Model and Mesh

The same mesh and model from Section 4.4.1 was used. The simulation evaluates the blade acoustic power due to the boundary layer and kinetic energy on the blade for different rotation speeds.

Results

The Table 5.1 shows the results of the two models for rotation speeds of 300 RPM, 535 RPM and 700 RPM. It is possible to observe that there is only a reduction of the surface acoustic power for the speed of 300 RPM, while for higher speeds the noise increases, the Figure 5.3 illustrates the effect of the finlets on the surface acoustic level.

The turbulent kinetic energy on the surface of the blade, that represents the velocity of the flow and the generation of vortexes and directly representing the source of trailing edge noise, can be analyzed in Figure 5.4 for the different models. A reduction in the finlet zone is observed. It is possible to notice for that an increase of the rotation speed, the effects of the finlets become less noticed. This makes sense and its geometry depends on the thickness of the boundary layer and this is variable with the fan rotation speed. With the increase in rotation speed the pressure drop of the dimpled model decreases compared to the standard model. This suggests the influence of the finlets on the overall drag coefficient, which is strongly dependent on the speed of the fan.

Table 5.1: Operating points and surface Acoustic Power Level (SWL) for the original fan and the fan with finlets at 300 RPM, 530 RPM and 700 RPM.

Model	Velocity $[RPM]$	Airflow $[m^3/h]$	Pressure Drop $[Pa]$	Area Avg. SWL $[dB]$
Standard	300	1726	15,7	44,1
	530	3477	34,9	48,0
	700	5652	56,3	55,2
Finlets	300	1703	15,7	43,8
	530	3465	35,1	48,3
	700	5569	54,1	56,1

As previously observed the turbulent kinetic energy is reduced near the finlets region at 300 rotation speed. Figure 5.5 shows a comparison of the turbulent kinetic energy in the wake for this operating point. It is possible to observe in the finlet model that the turbulent kinetic energy of the flow is reduced immediately next to the surface of the finlets followed by a increase in the wake after the trailing edge, representing the generation of a vortex with higher velocity than the generated wake. This corroborates the hypothesis presented by Clark [52] after carrying out experimental studies. The author argued that the finlets generate small and strong vortexes that brake the large coherent turbulence coming from the separation of the boundary layer.

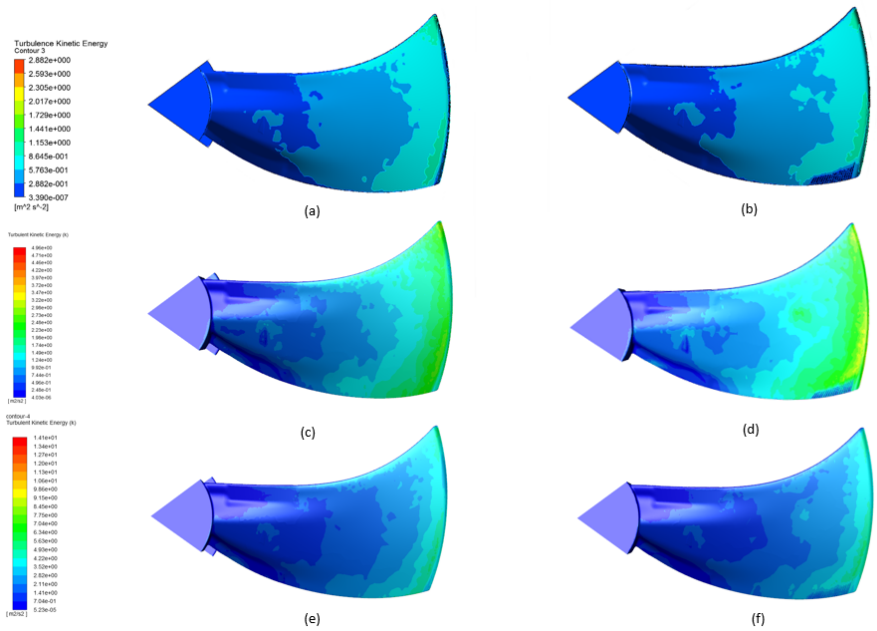

Figure 5.3: Surface Acoustic Power Level contours on the suction side of: a) the simple fan at 300 RPM, b) the fan with finlets at 300 RPM, c) the simple fan at 530 RPM, d) the fan with finlets at 530 RPM and e) the simple fan at 700 RPM f)the fan with finlets at 700 RPM.

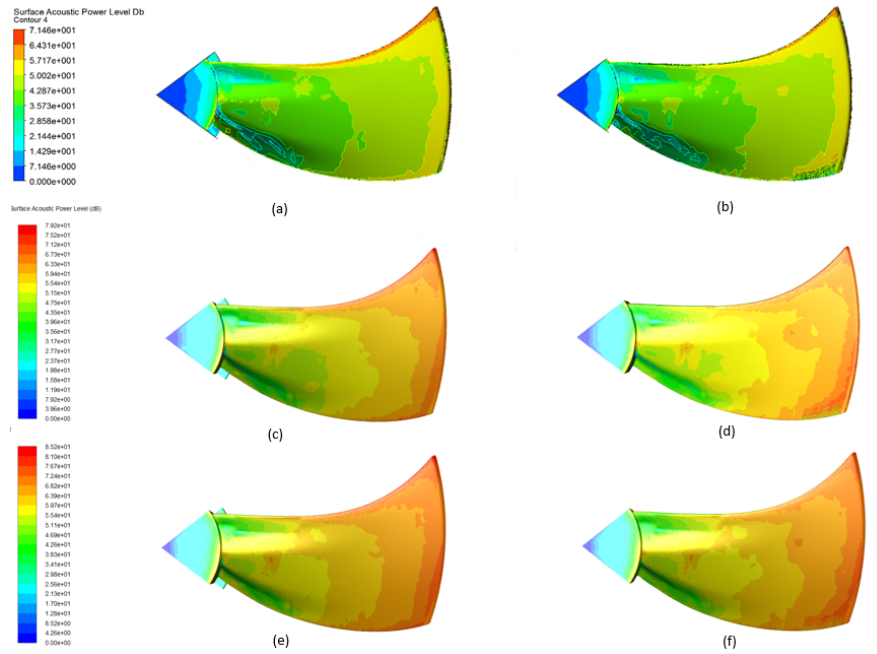

Figure 5.4: Turbulent kinetic energy contours (k) on the suction side of: a) the simple fan at 300 RPM, b) the fan with finlets at 300 RPM, c) the simple fan at 530 RPM, d) the fan with finlets at 530 RPM, e) the simple fan at 700 RPM, f) the fan with finlets at 700 RPM.

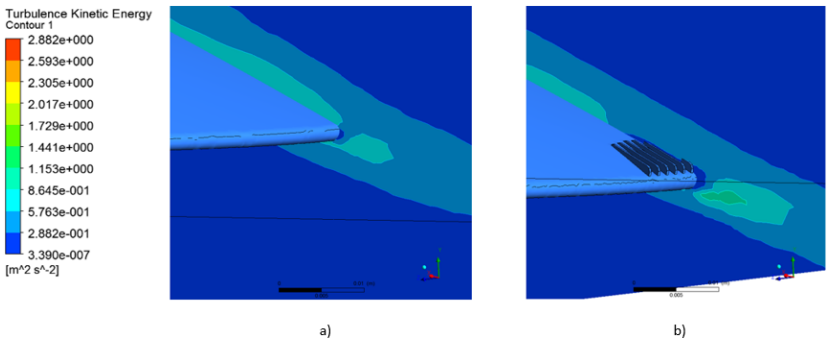

Figure 5.5: Turbulence kinetic energy contours in plane parallel to the finlet at 300 rotation speed: a) original blade, b) blade with finlets.

5.3 Flexible Trailing Edge

In the present study, a novel configuration of a self-oscillation trailing edge, inspired by owl's wing is evaluated. The study was conducted through the meridional flow technique on the airfoil studied in Chapter 3.3. This airfoil was modified to have an flexible material near the trailing edge. The numerical simulation was conducted through fluid structure iteration (FSI) simulation.

5.3.1 The Effect of a Flexible Trailing Edge

The turbulent boundary layer generates turbulence when interacting with the trailing edge, and creates acoustic waves initiating a self-exciting feeedback loop, as explained in Chapter 4.3. In order to mitigate this aeroacoustic phenomenon, several solutions were proposed. The first is the use of porous airfoil, which has already been mentioned in Chapter 2.1.2. Although the advances in this type of airfoil, the penalty in the lift and drag of porous airfoil cannot be eliminated. Another technique used is trailing edge serrations mentioned in Chapter 3.4.2, being this a target of numerous researches. As the interest in bio-inspired features grew, the first study of how the flexible trailing edge of the owl influenced the flow was carried out by Talbois et al. [50] where an array of silicone flaplets were added to a NACA 0012 airfoil. The results show a reduction in the thickness of the boundary layer leading to an overall noise reduction of 1.5 to 2 dB. Jodin et al.[55] used an morphing trailing edge but with oscillation with the same frequencies as Talbois et al. [50] study and the results showed an reduction a 10% in the boundary layer thickness, with a 2% increase in lift.

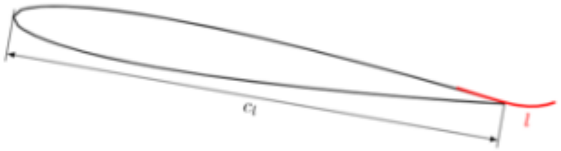

Figure 5.6: Flaplet placement in the suction side of the NACA 0012 airfoil [50].

5.3.2 CFD model

Since the oscillation of the trailing edge induces a pressure wave in the surrounding and opposite fluid, a transient simulation is necessary that includes both domains: the flexible structure and the fluid. The domains have to be coupled in order to evaluate the natural frequencies and the response of the dynamic excitation. In the flow domain, the forces that are applied to the flexible structure by deforming the elements of the mesh are calculated; the non-linear displacement response is transferred to the fluid domain affecting the flow. This two-way transient interaction loop continues through multiple cycles. Since the geometry of the airfoil is the same as the one previously studied in the Chapter 4.3.3, the same turbulence model was used. In order to guarantee the coupling between the simulations, the mesh of the fluid domain was coarser than the one mentioned in the Chapter 4.3.3, this way the elements from the fluid domain align with the mesh of the flexible trailing edge. Thus, the fluid elements are compatible and aligned with the elements of the flexible structure. The different modules of the software ANSYS have been used, the fluent and mechanical linked with the system-coupling module, the workflow can be consulted in the Appendix 3.

Geometry

The geometry shown in Figure 5.7 illustrates the airfoil studied by the meridional flow simplification previously studied in Chapter 4.3.4, where the orange region represents the flexible trailing edge (10% of the chord lenght), modeled with the silicone material with an Young modulus of 0.001 GPa. The remaining section of the airfoil is composed of ABS (the original material). The boundary conditions are the same as those considered in the Chapter 4.3.3.

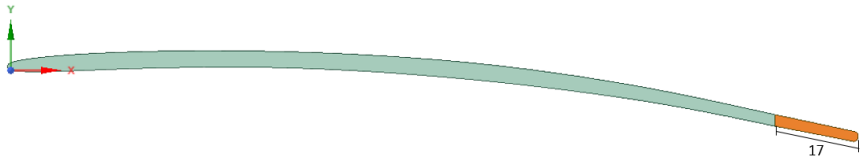

Figure 5.7: Airfoil r=290mm with the orange color representing the flexible part made of silicone.

Fluid Mesh And Structural Mesh

The mesh of the fluid domain has been greatly reduced in size and refinement in comparison with the previous mesh used in Chapter 4.3.3. Only one element was considered in the transverse direction to the airfoil, in order to avoid errors between the coupling of the fluid mesh and the airfoil. In fluent and mechanical domain three and four noded mesh elements were used to ensure a refined mesh near the trailing edge. It was not possible to use inflation layer because the sweep method does not support this function. The little refinement of the mesh and the small domain of the fluid domain lead to a large decrease in the number of elements. The fluid domain presents an estimate of of 30 000 elements while the structural domain presents 1800 elements. The FSI transient simulation was done only for 1.5 seconds of numerical simulation, generating about 140 GB of data.

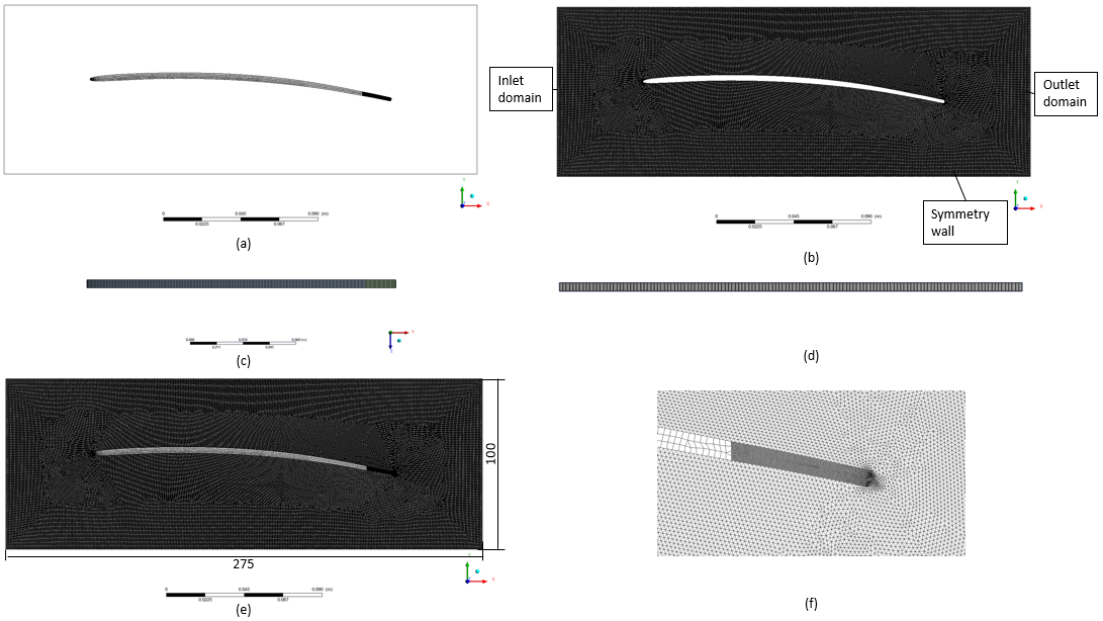

Figure 5.8: The two meshes used in the model: a) front view of the ANSYS Mechanical mesh, b) front view of the Fluent mesh wit the boundary condition used, c) top view of the ANSYS Mechanical mesh d) top view of the Fluent mesh, e) Coupling of the two meshes and f) Mesh alignment between the different meshes and the finer mesh in the flexible trailing edge.

Results

In Figure 5.9 it is possible to observe the streamlines between the conventional airfoil and the airfoil equipped with the flexible trailing edge. For t= 0.01 seconds, although, there is no displacement of the flexible trailing edge. It has an higher speed, creating a decrease of the pressure difference. When the pressure is higher on the suction side, a lift force contrary to expected, is applied, causing the trailing edge to move downwards. This is verified for t= 0.53 seconds where the maximum downward displacement is verified, shifting the separation of the limit layer and its thickness. For this configuration of the airfoil is associated a higher angle of attack, which will lead to the increase of the velocity of the flow in the suction side of the airfoil, making the pressure lower than that of the pressure side, leading the lift force to move the flexible trailing edge upwards until its maximum displacement at t=1.5 seconds. At t=1.5 seconds the considerably smaller angle of attack causes the boundary layer separation to shift. Figure 5.11 shows the surface acoustic power of the different models for the respective simulation time, which revealed small reductions in the trailing edge. A more significant reduction was expected, taking into account the qualitative reduction in the thickness of the airfoil turbulence, suggesting that the mesh is not fine enough for the acoustic model or the acoustic model is not suitable for this analysis since the experimental study conducted by Talboys et al, [50] showed improvements in tonal noise and the chosen model is more suitable for prediction of boundary layer broadband noise.

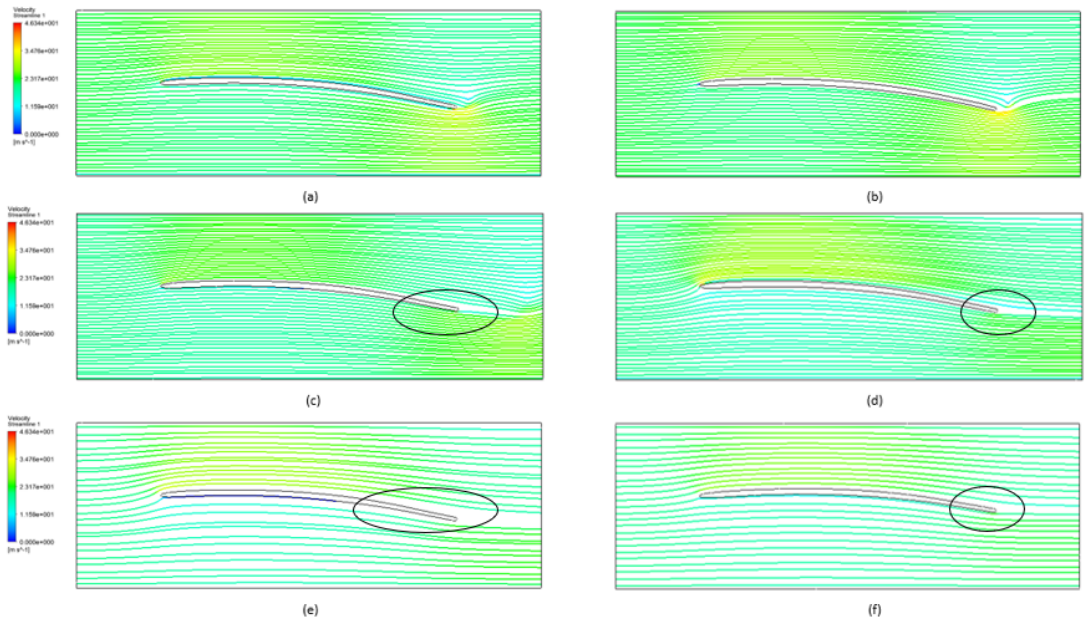

Figure 5.9: Velocity streamlines for the equivalent u_∞ of 800 rotation speed, and boundary layer turbulence thickness represented inside the circle: a)standard airfoil for t=0.01 seconds, b)airfoil with flexible tailing edge for t=0.01 seconds, c)standard airfoil for t=0.53 seconds, d)airfoil with flexible tailing edge for t=0.53 seconds, e)standard airfoil for t=1.5 seconds and f)airfoil with flexible tailing edge for t=1.5 seconds.

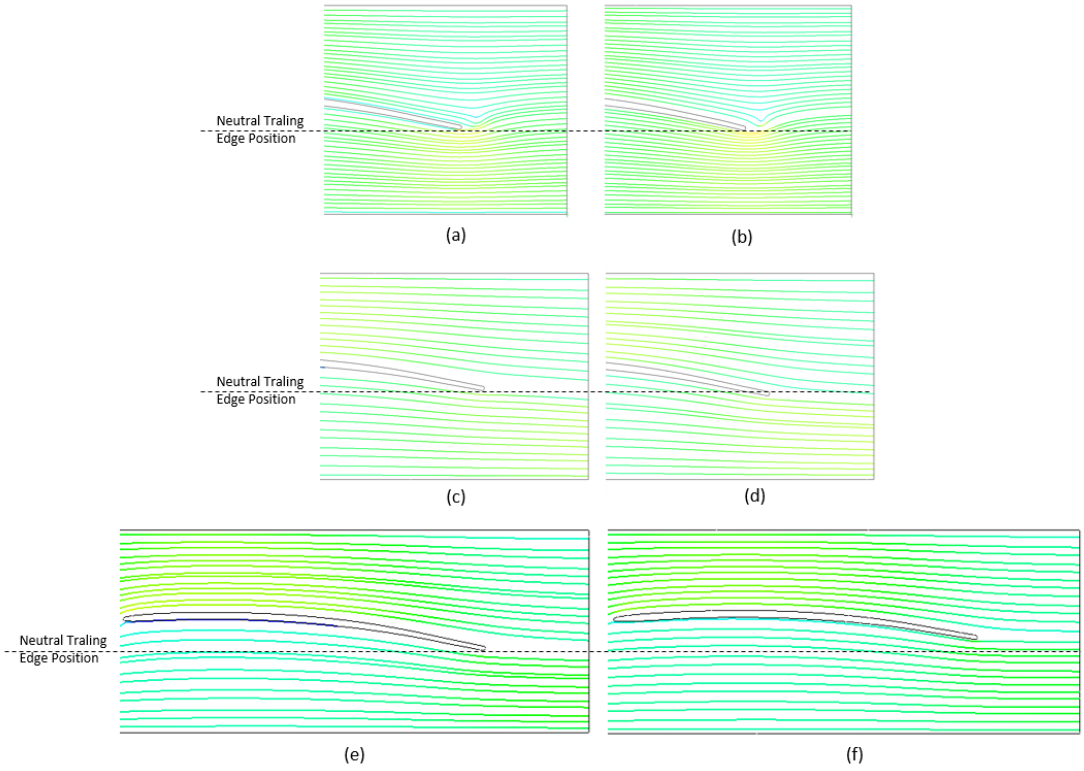

Figure 5.10: Relative position of the trailing edge a)standard airfoil for t=0.01 seconds, b)airfoil with flexible tailing edge for t=0.01 seconds, c) standard airfoil for t=0.53 seconds, d) airfoil with flexible tailing edge for t=0.53 seconds, e) standard airfoil for t=1.5 seconds and f) airfoil with flexible tailing edge for t=1.5 seconds.

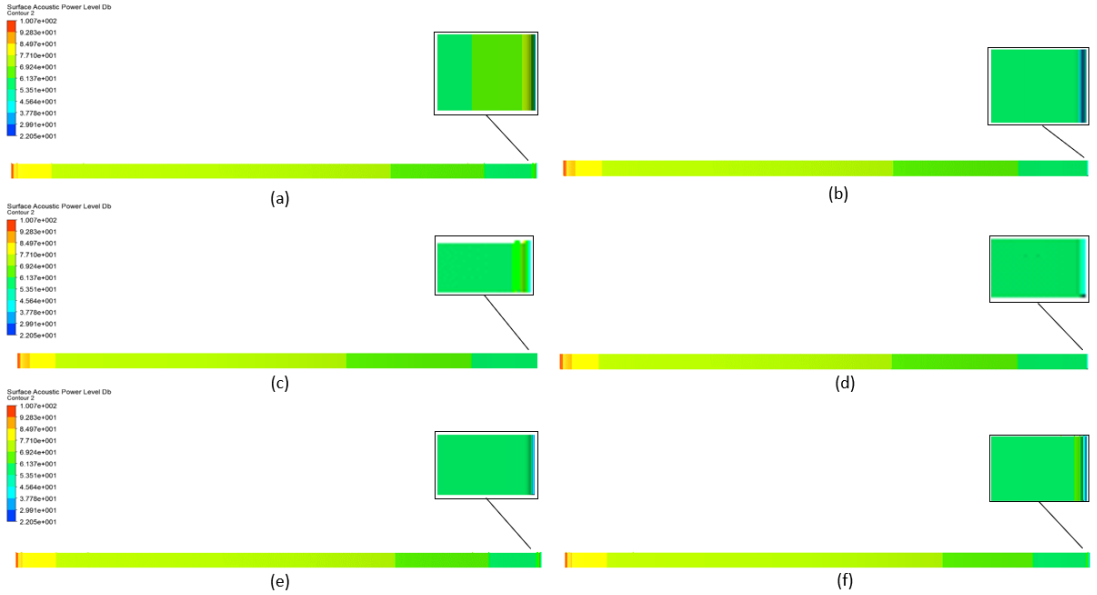

Figure 5.11: Surface Acoustic Power Level contours of the two models for a)standard airfoil for t=0.01 seconds, b)airfoil with flexible tailing edge for t=0.01 seconds, c)standard airfoil for t=0.53 seconds, d)airfoil with flexible tailing edge for t=0.53 seconds, e)standard airfoil for t=1.5 seconds and f)airfoil with flexible tailing edge for t=1.5 seconds.

5.4 Conclusion

Given the results obtained with the two features inspired by the owl feathers analyzed in this chapter, the following conclusions can be drawn:

- Finlets have a positive effect on reducing trailing edge noise when their geometry is optimized for the present flow on the fan.
- The results suggest that the finlets increase the coefficient of drag of the blade, acting as a bump in the flow.
- The finlets are a potentially a valid feature to be implemented in the fan that operates at low and constant rotational speeds, characteristics that are present when the heat pump is in night mode.
- The turbulent kinetic energy increase near the wake region and supports the experimental tests conducted by Clark et al. [52] that suggest that an increase of the turbulence kinetic energy on the wake might be beneficial to attenuate larger eddies.
- The flexibility of the trailing edge allows the displacement in the downward direction in order to balance the pressure mismatch between the pressure side and suction side of the airfoil. Then, the upward movement decreases the angle of attack by placing the airfoil in the direction of the flow. Both movements lead to a decrease in the boundary layer turbulence thickness, which is directly related to the trailing edge noise, motivating the interest for further investigations.

Chapter 6

Experimental Study

The following experimental study aims to evaluate the noise emission of the dimpled fan studied in Chapter 4.4.3, applied to the external heat pump unit. Prototyping dimples to a rotating propeller presented some challenges related to the design and size of the fan itself. Thus, in order to replicate the cavities of the different dimples, two different patterns were trimmed in a self-adhesive sticker with the same thickness of the depth of the dimples and then the sticker was applied to the ⌀630 fan. The experimental study was conducted in a hemi-anechoic chamber where the Acoustic Power level of the different fan models was compared with the standard fan. A second study was conducted in an attempt to reduce the inlet airflow in order to induce the aerodynamic stall, since the dimples showed a bigger noise reduction before reaching this type of flow regime.

6.1 Model prototyping

In order to study the effect of the dimples, two patterns were applied to the standard fan. For the adhesive material, paper and acrylic with thickness of 0.4 mm and 0.8 mm were chosen in order to get a thickness equal to the depth of the dimple cavity. Unfortunately, it was not possible to prototype the circular dimples due to the complexity of the cavity shape. The simulation of the hexagonal dimples have shown identical results on flow in relation to circular dimples. However, inferior results are expected for hexagonal geometry, due to the lower wake energization, as seen in Chapter 4.3.5. The different patterns were trimmed with a CO_2 laser cutter with tolerance of 0.005 mm. In order to make the transition between the sticker and the blade as homogeneous as possible, 5 mm of plasticine was placed between the two components. The plasticine was weighed previously to avoid unbalance the different blades. Therefore, a negative effect is expected due to the roughness of the plasticine.

6.2 Experimental Setup

The acoustic measurements were conducted inside Bosch's hemi-anechoic chamber. The sound test was conducted in accordance to the ISO 3144 with the change in orientation of microphones 1 and 3 due to the high dimensions of the mid chassi. This change was made to guarantee a distance of 1 meter from the center to the the microphone 1 and 3 according to the ISO 3144. Therefore, the two microphones were moved 45º from their

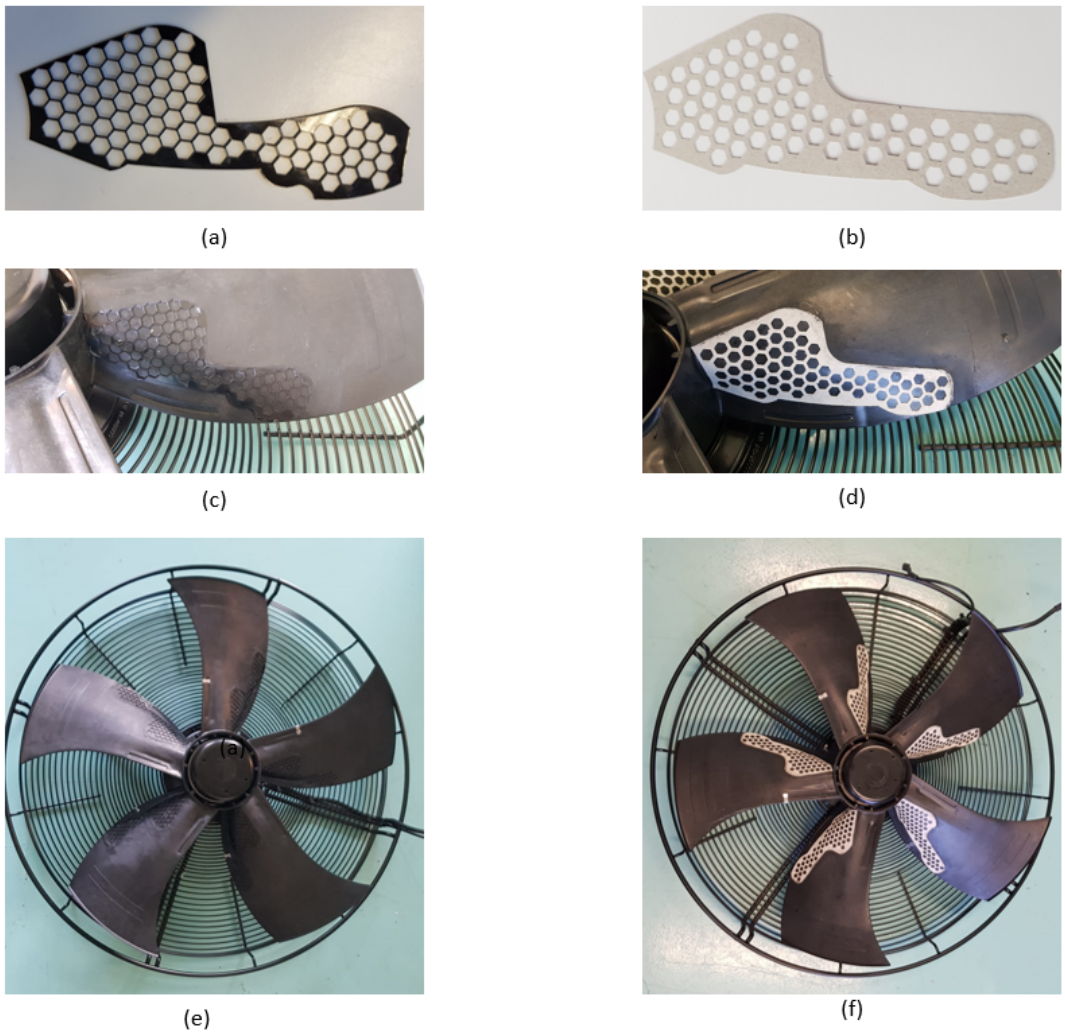

Figure 6.1: Dimpled Fan models prototype a) acrylic sticker with 0.8 mm of thickness and hexagonal dimples with ⌀4.34mm and 1mm of spacing. b) 320g paper sticker with 0.45 mm of thickness and hexagonal dimples with ⌀4.34mm and 2mm of spacing. c)acrylic sticker applied to the blade d)paper sticker applied to the blade e)final 0.8mm hexagonal dimpled fan model f)final 0.45mm hexagonal dimpled fan model.

original position to the outlet side of the fan. This position change can be observed in the Figure 6.2.

The Sound Power Level measurements were performed using 9 PCB ICP microphones (378B02) with windshield mounting (Audio CA132), with a frequency range between 20Hz and 20kHz.The microphones were calibrated to 94 dB by Rion Sound Calibrator NC-74 at 1000Hz. The HeadLab Compact24+12 channel module data acquisition equipment was used,with a measuring frequency range between 1Hz and 24kHz. The software used for the data acquisiton and analysis was the HEAD Acoustics 8.1.

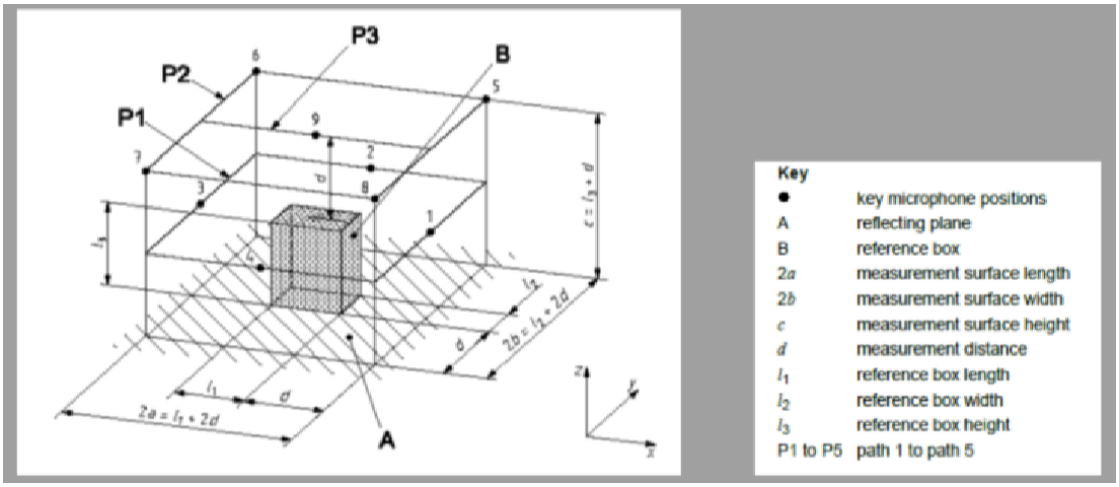

Figure 6.2: Experimental test setup: microphones distribution and setup inside the hemi-anechoic chamber: microphone 1 and 3 distance 1 m from the center; microphones 2 and 4 distance 1,22 m; 1,17 m distance from the floor to the center and 1,23 m from center to microphone 9. Overall dimensions are 2,5x2,5x2,5 m.

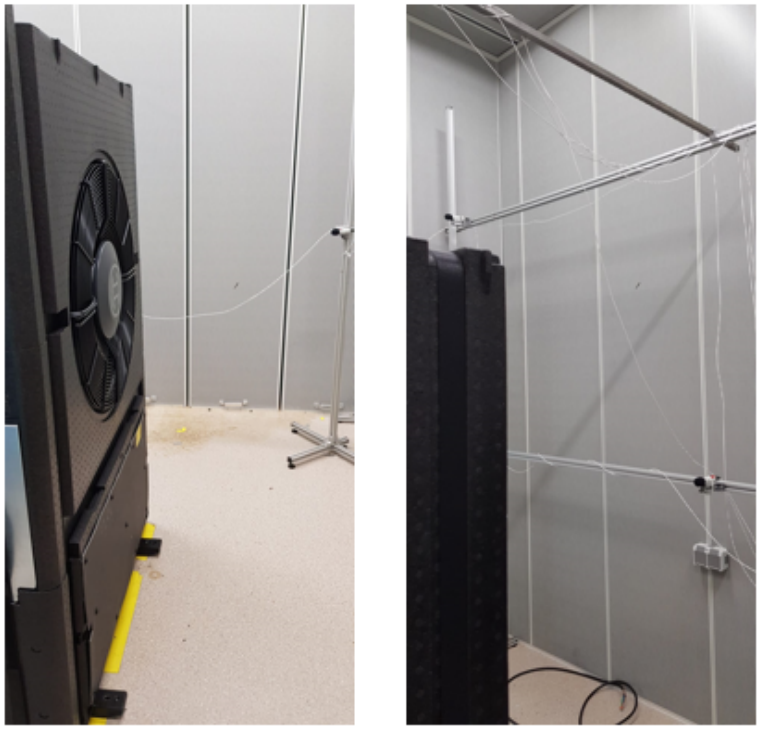

Figure 6.3: Experimental test setup: a) modified location of the microphone 3 b) setup of the microphones 2 and 5.

6.3 Measurements

6.3.1 Performance and Acoustic Measurements

The first test consisted in comparing the noise emitted from the dimpled fan models with the standard fan model. Thus, different motor input voltages were tested and the rotation speed of the fan generated from the different models and the sound pressure level of the far-field were measured. This experiment had two phases, in a first phase two standard fans were tested, denominated standard 1 and standard 2. Subsequently, the adhesive stickers were applied to these standard fans and the tests were repeated. The different models were installed in the heat pump, and its hydraulic system was turned off during the tests to remove this contribution from the noise emission. The only active element was the fan motor. The rotation speed were measured by an strobe tachometer with associated error of 0.5 rotation speed.

In the analysis of Table 6.1 and 6.2 it is possible to observe that for the same input voltage (2V-3V) of the motor it is generated one more or in some cases two different rotation speeds for both models with dimples, at low speeds. This was verified for both dimpled fan models, which suggests that it is not an error associated to the measuring device. In spite of a speed increase, the opposite effect was expected due to the increased in weight of the prototype fan.

Table 6.1: Comparison of the SPL between the 0.8 mm thickness hexagonal sticker fan model and the standard model to the increase of input voltage in the motor.

Fan	Motor Input Voltage $[V]$	Velocity $[RPM]$	SPL $[dB(A)]$
Standard 1	2,0	200	36,5
	3,0	288	42,2
	4,0	380	46,7
	5,0	470	54,4
	6,0	564	58,8
	7,0	649	62,5
	8,0	740	65,9
Hexagonal 0,8 mm	2,0	202	36,0
	3,0	290	41,7
	4,0	381	46,2
	5,0	471	53,9
	6,0	565	58,6
	7,0	649	62,1
	8,0	740	65,5

Table 6.2: Comparison between the 0.45 mm thickness hexagonal sticker fan model and the standard model to the increase of input voltage in the motor.

Fan	Motor Input Voltage $[V]$	Velocity $[RPM]$	SPL $[dB(A)]$
Standard 2	2,0	198	36,2
	3,0	285	41,8
	4,0	377	46,6
	5,0	471	54,3
	6,0	565	58,8
	7,0	649	62,5
	8,0	740	65,6
Hexagonal 0,45 mm	2,0	200	36,0
	3,0	286	41,5
	4,0	378	46,5
	5,0	471	54,3
	6,0	565	59,4
	7,0	649	62,9
	8,0	740	65,9

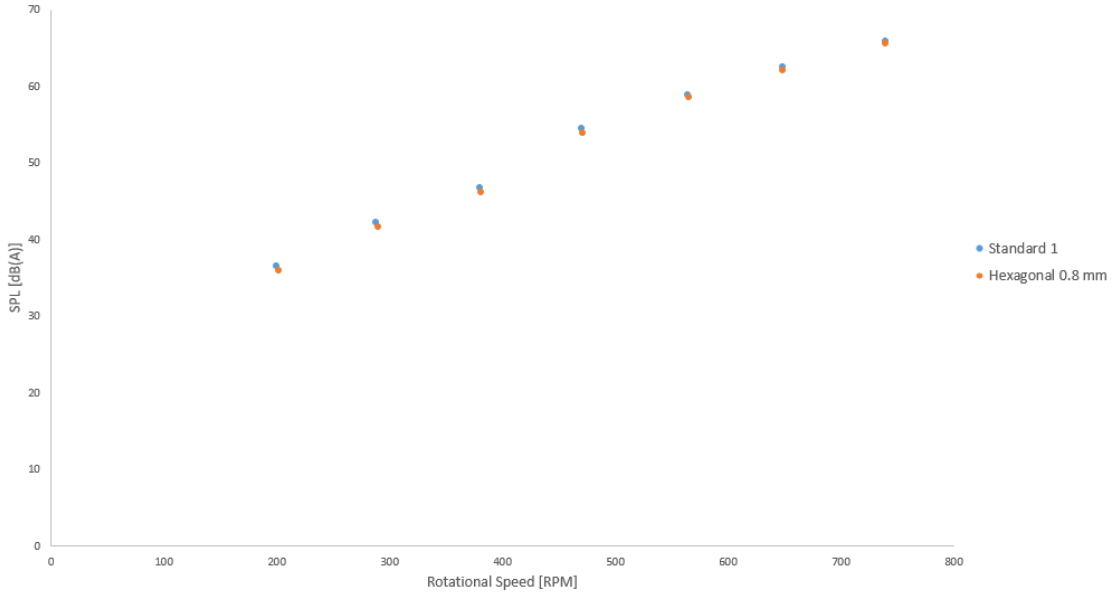

Figure 6.4: Far-field Sound Pressure Level measured inside the hemi-anechoic chamber for the standard and 0.8 mm acrylic hexagonal fan at different rotation speeds.

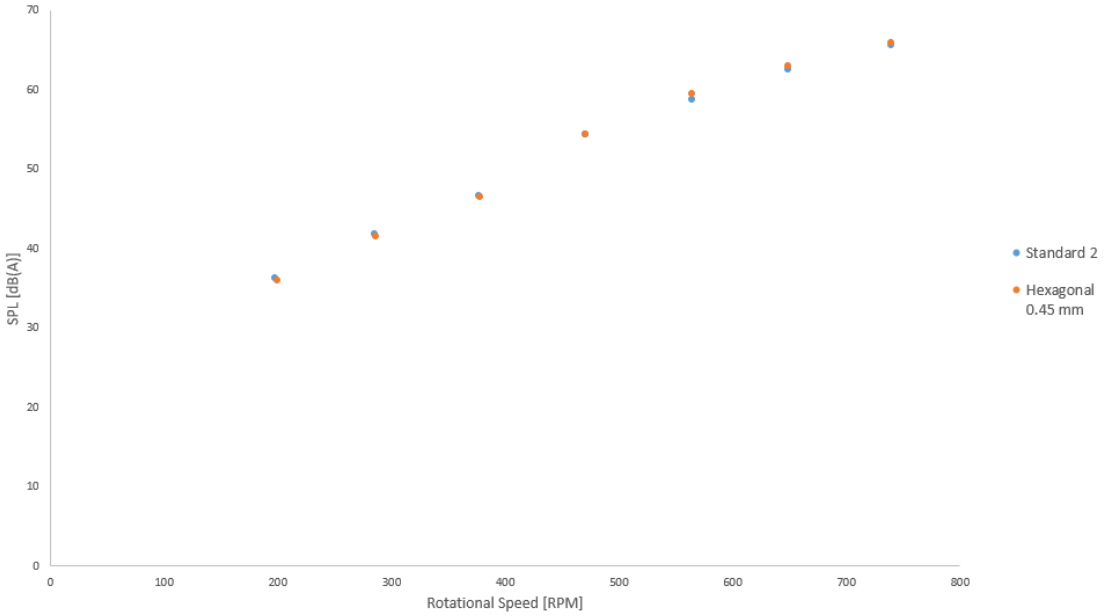

Figure 6.5: Far-field Sound Pressure Level measured inside the hemi-anechoic chamber for the standard and 0.45 mm paper hexagonal fan at different rotation speeds.

In addition to the small increase in rotation speed there is a reduction of 0.5 dB for low to medium velocities in the fan with hexagonal dimples with 0.8 mm depth. It should be noted that with a slight increase in speed, the noise emitted increases, and it is expected that the noise reduction will be greater for 380 rotation speed. For all speeds

the FFT graphs show a reduction between mid-to-high frequencies(Figure 6.6 and 6.7). This frequency range is associated with the noise emitted by the flow separation shown in Chapter 3.4.1. Therefore, the results suggest an increase of the fan performance for lower speed where the penalties of increased drag by the roughness of the plasticine and increase of the blade thickness have less influence on the flow. The fan with hexagonal dimples with a cavity spacing of 2 mm and 0.45 mm of thickness shows worst results than expected and a possible explanation of the paper roughness affect on the free-flow.

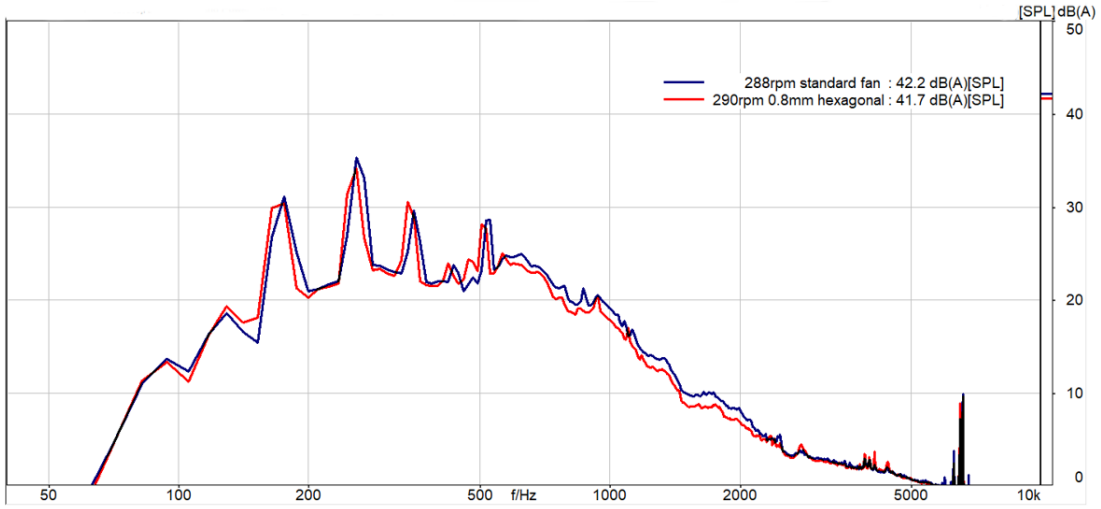

Figure 6.6: Representation in the frequency domain of the A-weighted sound pressure level dB(A) of the hexagonal dimpled and standard fan rotating at 288 rotation speed.

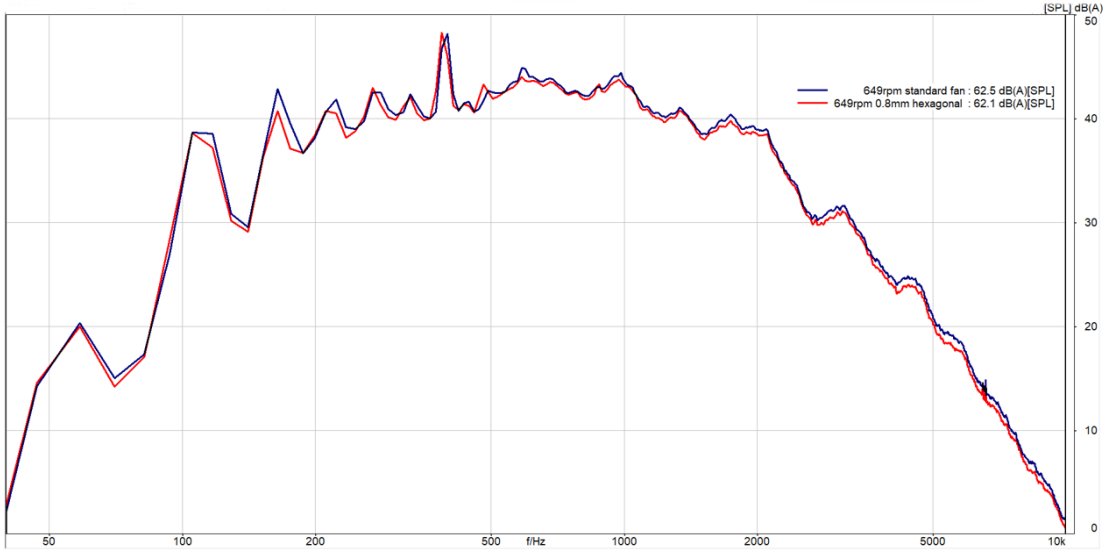

Figure 6.7: Representation in the frequency domain of the A-weighted sound pressure level dB(A) of the hexagonal dimpled and standard fan models rotating at 649 rotation speed.

6.4 Airflow Near Stall

In an attempt to induce a stall condition in the dimpled fan model since it showed the most noise reduction from the results of the previous section, the inlet of the fins (evaporator) was obstructed with adhesive tape (Figure 6.8), in order to force a decrease in the airflow. The velocity of the flow was verified in different points of the evaporator inlet, and the average of these values was considered. This measurement was made with an airflow meter CPS ABB-200 with accuracy of 0.5%. The results are presented in Table 6.3, where the fan with hexagonal dimples of 0.8 mm thickness and 1 mm of spacing is compared with the corresponding standard fan.

Figure 6.8: Outdoor heat pump fins (inlet) obstructed with tape.

The results show to be in agreement with the simulations obtained in Chapter 4.4. For airflows higher than 2000 m^3/h the expected reduction is much smaller than for lower airflows. This noise reduction on a larger scale, followed by a peak with both models with very similar noise levels, suggests the occurrence of aerodynamic stall in the fan. This observation follows the simulation results described in Chapter 4.4, which showed the same behaviour for airflow values of 1500 m^3/h. This reduction is due to the fact that the standard fan increases its noise along low-to-mid frequencies, which can be seen in Figure 6.11, while the dimpled fan stayed similar to the previous airflow FFT, providing a reduction of 0.9 dB. This increase correlates with the phenomenon of light stall studied by Moreau et al. [56] in airfoils, that shows the increase of low-mid frequency noise for the a light-stall condition.

Table 6.3: Far-field Sound Pressure Level measured inside the hemi-anechoic chamber for different operating points of the standard and 0.8mm thickness hexagonal sticker fan at 535 rotation speed.

Fan	Velocity $[RPM]$	Inlet Area $[m^2]$	Average Speed $[m/s]$	Airflow $[m^3/h]$	SPL $[dB(A)]$
Standard 1	535	0,945	1,49	5071	56,5
		0,439	1,90	3003	58,1
		0,253	2,13	1937	62,7
		0,220	2,25	1782	63,1
		0,200	2,35	1692	62,5
Hexagonal 0,8 mm	535	0,945	1,50	5103	56,3
		0,439	1,95	3082	58,1
		0,253	2,10	1913	62,4
		0,220	2,30	1822	63,2
		0,200	2,36	1699	61,6

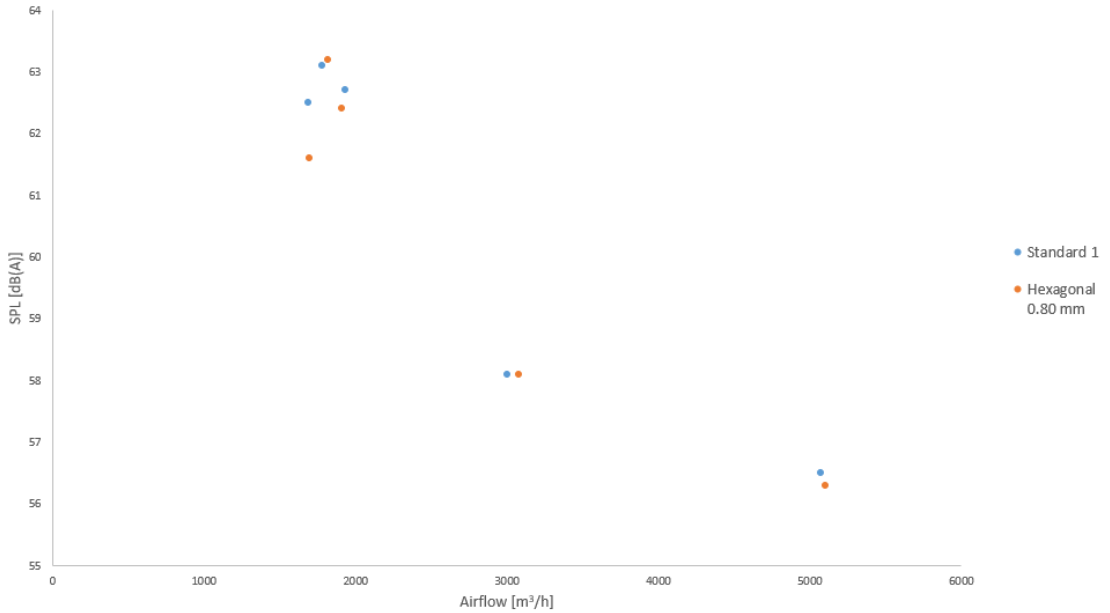

Figure 6.9: Far-field Sound Pressure Level measured inside the hemi-anechoic chamber for different operating points of the standard and 0.8mm hexagonal fan at 535 rotation speed.

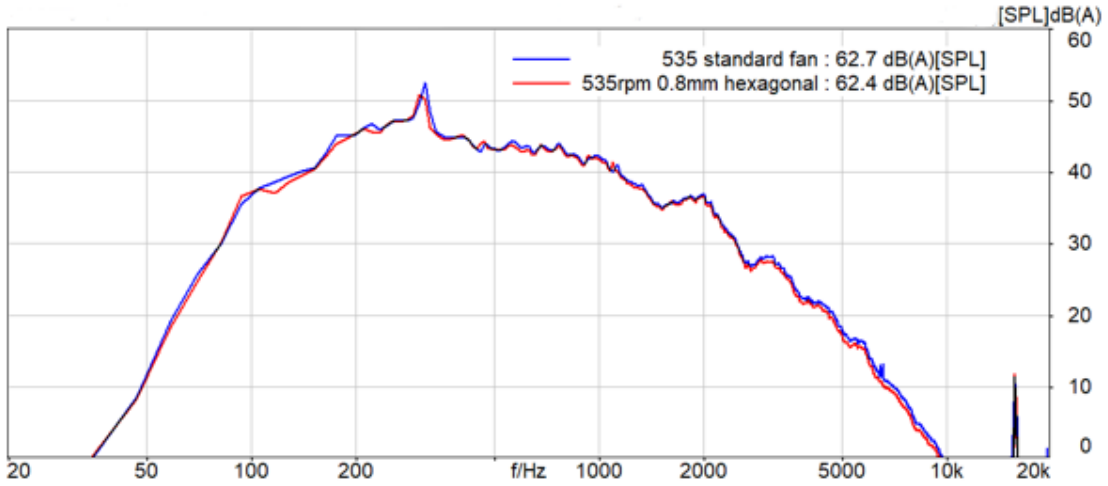

Figure 6.10: Representation in the frequency domain of the A-weighted sound pressure level dB(A) of the dimpled and standard fan models rotating at 535 rotation speed and approximately 1800 m^3/h.

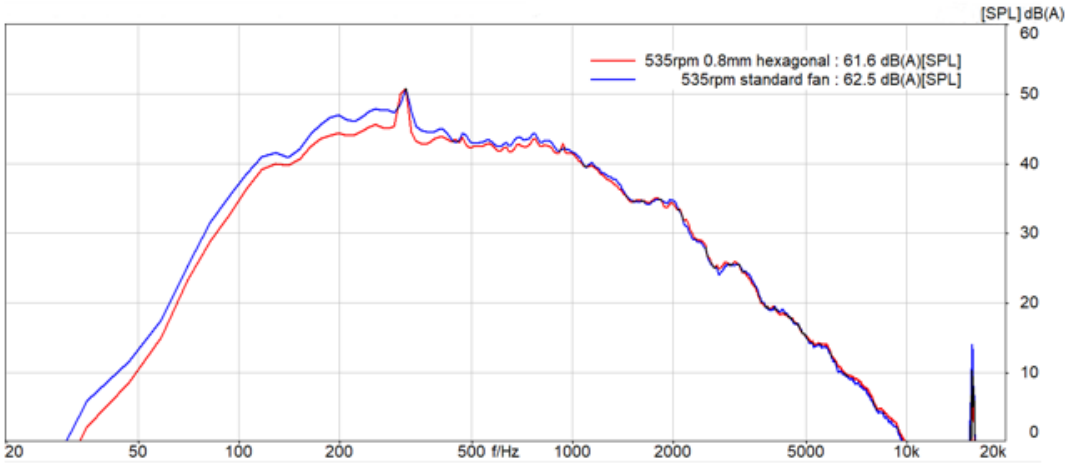

Figure 6.11: Representation in the frequency domain of the A-weighted sound pressure level dB(A) of the dimpled and standard fan models rotating at 535 rotation speed with inlet and approximately 1700 m^3/h.

6.5 Conclusions

- The application of the sticker and the plasticine on the surface of the fan blade, to obtain the model with dimples, might had a strong influence on the aerodynamic noise produced by this upgraded geometry. In fact, the difference of the surface roughness of the added feature and the presence of the sticker, acting as a bump to the flow, may have been responsible for a harmful disturbing effect (turbulence) on the boundary layer.
- At low speed, the fan with the dimpled sticker showed for the same motor voltage a slight improvement of one two rotation speed compared to the original fan. This suggests a small increase in fan efficiency for low speed conditions as predicted by the numerical simulation of the model.
- The dimpled fan showed a noise reduction up to 0.5 dB(A) for its main operating points.
- The fan with dimpled sticker showed a reduction of broadband noise in mid to high frequencies that goes in agreement with the theory presented in Chapter 3.4.1 for the trailing edge noise.
- The fan with the 0.8 mm thickness dimpled sticker showed a higher noise reduction compared to the 0.45 mm dimpled sticker fan which suggests that a deeper dimple is beneficial, which follows the results of the simulation in Chapter 4.3.5.
- At 1700 m^3/h, the original fan drastically increases the noise emitted at low to mid frequencies, contrary to the fan with dimpled sticker, which suggests a shift in the occurrence of light stall, reducing noise by 0.9 dB(A).

Intentionally blank page.

Chapter 7

Summary and Future Work

7.1 Concluding Remarks

Along this work, an analysis of aerodynamic noise on heat pump fans was conducted. The fan with dimples were studied in terms of optimization and implementation, and the aeroacoustic mechanisms of the finlets and the flexible trailing edge were explored.

A broad study has been undertaken to understand how dimples impact the two-dimensional flow in general, and how the different parameters affect the optimization process of the boundary layer separation control. This study showed that the dimples pattern must be placed at the separation line of the airfoil, this way vortex generated in dimple's cavity energizes the free-flow, accelerating it and making it overcome the adverse pressure gradient. From the parametric optimization analysis, it was found that the location and number of dimples are the parameters that most affect the shift of the boundary layer separation.

The implementation of the optimized pattern in the fan was made through the study of skin friction lines that showed the different locations of the flow attachment and detachment on the blade. The effect of the dimples on this complex three-dimensional flow was evaluated by showing that they control the separation of the boundary layer leading to the inhibition of hub corner vortex generation, reducing the boundary layer noise up to 0.9 dB and increasing the fan efficiency under regular heat pump fan operating conditions.

Since the heat pump does not work in conditions that may be favorable to shift stall formation, it is expected that this result can be used in other industries such as wind turbines where it is beneficial to control stall. This allows to place an higher angle of attack of the blade generating more energy while reducing its noise.

The noise of the heat pump is more noticeable during the night. Therefore, the use of finlets can be a solution to be implemented in order to reduce noise in the heat pump during its night mode. This mode has characteristics of low and constant speed, and at this conditions the finlets have shown to reduce noise by 0.3 dB.

The flexible trailing edge showed to be capable to balance the pressure mismatch between the suction side and pressure side of the airfoil and to adapt the angle of attack to the flow, decreasing the thickness of the boundary layer turbulence. Also, it is important to note that a coarse mesh was used not fulfilling the requirements of the acoustic model used, which may be the possible cause for the boundary layer noise reduction prediction not to be significant.

The experimental study showed that, despite the possible negative effect of the sticker, the noise of the fan was reduced by 0.2 to 0.5 dB(A) and the efficiency of the fan was increased for low speeds. However, the study of the airflow for the different models should be done.

The obstruction of the heat pump inlet showed that at an airflow around 1700 m^3/h the original fan increases considerably the noise at low frequencies, which in the literature is referred to as light stall characteristic, while in the fan with the dimples the low frequencies noise emitted was kept constant suggesting the shift of light stall. The higher the speed of the fans, the lower the noise improvements registered with dimpled fan, which is aligned with theoretical expectations.

Considering that the separation flow is not the main source of aeroacoustic noise of an axial fan, this result is not surprising. Investigation on the effect of the fins (evaporator) on the velocity inlet fluctuations and possible changes in the shroud in order to decrease the reverse tip leakage should be studied.

Overall, considering this work analyzed solemnly the boundary layer effect on the fan broadband noise it became clear how the different features affect the flow. Considering that different acoustic waves are generated by the different components, it is necessary to consider the effect of these waves propagation on other waves produced by other sources, or even if these waves can be absorbed by the geometry or the flow.

7.2 Future Work Suggestions

The possibility of using dimpled fan shows promising aeroacoustic benefits, however it is necessary to evaluate the model within the heat pump unit trough numerical simulation without sacrificing the mesh quality. This way the effect of the fins on the velocity inlet fluctuations of the fan can be evaluated, which will affect the boundary layer in a great extent.

Regarding the experimental measurements, it is important to repeat them with a prototype with the dimples cavity on the blade surface. Only then, the concrete noise reduction can be drawn from the model. Additionally, a more detailed study of the airflow in the heat pump should be done in order to obtain lower airflow reaching the full stall condition. A study with fixed rotation speed of the different model should be conducted. Since, during experimental study it was only possible to control the motor voltage input and when an increase in efficiency and noise reduction was observed, this noise reduction is expected to be higher due to the fact that the rotational speed has increased a increasing the noise generated.

The finlets proved to be a potential solution to implement in order to optimize the heat pump noise during its night mode, the different parameters of the finlets geometry were collected from the study by Clark et al. [52] on airfoils with finlets at high Re numbers, which suggest there is room for the optimization process of the finlet geometry adapting it to the complex three-dimensional flow with low Reynolds number. Additionally, a detailed analysis of the fan efficiency be conducted.

The flexible trailing edge showed a decrease in wake thickness suggesting a reduction in trailing edge noise. Unfortunately the mesh used does not reach the requirements of the acoustic model. Since it is a novel idea, there are several possibilities to explore. Concrete suggestions consist in modifying the flexible material and the shape of the

flexible trailing edge making it with a serration shape, since the literature refers to the use of serrations as a method of reducing wake thickness showing that it has the same effect as the flexible trailing edge which can lead to a combined reduction. The complexity of simulation is the main challenge for this study, but it can be drastically reduced if the movement of the trailing edge is characterized by wind tunnel test and subsequently inserted as a pre-processing parameter, transforming the simulation from FSI into a transient state CFD simulation.

Overall, considering this work a detailed study of the broadband boundary layer noise resulting in a small increment to the overall fan noise reduction. In the same way as this study different in depth studies should be conducted in the major contributors to heat pump noise (fan, compressor, pipes, fins) being subsequently evaluated within the heat pump unit. This way the noise reduction of the heat pump unit should be predicated by small increments resulting in a continuous work towards a "silent" heat pump.

Intentionally blank page.

References

[1] Gunda Mader. *Economic analysis of air-water heat pump technologies with a screening method*. PhD thesis, Sweden Royal Institute of Technology, 2015.

[2] Bosch Thermotechnik GmbH. Wärmepumpen von bosch. Brochure Available: `https://www.bosch-thermotechnology.com/ocsmedia/optimized/full/o399483v272_PR18750_--_Bosch_TT_--_Broschu_re_--_Wa_rmepumpen_--_8737710041_--_10-18___RZ3lowres.pdf`, 2018. Accessed: 2019-02-21.

[3] Timothy Newman. *Towards a silent fan: an investigation of low-speed fan aeroacoustics*. PhD thesis, Cambridge University, 2014.

[4] Florian Krömer. *Sound emission of low-pressure axial fans under distorted inflow conditions*. PhD thesis, FAU University Press, 2018.

[5] Doolan Moreau, Brooks. The effect of boundary layer type on trailing edge noise from sharp-edged flat plates at low-to-moderate reynolds number. *Journal of Sound and Vibration*, 331:3976 – 3988, 2012.

[6] Mats Allam, Abom. Noise reduction for automotive radiator cooling fans. *Fan 2015: International Conference on Fan noise, Technology and Numerical Methods*, 2015.

[7] Ageborg Morsing. Wind turbine noise and sleep: Pilot studies on the influence of noise characteristics. *International Journal of Environmental Research and Public Health*, 15:2573, 2018.

[8] Helmut Klug. Noise from wind turbines standards and noise reduction procedures. In *Forum Acusticum Sevilla: 3rd European Congress on Acoustics*, page 88, 2002.

[9] Andrew Lohn. What's the buzz? the city-scale impacts of drone delivery. *Rand Corporation Report*, 2017.

[10] Randolph Cabell. Initial investigation into the psychoacoustic properties of small unmanned aerial system noise. In *17th AIAA Aviation Technology, Integration, and Operations Conference*, 2017.

[11] Rong-Ping Huang, Shih-Pin. Frequency characteristics of interior noise in houses. In *World Sustainable Building Conference*, 2005.

[12] Santos Carmen. Aeroacoustic noise analysis of axial fans using computational fluid dynamics (CFD) and computational aeroacoustics (CAA). Master's thesis, Universidade de Aveiro, 2018.

[13] Dennis L Huff. Noise reduction technologies for turbofan engines. *NASA Glenn Research Center*, 2007.

[14] NASA Glenn Research Center. NASA facts: Making future commercial aircraft quieter. Newsletter: `https://www.nasa.gov/centers/glenn/about/fs03grc.html`. Accessed: 2017-06-12.

[15] Michael Jones, T Parrott, Daniel Sutliff, and C Hughes. Assessment of Soft Vane and Metal Foam Engine Noise Reduction Concepts. *15th AIAA/CEAS Aeroacoustics Conference*, 2012.

[16] Dale E. Van Zante, Douglas M. Nark, and H Claudio Fernandez. Propulsion noise reduction research in the nasa advanced air transport technology project. *NASA Langley Research Center, NASA Glenn Research Center*, 2017.

[17] Jones Nark. Further development and assessment of a broadband liner optimization process. *22nd AIAA/CEAS Aeroacoustics Conference*, 2016.

[18] Doolan Hansen, Kelso. Reduction of flow induced tonal noise through leading edge tubercle modifications. *16th AIAA/CEAS Aeroacoustics Conference*, 2010.

[19] S.Oerlemans. Technical report in wind turbine noise: primary noise sources. `https://reports.nlr.nl/xmlui/bitstream/handle/10921/117/TP-2011-066.pdf?sequence=1&isAllowed=y`. Accessed: 2019-05-05.

[20] Carpio Rubio, Avallone Merino-Martinez, and Snellen Ragni. Broadband trailing edge noise reduction using permeable metal foams. In *Conference Inter-Noise 2017*, 2017.

[21] Mößner Lippitz Rossignol, Delfs. Specifcation of porous materials for low-noise trailing-edge applications. *20th AIAA/CEAS Aeroacoustics Conference*, 2014.

[22] Dubravko Miljković. Methods for attenuation of unmanned aerial vehicle noise. *MIPRO Conference 2018*, 2018.

[23] S. Dixon and C. Hall. *Fluid Mechanics and Thermodynamics of Turbomachinery*. Pergamon Press, 4th edition, 2010.

[24] Franz Durst. *Fluid Mechanics: An Introduction to the Theory of Fluid Flows*. Springer, Chap: 2-5, 2008.

[25] Hannes Sturm, Gerrit Dumstorff, Peter Busche, Dieter Westermann, and Walter Lang. Boundary layer separation and reattachment detection on airfoils by thermal flow sensors. *Journal Sensors ISSN 1424-8220*, 12:14292–306, 2012.

[26] Gherardo Zambonini. *Unsteady dynamics of corner separation in a linear compressor cascade*. PhD thesis, Central School of Lyon, 2016.

[27] Haller Surana, Grunberg. Exact theory of three-dimensional flow separation. part 1. steady separation. *Journal of Fluid Mechanics*, 564:57 – 103, 2006.

[28] Jean Délery. *Three-dimensional Separated Flow Topology*. FOCUS Fluid Dynamic Series, 2013.

[29] Ankit Sachdeva. *Study and control of three dimensional flow separation in a high pressure compressor stator blade row by boundary layer aspiration.* PhD thesis, Central School of Lyon, 2010.

[30] Marcolini Brooks, Pope. Airfoil self-noise and prediction. *NASA Langley Research Center*, 1218:145, 1989.

[31] Michael Collison, Ludovic Desvard, and Ryan Stimpson. Vortex shedding noise reduction of a mixed flow fan: Experimental and numerical investigation. 2015.

[32] Mohd Noor and Nazihah. Analysis of vortex shedding in a various body shapes. Master's thesis, Universiti Tun Hussein Onn Malaysia, 2015.

[33] Ayad Beskales, Abdellatif Samir, and Samer Anwar. The effect of tip end-blade geometry on the axial fans performance. In *Eleventh International Conference of Fluid Dynamics*, 2013.

[34] Dominic Lallier-Daniels. *Analysis of Tip Leakage Flow Noise Inception in Axial Fans.* PhD thesis, University of Sherbrooke, 2019.

[35] Cengi Camci. Tip clearance investigation of a ducted fan used in vtol uavs. *Journal of Turbomachinery*, 136:215, 2014.

[36] Neise Kameier. Experimental study of tip clearance losses and noise in axial turbomachines. *VDI-Tagung Turbomachinery - Fluid Dynamic and Thermodynamic Aspects*, 119:229–243, 1995.

[37] Weijie Zhang and Banglun Jianping. The influence of axial-flow fan trailing edge structure on internal flow. *Advances in Mechanical Engineering*, 10:168, 2018.

[38] Atsushi Nashimoto, Tsuneo Akuto, Yuichi Nagase, and Nobuyuki Fujisawa. Aerodynamic noise reduction by use of a cooling fan with winglets. *International Journal of Refrigeration*, 2003.

[39] Jin Choi, Woo-Pyung Jeon, and Haecheon Choi. Mechanism of drag reduction by dimples on a sphere. *Physics of Fluids*, 18, 2006.

[40] E. Livya, G. Anitha, and P. Valli. Aerodynamic Analysis of Dimple Effect on Aircraft Wing. *International Journal of Aerospace and Mechanical Engineering Vol:9*, 2015.

[41] P. W. Bearman and John Kenneth Harvey. Control of circular cylinder flow by the use of dimples. *Experimental Thermal and Fluid Science*, pages 19–26, 1993.

[42] Kurt P. Rouser. *Use of Dimples to Suppress Boundary Layer Separation on a Low Pressure Turbine Blade.* PhD thesis, Air Force Institute of Technology, Ohio, 2002.

[43] Inc ANSYS. ANSYS FLUENT 12.0 Theory Guide. `http://www.afs.enea.it/project/neptunius/docs/fluent/index.htm`. Accessed: 2019-04-22.

[44] Best practice guidelines for turbomachinery CFD – CFD-Wiki, the free CFD reference. `https://www.cfd-online.com/Wiki/Best_practice_guidelines_for_turbomachinery_CFD`. Accessed: 2019-05-12.

[45] Mostafa Nabawy and William Crowther. The role of the leading edge vortex in lift augmentation of steadily revolving wings: A change in perspective. *Journal of The Royal Society Interface*, 14:20170159, 2017.

[46] Helmut Kuehnelt, Alessandro Zanon, Michele De Gennaro, and Domenico Caridi. Reliable CFD/CAA broadband noise prediction of an unducted low speed axial HVAC fan. Technical report, 2014.

[47] Seyedali Sabzpoushan, Masoud Darbandi, Mohsen Mohammadi, and Gerry Schneider. Numerical investigation on periodic simulation of flow through ducted axial fan. *Mathematical and Computational Approaches in Advancing Modern Science and Engineering*, pages 401–411, 2015.

[48] X Hu, S Wen, Y Gao, G. Xi, Bahram Khalighi, and James Johnson. Experimental study on the effect of the shroud on the performance and flow field of an automotive cooling fan. *Journal of Automobile Engineering*, 225:627–642, 2011.

[49] Ian Clark, W. Alexander, William Devenport, Stewart Glegg, Justin Jaworski, Conor Daly, and Nigel Peake. Bioinspired trailing-edge noise control. *AIAA Journal*, 55:1–15, 2016.

[50] Edward Talboys, Thomas Geyer, and Christoph Brücker. The aerodynamic and aeroacoustic effect of passive high frequency oscillating trailing edge flaplets. *IUTAM Symposium on Critical flow dynamics involving moving/deformable structures with design applications*, 2018.

[51] Justin Jaworski and Nigel Peake. Aerodynamic noise from a poroelastic edge with implications for the silent flight of owls. *Journal of Fluid Mechanics*, 723:456–479, 2013.

[52] Ian Clark, WN Alexander, William Devenport, S Glegg, Justin Jaworski, C Daly, and Nigel Peake. Bio-inspired trailing edge noise control. *Journal of Sound and Vibration*, 2017.

[53] Auris Juknevičius and Tze Chong. On the leading edge noise and aerodynamics of thin aerofoil subjected to the straight and curved serrations. *Journal of Sound and Vibration*, 425:324–343, 2018.

[54] Matthias Weger and Hermann Wagner. Morphological variations of leading-edge serrations in owls. *Plos one*, 11:149, 2016.

[55] Gurvan Jodin, Scheller Motta, Döll Duhayon, and Braza Rouchon. Dynamics of a hybrid morphing wing with active open loop vibrating trailing edge by time-resolved PIV and force measures. *Journal of Fluids and Structures*, 2017.

[56] Stéphane Moreau, Michel Roger, and Julien Christophe. Flow features and self-noise of airfoils near stall or in stall. *15th AIAA/CEAS Aeroacoustics Conference*, 2009.

[57] EBM Papst. Ec axial fan. `https://www.ebmpapst.com/en/products/axial-fans/axial_fans.php`, 2015. Accessed: 2019-08-29.

Appendices

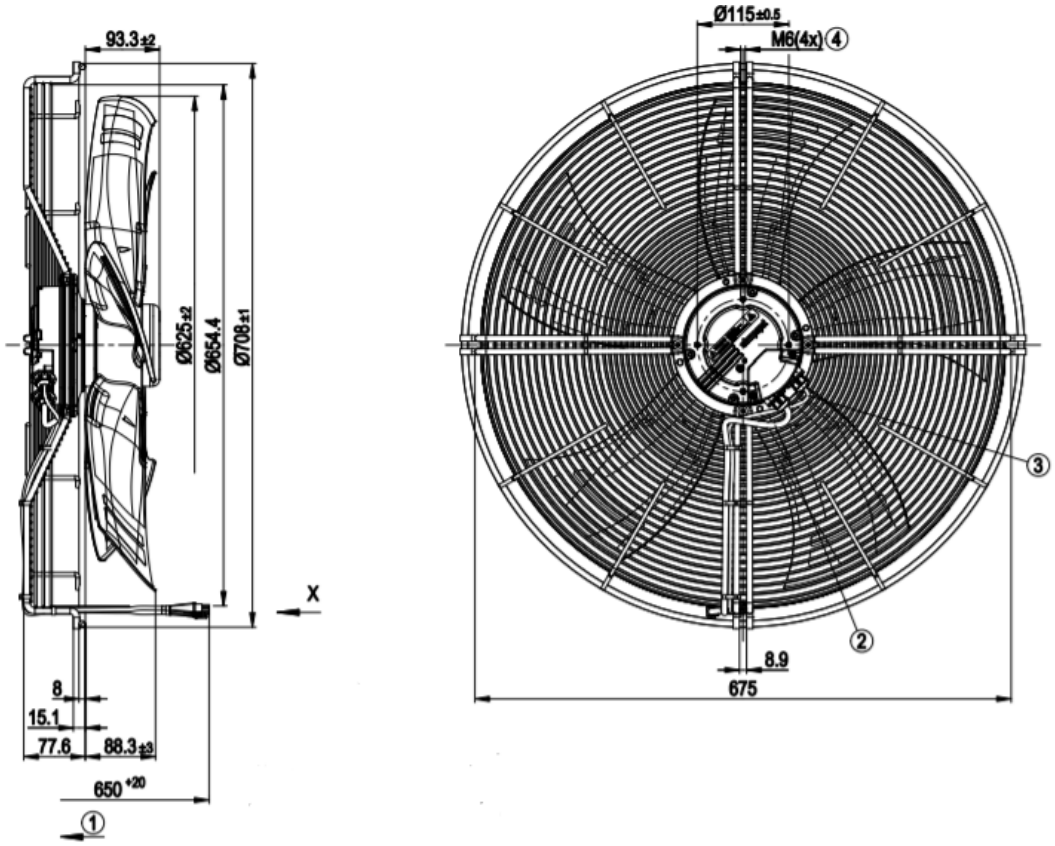

Figure 1: Fan drawing [57]

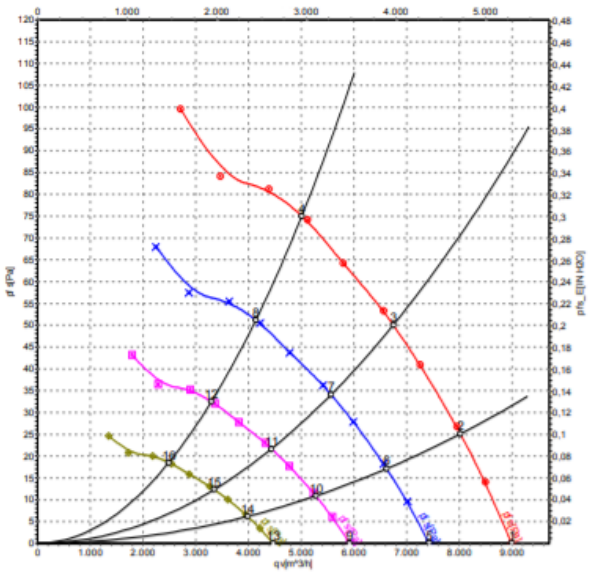

Measured values

	U	f	n	P_{ed}	I	LpA_{in}	LwA_{in}	LwA_{out}	qv	p_{fs}
	V	Hz	min^{-1}	W	A	dB(A)	dB(A)	dB(A)	m^3/h	Pa
1	230	50	800	170	0.76	56	63	62	8985	0
2	230	50	800	211	0.93	57	63	62	8015	25
3	230	50	800	245	1.08	57	63	62	6745	50
4	230	50	800	280	1.20	60	67	67	5010	75
5	230	50	665	96	0.43	52	59	58	7420	0
6	230	50	665	119	0.53	53	59	58	6620	17
7	230	50	665	138	0.61	53	59	58	5565	34
8	230	50	665	155	0.68	56	63	63	4135	51
9	230	50	530	49	0.22	47	54	53	5915	0
10	230	50	530	60	0.27	48	54	53	5275	11
11	230	50	530	70	0.31	48	54	53	4435	22
12	230	50	530	79	0.35	51	58	58	3295	33
13	230	50	400	21	0.09	41	48	47	4465	0
14	230	50	400	26	0.11	42	47	47	3980	6
15	230	50	400	30	0.13	42	48	47	3350	12
16	230	50	400	34	0.15	45	52	52	2485	19

U = Supply voltage · f = Frequency · n = Speed · P_{ed} = Power input · I = Current draw · LpA_{in} = Sound pressure level inlet side · LwA_{in} = Sound power level inlet side · LwA_{out} = Sound power level outlet side
qv = Air flow · p_{fs} = Pressure increase

Figure 2: Impeller operating curves at 50Hz [57].

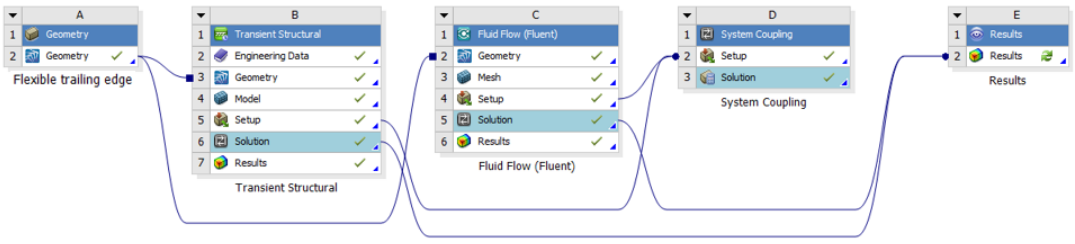

Figure 3: FSI Simulation workflow for the Chapter 5.3.